ADDITIVE MANUFACTURING OF 3-DIMENSIONAL BIOCERAMIC STRUCTURES ELABORATED BY CALCIUM PHOSPHATE CEMENT REACTIONS

A THESIS SUBMITTED TO
THE GRADUATE SCHOOL OF NATURAL AND APPLIED SCIENCES
OF
MIDDLE EAST TECHNICAL UNIVERSITY

BY

HÜSEYIN ENGIN SEVER

IN PARTIAL FULFILLMENT OF THE REQUIREMENTS
FOR
THE DEGREE OF MASTER OF SCIENCE
IN
METALLURGICAL AND MATERIALS ENGINEERING

JULY 2022

Approval of the thesis:

ADDITIVE MANUFACTURING OF 3-DIMENSIONAL BIOCERAMIC STRUCTURES ELABORATED BY CALCIUM PHOSPHATE CEMENT REACTIONS

submitted by **HÜSEYIN ENGIN SEVER** in partial fulfillment of the requirements for the degree of **Master of Science in Metallurgical and Materials Engineering Department, Middle East Technical University** by,

Prof. Dr. Halil KALIPÇILAR
Dean, Graduate School of **Natural and Applied Sciences** _____

Prof. Dr. Ali Kalkanlı
Head of Department, **Metallurgical and Materials Engineering** _____

Prof. Dr. Caner Durucan
Supervisor, **Metallurgical and Materials Engineering, METU** _____

Examining Committee Members:

Prof. Dr. Arcan F. Dericioğlu
Metallurgical and Materials Engineering, METU _____

Prof. Dr. Caner Durucan
Metallurgical and Materials Engineering, METU _____

Prof. Dr. Ziya Esen
Inter-Curricular Courses Department, Çankaya University _____

Assist. Prof. Dr. Simge Çınar Aygün
Metallurgical and Materials Engineering, METU _____

Assist. Prof. Dr. Irmak Sargın
Metallurgical and Materials Engineering, METU _____

Date: 26.07.2022

I hereby declare that all information in this document has been obtained and presented in accordance with academic rules and ethical conduct. I also declare that, as required by these rules and conduct, I have fully cited and referenced all material and results that are not original to this work.

Name, Surname: Hüseyin Engin Sever

Signature :

ABSTRACT

ADDITIVE MANUFACTURING OF 3-DIMENSIONAL BIOCERAMIC STRUCTURES ELABORATED BY CALCIUM PHOSPHATE CEMENT REACTIONS

Sever, Hüseyin Engin
M.S., Department of Metallurgical and Materials Engineering
Supervisor: Prof. Dr. Caner Durucan

July 2022, 109 pages

Calcium phosphate cements (CPCs) are clinically used in bone related surgical operations for irregular defect filling operations. The cement nature also enables them to be used in additive manufacturing to produce bioceramic structures with irregular shapes and scaffolds with specific geometry, shape and macroporosity, as explored in this thesis. In this study, first a CPC cement precursor, α-tricalcium phosphate (α-TCP or α-$Ca_3(PO_4)_2$), is synthesized by using two different powder mixtures of $CaHPO_4$:$CaCO_3$ and $Ca_2P_2O_7$:$CaCO_3$, respectively. The end-product of second mixture found to be more reactive for cement conversion. The cement conversion here implies conversion of a-TCP to biological bone mineral-like phase calcium deficient hydroxyapatite (CDHAp or $Ca_9(PO_4)(HPO_4)(OH)$) upon water uptake. The synthesized α-TCP powder are combined with two different binder liquid solutions (Pluronic F127:water and sodium Alginate:water) to obtain injectable cement paste. It is observed that α-TCP:Pluronic F127:Water mixture showed better injectability and provided good integrity upon injecting. α-TCP-based and/or hybrid cement pastes were prepared by blending α-TCP:calcium sulfate Hemihydrate (Plaster of Paris, CSH or $CaSO_4 \cdot \frac{1}{2} H_2O$) and hydration (cement conversion) behavior of those mixtures were

examined thoroughly. It is shown that CSH addition delayed hydration of α-TCP. Taking into consideration of preliminary experiments, optimized cement pastes were implemented on Direct-Ink Writing 3D printing process. Scaffolds with different solid compositions (TCP:CSH) were successfully fabricated. As it was expected, addition of CSH did not improve the strength of the scaffolds, however it enabled controlling microporosity for the printed constructs due to dissolution of calcium sulfate phases during cement hydration. The results of this can be expanded to print any irregular shaped CDHAp, by combining CAD-supported 3D.

Keywords: Calcium Phosphate Cement, 3D Printing, Bioceramic Scaffold, Setting Reaction, Injectability of Cements

ÖZ

KALSİYUM FOSFAT ÇİMENTO REAKSİYONLARI YARDIMIYLA ÜÇ BOYUTLU BİYOSERAMİK YAPILARIN KATMANLI İMALATLA ÜRETİMİ

Sever, Hüseyin Engin
Yüksek Lisans, Metalurji ve Malzeme Mühendisliği Bölümü
Tez Yöneticisi: Prof. Dr. Caner Durucan

Temmuz 2022 , 109 sayfa

Kalsiyum fosfat çimentosu klinik olarak kemik hastalıkları ve yaralanmaları ile alakalı çarpık kemik boşluklarını doldurmada sıklıkla kullanılır. Çimentomsu yapısı sayesinde katmanlı imalat teknikleriyle birleştirip geometrik olarak düzensiz ve makro gözenekli biyomeseramik doku iskelelerinin üretimi mümkündür. Bu bilimsel çalışmada, çimento ham maddesi olarak kullanılacak olan alfa-trikalsiyum fosfat (α-TCP ya da α-$Ca_3(PO_4)_2$) farklı toz karışımları kullanılarak (sırasıyla $CaHPO_4$:$CaCO_3$ ve $Ca_2P_2O_7$:$CaCO_3$) sentezlenmiştir. İkinci toz karışımı ile üretilen α-TCP tozunun çimento reaksiyonunda daha aktif rol aldığı görülmüştür. α-TCP su ile karıştırdığında sertleşerek biyolojik olarak vücutta bulunan kemik minerali kalsiyumca eksik hidroksiapatite (CDHAp) dönüşür. Sentezelenen α-TCP tozları farklı polimerik tutucularla(Pluronic F127:Su ve sodyum aljinat:Su) hazırlanmış sıvı solüsyonlarla karıştılarak enjekte edilebilir macunumsu bir yapı kazanmıştır. Yapılan deneyler sonucu α-TCP:Pluronic F127:Su karışımlarının enjekte edilebilirliği ve enjekte edildekten sonra yapısını koruma özelliği daha iyi bulunmuştur. α-TCP ve/veya hibrit çimento-

lar kalsiyum sülfat (alçı veya $CaSO_4 \cdot \frac{1}{2} H_2O$) ile karıştılarak hazırlanmış ve sertleşme davranışları incelenmiştir. Kalsiyum sülfat tozunun eklenmesi α-TCP tozunun sertleşmesini geciktirdiği görülmüştür. Öncül deneyleri baz alarak optimize edilmiş çimento karışımları Direct-Ink Writing adı verilen 3 boyutlu basım tekniğine başarıyla aktarılmıştır. Kalsiyum sülfat tozunun eklenmesi beklendiği gibi sertleşme sonrasında mekanik özellikleri arttırmamış ve kalsiyum sülfat fazlarının yapı içerisinde çözünerek makro ve mikro gözenekli bir yapı elde edilmiştir. Bu tezin sonucunda düzensiz makro/mikro gözenekli yapı iskelerinin 3 Boyutlu bilgisayar destekli tasarım yazılımları yardımıyla basılabildiği görülmüştür.

Anahtar Kelimeler: Kalsiyum Fosfat Çimentosu,3 Boyutlu Basım, Biyoseramik Doku İskelesi, Sertleşme Reaksyionu, Enjekte edilebilir Çimento Dolgusu

To my family...

ACKNOWLEDGMENTS

I am deeply thankful to my advisor, Prof. Dr. Caner Durucan, for his supervision, unique support, infinite patience and encouragement throughout the my study and academic life.

I would like to thank to Yusuf Yıldırım helping me in quenching operations, to Orçun Dinçer for particle size analyzes and to BIOMATEN research specialists Dr. Senem Büyüksunur for their help in 3D Printing process, Dr. Engin Pazarçeviren for mechanical tests and Dilara Göksü Tamay for Micro Computed Tomography analyses.

I owe my most sincere gratitude to my colleagues Oğuz Gözcü, Doğuhan Sarıtürk, Can Okuyucu, Esra Kaderli and my labmate Nilsu Öndin for their precious support, and friendship during this journey.

I also would like to express my heartily gratitude to my friends Aral Aksoy, Göksel Yuncu, Rıfat Can Yörük, Sabri Kaan Kayaş and Deniz Tuğrul for their valuable friendship and support. They were always there whenever i needed it.

Finally, my mom, dad and sister... It is impossible to express my feelings by any known words about their support, friendship and guidance throughout my life. Their unconditional love helped me a lot to become the person who i am and the person who i will be.

TABLE OF CONTENTS

ABSTRACT v

ÖZ vii

ACKNOWLEDGMENTS x

TABLE OF CONTENTS xi

LIST OF TABLES xv

LIST OF FIGURES xvi

LIST OF ABBREVIATIONS xx

CHAPTERS

1 INTRODUCTION 1

1.1 Bone Structure and Chemical Characteristics 1

1.2 Bone Grafts 5

1.2.1 Calcium Phosphates 5

1.2.2 Calcium Sulfates 7

1.2.2.1 Hydroxyapatite 9

1.2.2.2 β-tricalcium phosphate 10

1.2.2.3 α-tricalcium phosphate 11

1.2.2.4 Dicalcium Phosphate 13

1.2.2.5 Tetracalcium Phosphate 13

1.2.2.6 Amorphous Calcium Phosphate 13

1.2.3 Calcium Phosphate and Calcium Sulfate Cements 14

1.2.3.1 Brushite Cements 15

1.2.3.2 Apatite Cements 15

1.3 Injectability/Shaping Ability of Calcium Phosphate Cements 19

1.3.1 Effect of Packing Fraction of Powder and Liquid to Powder Ratio 20

1.3.2 Effect of Particle-Particle Interaction 21

1.3.3 Effect of Setting (Cement) Reaction 22

1.3.4 Effect of Extrusion Parameters 22

1.3.5 Effect of Viscosity 23

1.4 3D Printing of Bioceramics 25

1.4.1 Selective Laser Sintering 26

1.4.2 Stereolithography 26

1.4.3 Fused Deposition Modeling 27

1.4.4 Inkjet Writing 28

1.4.5 Direct-Ink Writing 28

1.5 Objective and Rationale of the Thesis 31

2 MATERIALS AND METHODS 35

2.1 Materials 35

2.2 Methods 36

2.2.1 Synthesis of α-TCP Powder 36

2.2.2 Cement Paste Preparation 39

2.2.3 3D Printing of α-TCP Scaffolds 40

2.2.4 Post-Printing Treatments of 3D Printed Scaffolds and Dummy Scaffolds 41

2.3 Material Characterization of Solid-State Synthesis, Cement End and Scaffold Products 42

2.3.1 Characterization of Solid-State Synthesis Products and Cement Products 42

2.3.1.1 Particle Size Analysis 42

2.3.1.2 Phase Identification: X-Ray Diffraction Analysis 43

2.3.1.3 Microstructural Investigation: Scanning Electron Microscopy 43

2.3.1.4 Chemical Analysis: Fourier Transformed Infrared Spectroscopy 43

2.3.2 Characterization of 3D Printed Scaffolds 44

2.3.2.1 Mechanical Test: Compressive Strength Test 44

2.3.2.2 Archimedes Porosity Measurement 44

2.3.2.3 Micro Computed Topography 44

3 SYNTHESIS AND CHARACTERIZATION OF CEMENT COMPONENT OF THE PRINTING PASTES/INKS 45

3.1 Characterization of Intermediate Products 45

3.2 Characterization of Solid-State Products 48

4 INJECTABILITY/MANUAL PRINTING STUDIES WITH DIFFERENT CEMENT PASTE FORMULATIONS 53

4.1 Effect of Binder Solution and LPR on Injectability of Calcium Phosphate Cement Paste 54

4.2 Characterization of Dummy Scaffolds 58

5 DIRECT-INK WRITING STUDIES WITH CEMENTS INKS 75

5.1 Optimization Automated Printing Parameters 76

5.2 Microstructural Characterization of 3D Printed Scaffolds: Porosity . . 81

5.2.1 Micro-CT and SEM Images of the Scaffolds 82

5.2.2 Archimedes Porosity Measurement and Compression Test of the Printed Scaffolds 91

6 CONCLUSIONS 95

REFERENCES 99

LIST OF TABLES

TABLES

Table 1.1 List of Calcium Phosphates depending on Ca/P ratio and stability . . 6

Table 2.1 Printing paste formulations varying liquid to powder ratio and binder concentration 39

Table 2.2 The composition of printing pastes 41

Table 2.3 PBS solution is prepared at 25 °C in 1 litre of DI water with the compounds and amounts 42

Table 4.1 % Injectability values of different printing paste formulations determined according to Equation (2.3) 54

Table 4.2 Chemical composition (by EDS) CSH10 scaffolds 62

Table 4.3 Chemical composition (by EDS) CSH25 scaffolds 63

Table 4.4 Summary of XRD results of TCP,CSH10 and CSH25 samples . . . 64

LIST OF FIGURES

FIGURES

Figure 1.1 Bone Structure from nano level to macro level 2

Figure 1.2 Ashby Plot of naturally found materials 3

Figure 1.3 Isotherm Diagrams of Calcium Phoshpates depends on molarity and pH 8

Figure 1.4 Phase diagram of $CaO\text{-}P_2O_5$ 10

Figure 1.5 Phase diagram of $CaO\text{-}P_2O_5$ system in the presence of water vapor 12

Figure 1.6 Represantive view of Direct-Ink Writing process 29

Figure 2.1 Flow Chart of Solid State Synthesis of α-TCP 38

Figure 3.1 XRD-diffractograms of intermediate Products 46

Figure 3.2 FTIR spectrum of Monetite and Calcium Pyrophostate 47

Figure 3.3 The XRD diffractograms of the solid state synthesis of TCPs . . 48

Figure 3.4 The SEM images of end-products of the solid state reactions . . 50

Figure 3.5 The particle size distribution of TCP powder 51

Figure 4.1 Digital camera images of dummy scaffolds, printed using cement paste prepared with 2 wt.% alginate:DI water liquid solution . . . 55

Figure 4.2 Digital camera image of a dummy scaffold prepared with 20 wt.% Pluronic F127:DI water liquid solution 57

Figure 4.3 The XRD diffractograms of TCP:Pluronic F127(20 wt.%) scaffolds in as-printed condition and after hydration for 6, 12, 24, 48 ,and 72 h in excess DI water. 58

Figure 4.4 The XRD diffractograms of CSH10:Pluronic F127(20 wt.%) scaffolds in as-printed condition and after hydration for 6, 12, 24, 48 ,and 72 h in excess DI water. 61

Figure 4.5 The XRD diffractograms of CSH25:Pluronic F127(20 wt.%) scaffolds in as-printed condition and after hydration for 6, 12, 24, 48 ,and 72 h in excess DI water. 63

Figure 4.6 FTIR spectra of pure TCP, CDHAp, CSH and CSD 65

Figure 4.7 FTIR spectra of TCP, CSH10 and CSH25 scaffolds, designating binder (Pluronic F127) time 67

Figure 4.8 FTIR spectra of CSH10 and CSH25 scaffolds 69

Figure 4.9 SEM micrographs of TCP, CDHAp, CSH and CSD 70

Figure 4.10 Microstructural changes of TCP-based scaffolds during hydration as a function of hydration time 71

Figure 4.11 Microstructural changes of CSH10 scaffolds during hydration as a function of hydration time 72

Figure 4.12 Microstructural changes of CSH25 scaffolds during hydration as a function of hydration time 74

Figure 5.1 Initial printing trial of previously optimized cement-ink with the following parameters: LPR:0.6 ml/g, Concentration of binder: 20 wt.% Pluronic F127. 76

Figure 5.2 Effect of lowering LPR from 0.6 to 0.55 ml/g on the viscosity of the cement-ink, binder concentration:20 wt.% Pluronic F127. 77

Figure 5.3 Effect of increasing binder concentration in DI water from 20 to 25 wt.% Pluronic F127 on the viscosity of the cement-ink, LPR:0.65 . . 78

Figure 5.4 Effect of printing increased speed (from 3 to 6 mm/s) on the structural integrity of the scaffold; Binder concentration: 25 wt.% Pluronic F127, LPR:0.6 79

Figure 5.5 Effect of reducing tip(opening orifice) diameter on printing and on the scaffold integrity, Binder concentration: 25 wt.% Pluronic F127, LPR:0.6 79

Figure 5.6 Effect of increased printing speed on the printing and on the scaffold integrity, Binder concentration: 25 wt.% Pluronic F127, LPR:0.6 80

Figure 5.7 3D Printed TCP Scaffolds with the optimized parameters: LPR:0.6, Binder Concentration: 25 wt.%, Tip I.D:0.4 mm, Printing Speed:9 mm/s 81

Figure 5.8 Top view of scaffolds after constructing 3D structure via software shows the alignment of the scaffold and surface finish quality before and after the hydration 83

Figure 5.9 Isometric and cross-sectional views of scaffolds after constructing 3D structure via software shows the structural integrity before and after hydration and porosities are observable clearly 85

Figure 5.10 Cross-sectional views of the scaffolds directly taken without processing show the porosities inside the structures and alignment between the strands 86

Figure 5.11 SEM images of TCP,CSH10 and CSH25 at x100 magnification . 87

Figure 5.12 SEM images of TCP,CSH10 and CSH25 at x400 magnification . 88

Figure 5.13 SEM images of TCP,CSH10 and CSH25 at x4000 magnification 90

Figure 5.14 Bulk porosities (in volume %) of TCP, CSH10 and CSH25 scaffolds. 92

Figure 5.15 Uniaxial compressive strength values (in MPa) of TCP, CSH10 and CSH25 scaffolds. 93

LIST OF ABBREVIATIONS

2D	2 Dimensional
3D	3 Dimensional
HAp	Hydroxyapatite
CaP	Calcium Phopshate
CPC	Calcium Phopshate Cement
CSC	Calcium Sulfate Cement
CaS	Calcium Sulfate
CSH	Calcium Sulfate Hemihydrate
CSD	Calcium Sulfate Dihydrate
β-TCP	β-Tricalcium Phosphate
α-TCP	α-Tricalcium Phopshate
CPP	Calcium Pyrophosphate
CDHAp	Calcium Deficient Hydroxyapatite
LPR	Liquid to Powder Ratio
DIW	Direct-Ink Writing
CSH10	10 wt.% CSH:90 wt.% TCP
CSH25	25 wt.% CSH:75 wt.% TCP
asp	as-printed

CHAPTER 1

INTRODUCTION

1.1 Bone Structure and Chemical Characteristics

Bone is the part of the skeletal system which is principally responsible for the load-carrying function of the body. Bone structure is unique concerning its hierarchical configuration and its composite characteristic. Bone composite is in the form of a calcium phosphate matrix reinforcdd by the collagen fibers to make up a lamellar structure that is the simple basic unit of the bony structures [1]

Bone as a material is composed of three main constituents: a fibrous protein part called collagen, a mineralized part called apatite or dahllite (calcium phosphate crystal with carbonated sites) and water. The main inorganic constituents are bound together to form an ordered structure considered a "building block" for the bony structures [2, 3, 4]. Hierarchically, the organization of the bone can be classified as structurally and the size of the structural units of the bone. The hierarchical structure of the bone is illustrated in Figure 1.1 from starting nano size (collagen molecule) to macro scale (spongy bone).

The organic component of the bone is called collagen, which is a structural protein for the skeletal systems as well as for other connective tissues [5]. Type I collagen is the most abundant protein in the bone by creating at least 90 wt.% of the organic portion and 20-25 wt.% of the bone. Type I collagen has a fibrous character and makes up the first tropocollagen triple helix with three collagen molecules in a helical shape with many polypeptide chains between the collagen molecules, then non-collagen proteins in the collagen fibril that allows mineralization of hydroxyapatite ($Ca_{10}(PO_4)_6(OH)_2$ or HAp) nanocrystals $50\,\mathrm{nm} \times 30\,\mathrm{nm} \times 5\,\mathrm{nm}$ in a regular array of $40\,\mathrm{nm}$ gaps with

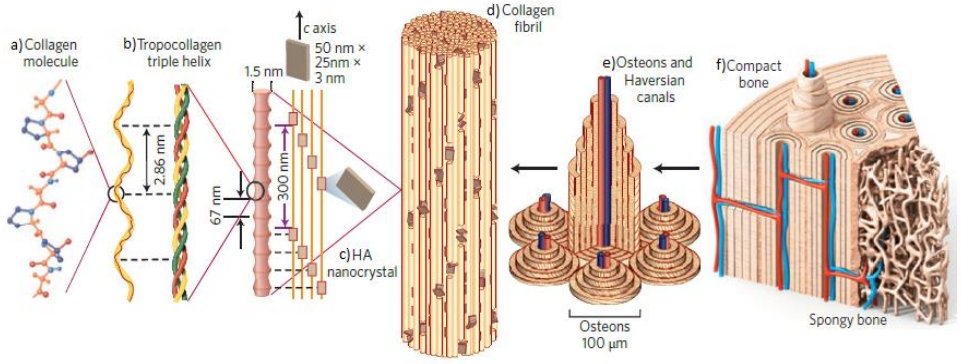


Figure 1.1: Hierarchical Structure of Bone from starting nanosize to bulky structure:(a) single collagen molecule in few nanometer; (b) triple helix of collagen molecules combined to tropocollagen structure; (c) HAp nanocrystal embedded collagen matrix; (d) cluster of tropocollagen along c-axis in few micron size; (e) osteons and haversian canals made up by collagen fibril in hundreds of micron size; (f) compact and spongy bone as a bulk structure.

$67\,\mathrm{nm}$ periodicity [3, 4, 6]. Collagen is responsible for the flexibility of the bone tissue. Collagen fibrils are always associated with other molecules to get higher hierarchical structures, such as osteons and Haversian canals. Moreover, there are different types of collagen fibril arrays in 3-dimensions that changes the mechanical property of the structure [2].Water is the second most abundant inorganic component (1-10 wt%) of the bone. The amount of water varies with the types of bone tissue and changes the mechanical properties (such as elastic modulus) of the bone [3, 7]. Apatite is the most abundant inorganic component of the bone (60-70 wt.%) that is commonly composed of calcium, phosphate and hydroxyl group. The stoichiometric apatite is called hydroxyapatite in the formula of $Ca_{10}(PO_4)_6(OH)_2$. There are several non-stochiometric types of apatite by an ionic substitution of different atoms and molecules such as carbonate (CO_3), fluoride, chloride, magnesium, sodium, potassium, citrate and hydrogen phosphate (HPO_4) in a biological apatite. Bone mineral is calcium-deficient apatite with a Ca/P ratio is less than 1.67, while stoichiometric hydroxyapatite Ca/P ratio is 1.67. The primary role of the apatite mineral is to provide strength, toughness and rigidity to the bone [7, 8, 9].

All types of bones are composed of collagens, apatite and water, but their composition in the bone structure provides different levels of porosity and density to the bone structure. The mechanical property of the bone is highly dependent on the porosity level of the bone structure. Cortical (dense) and cancellous (spongy) bones are classified according to their porosity level; their porosity varies between 5-10% and 50-90%, respectively [3]. As a results of a porosity volume differences, mechanical property of the cancellous bone has much lower strength compared to compact bone as it shown in Figure 1.2 [4]. Additionally, the macroporous structure of the bone enables molecules, nutrients and cells to diffuse or move inside the bone structure and help the physiological process called bone remodeling [10, 11], i.e. resorption and reformation of bone tissue.

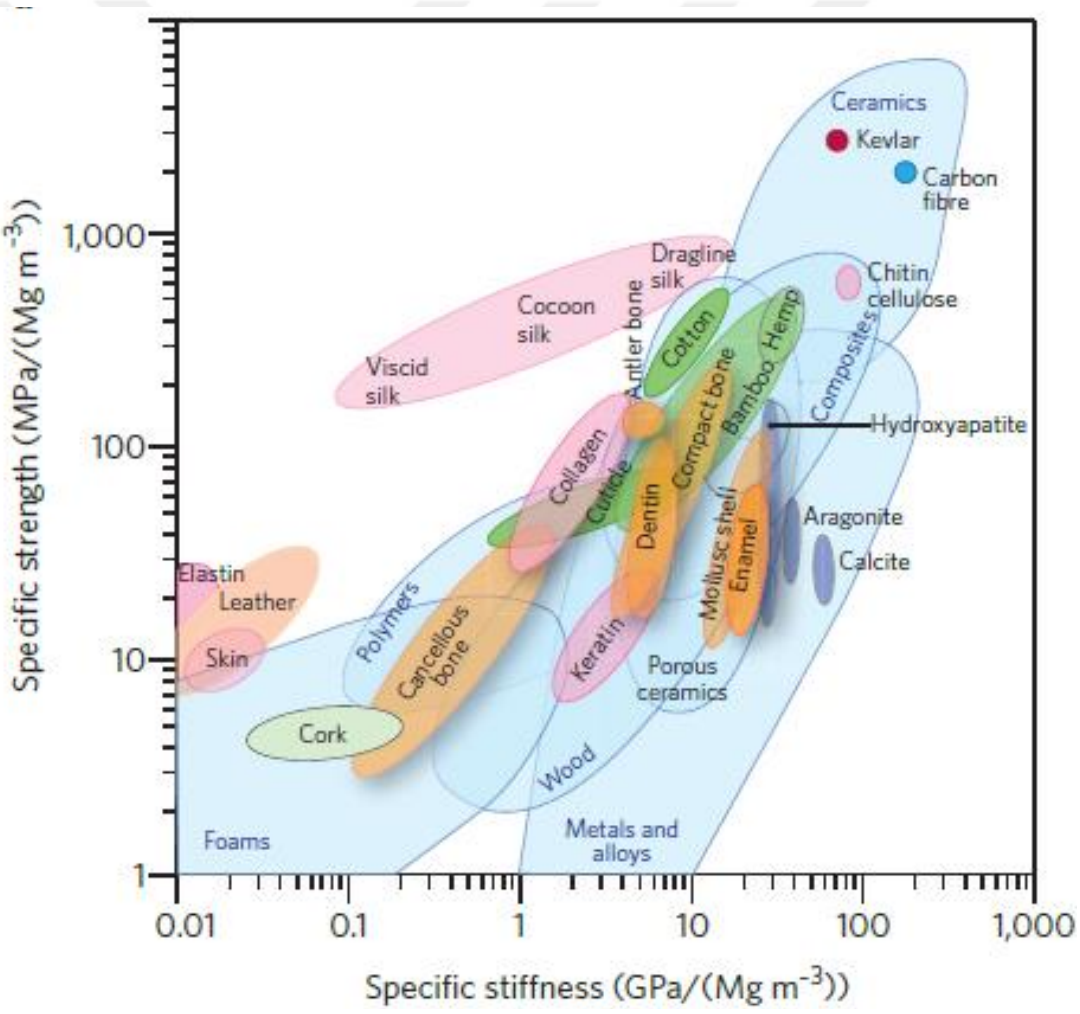


Figure 1.2: Ashby Plot of a wide range material (includes ranges for cancellous bone and compact bone) according to their specific strength and specific modulus [4].

The cells found in bone are namely osteoblasts, osteocytes, bone-lining cells and osteoclasts. Osteoblasts are responsible for production of collagen fibers and mineralizing calcium and phosphate ions into apatite crystals, also called bone formation. They originate from mesenchymal stem cells, while osteoclasts are responsible for the direct dissolution of the bone matrix called bone resorption and they are derived from macrophage cells. Osteocytes and bone lining cells are responsible for stimulating both processes that depend on the requirement. The maintenance of the physiological bone depends on the strict balance between bone formation and bone resorption processes called bone remodeling [12]. Any change in the physiological condition due to hormonal activities can increase or decrease the activity of osteoblasts or osteoclasts cells. Commonly known disease related to increased activity of osteoclasts cell results in osteoporosis which weakens the bone mechanically and eventually, the bone fracture occurs [10, 11, 12, 13]. In such cases, the intervention of the external therapeutic methods is necessary when the biological conditions are not sufficient for bone fracture healing.

1.2 Bone Grafts

Bone grafts are the materials externally delivered to the damaged or missing bone tissue for bone reconstruction. Bone grafts are classified into three categories: Autogenous bone grafts, allografts and synthetic grafts. Autograft applications require bone harvest from the patient. Autografts generally show good incorporations and functionality with the host while they are considered as the gold standard for bone graft applications. However, bone harvesting is a surgical process that may result in morbidity and limited availability for the bone harvest zone, which are critical challenges for autograft applications [11]. Allografts are donor grafts that eliminate the limitations for autograft applications. Nonetheless, allografts have potential risks such as viral diseases, bacterial infection and immune rejection in transplanted patients. Synthetic grafts are inexpensive substitutes for both autografts and allografts, considering the ease of production and availability [14, 15]. In this respect, calcium phosphates (CaPs) are generally used in clinical applications by injecting/filling into the related surgical sites and defects. In addition, CaPs can be used to fabricate scaffolds rather than injectable pastes. Scaffold fabrication principles are mainly related to the injectability of CPCs and processing parameters and functional properties are similar for both cases.

1.2.1 Calcium Phosphates

Calcium phosphates (CaP) are the most widely used type of ceramics for bone substitution applications since the main constituents of bone and teeth are CaPs. Calcium phosphates were tried out in the early 1900s to stimulate bone growth and the first commercial CaPs were begun to use between 1975 and 1980 [16]. CaPs are used as coatings on metallic implants and bone defect filling materials due to their excellent biocompatibility. CaPs' osteointegration properties are well known, sometimes may even lead to osteoconduction in bone tissue. There are several types of CaP sources based on their calcium/phosphate (Ca/P) molar ratio, as shown in Table 1.1. The stability of CaP depends on pH and the temperature in an aqueous environment and the classification of CaP is based on solubility behavior in physiological conditions [17].

Table 1.1: Calcium Phosphates are sorted by Ca/P molar ratio according to the compound formula and their stability in aqueous solutions with varying pH values at 25 °C. (Adapted from [7])

Ca/P Molar Ratio	**Compound**	**Formula**	**Solubility at** $25\,^{\circ}\mathrm{C}$ g/L	**pH stability range in aqueous solutions at 25 °C**
0.5	Monocalcium phosphate monohydrate(MPCM)	Ca(H2PO4)2 . H2O	18	0.0-2.0
0.5	Monocalcium phosphate anhydrous(MPCA)	Ca(H2PO4)2	17	Stable temperatures above 100
1	Dicalcium phosphate dihydrate(DCPD), mineral brushite	CaHPO4 .2H2O	0.088	2.0-6.0
1	Dicalcium phosphate anhydrous(DCPA), mineral brushite	CaHPO4	0.048	Stable temperatures above 100
1.33	Octacalcium phosphate(OCP)	Ca8(HPO4)2(PO4)4 . 5H2O	0.0081	5.5-7.0
1.5	Alpha tricalcium phosphate	a-Ca3(PO4)2	0.0025	can not precipitate
1.5	Beta tricalcium phosphate	b-Ca3(PO4)2	0.0005	can not precipitate
1.2-2.2	Amorphous Calcium Phosphate(ACP)	CaxHy(PO4)z . nH2O, n = 3–4.5; 15–20% H2O	can not be measured	5–12
1.5-1.67	Calcium-deficient hydroxyapatite(CDHA)	Ca10-x(HPO4)x (PO4)6-x(OH)2-x	0.0094	6.5-9.5
1.67	Hydroxyapatite(HAp)	Ca10(PO4)6(OH)2	0.0003	9.5-12
2	Tetracalcium phosphate(TTCP)	Ca4(PO4)2O	0.0007	can not precipitate

By considering their solubility in the aqueous environment, precipitation of the stable product in the presence of excess solute particles becomes possible. Thermodynamic consideration is related to Gibbs free energy of formation of the particle and Gibbs free energy of dissolution of the ions (or ionic activity) in the solvent. The ionic activity also depends on the pH of the aqueous environment since ionic activity changes with pH and temperature. The solubility diagram of mineral compounds is drawn concerning mineral concentration and pH of the solution [18]. Typical solubility isotherms of calcium phosphates are shown in Figure 1.3.

1.2.2 Calcium Sulfates

Calcium sulfate (gypsum or Plaster of Paris) is one of the first implanted materials for bone defect filling operations [19]. Clinically, Peltier practiced it as a bone substitute in 1959 with a highly crystalized and pure state [20]. Generally, gypsum is resorbed in the body within 6-8 weeks, providing effective healing to the damaged bone tissue. Calcium sulfates can be found as anhydrous, hemihydrate (CSH or $CaSO_4 \cdot \frac{1}{2} H_2O$)) and dihydrate (CSD or $CaSO_4 \cdot 2 H_2O$) forms in nature. Mainly, calcium sulfates are employed as cement products since the CSH phase undergoes a hardening reaction when mixed with water at the end; CSD forms after this reaction [21]. However, they come with exothermic hydration reaction problem.

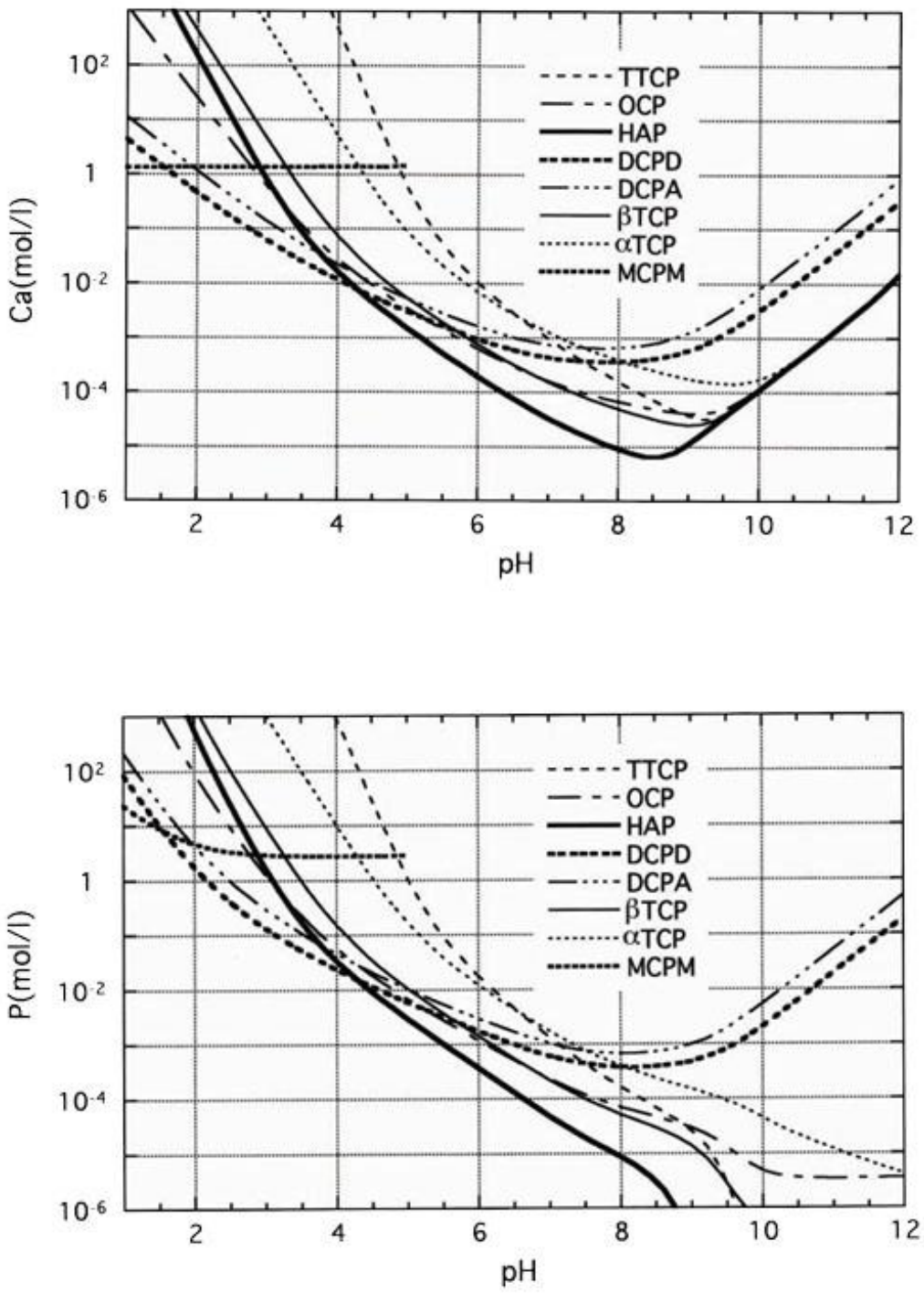


Figure 1.3: Isotherm diagrams of CaPs shows that stability region of CaP compounds with varying pH and molar ratio of calcium and phosphate molecules. The most underlying line in the diagrams shows the most stable CaP product within the given pH value [21]

.

1.2.2.1 Hydroxyapatite

Among the calcium phosphate minerals, HAp ($Ca_{10}(PO_4)_6(OH)_2$) is thermodynamically the most stable product (at around physiological pH) and has many similarities to the natural bone mineral, dahllite. The crystal structure of HAp is monoclinic at room temperature, but it undergoes a phase transition from monoclinic to hexagonal above 250 °C. Due to some impurities such as chloride and fluoride ion substitution, synthetic HAp is always obtained as a hexagonal structure related to stabilizing effect of the substitution ions apatite [7]. Synthetic HAp shows excellent biocompatibility and HAp can stimulate osteoconduction with no toxicity or not triggering inflammation. HAp has many applications, such as a replacement for bony and periodontal defects, tissue engineering systems, drug delivery agents and bioactive coating on metallic implants [18].

HAp syntheses are generally conducted according to three main routes: dry, wet and high-temperature methods. The end products of each process show different chemical, physical and mechanical properties with varying rates of crystallinity and sizes. For example, using the chemical precipitation method with calcium and phosphate salts (wet method) makes it possible to obtain nano size and non-stochiometric HAp with low cost at the expense of crystallinity and end-products of chemical precipitation methods generally require sintering at high temperatures. Using the solid-state method makes it possible to obtain micron size and stoichiometric HAp with very high crystallinity, but the cost is usually higher than other methods [22]. However, solid state-synthesis products may deviate from their stoichiometric ratio of Ca/P=1.67 and have secondary phases different than HAp. Possible secondary phases can be seen in Figure 1.4 [23].

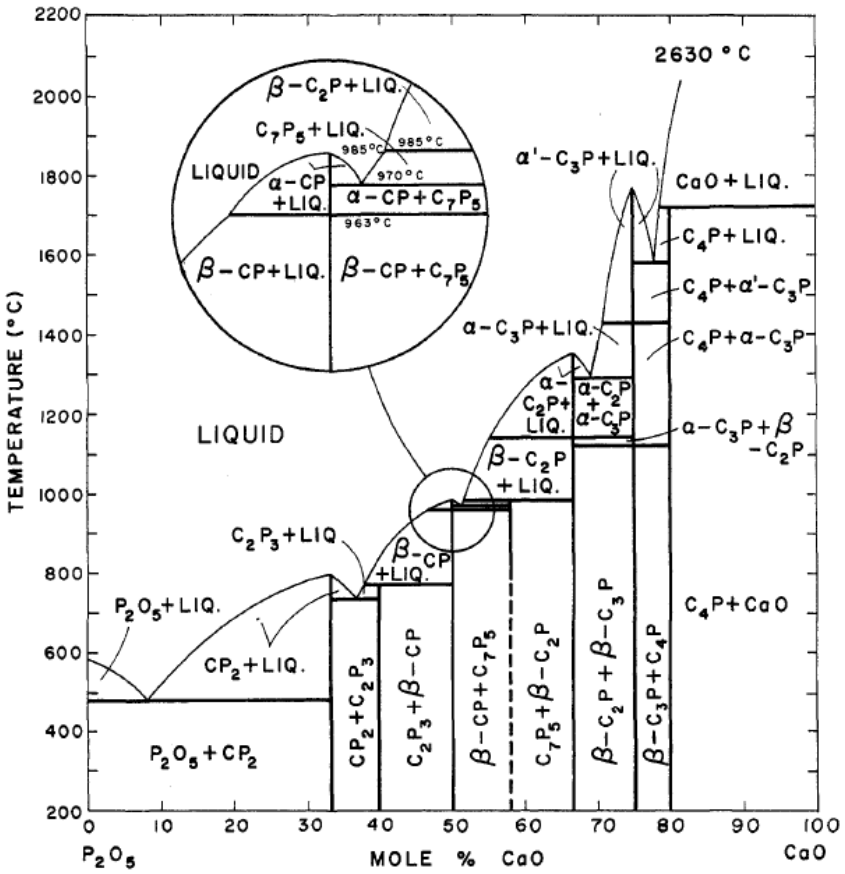


Figure 1.4: Phase diagram of CaO-P_2O_5 system according to Kreidler and Hummel [23].

1.2.2.2 β-tricalcium phosphate

β-tricalcium phosphate (β-TCP or β-$Ca_3(PO_4)_2$) is another calcium phosphate that is not a stable product in aqueous solutions and the stability of β-TCP is only achievable at temperatures above 800 °C. Thermal decomposition of calcium deficient HAp or solid-state chemical reaction is a possible production route for β-TCP [7]. Tricalcium phosphate has three polymorphic phases. The first polymorphic transition of β-TCP to α-TCP occurs at temperatures above 1125 °C and the second polymorphic transition of α-TCP to α'-TCP occurs at temperatures above 1430 °C. It is not possible to obtain α'-TCP below 1430 °C because of instantaneous transformation to α-TCP, while α-TCP polymorph can be obtained by quenching to lower temperatures as the metastable phase [24]. β-TCP is a choice of material due to biocompatibility and

bioresorbable characteristic in the physiological condition of the human body. β-TCP has a generally porous structure which leads to osteoconductivity in bone tissue with its interconnectivity of pores and tissue ingrowth after implantation. However, the mechanical properties of β-TCP are still inferior to the spongy bone and β-TCP is generally used with HA particles called biphasic calcium phosphates (BCP) in bone substitution. A mixture of two phases brings advantages of both powders while losing some properties. BCPs still show bioresorbable properties while the addition of HAp slightly improves their mechanical strength. Thus, a combination of β-TCP and synthetic HAp offers better bioresorbability than using HA alone while showing better mechanical properties than using β-TCP alone [25].

1.2.2.3 α-tricalcium phosphate

α-tricalcium phosphate (α-TCP: α-$Ca_3(PO_4)_2$) is one of the three polymorphs of tricalcium phosphates with a Ca/P ratio of 1.5. As previously stated, α-TCP is not stable at room temperature; however, it is possible to obtain a metastable α-TCP phase with effective quenching after firing above 1200 °C [26]. The crystal structure system of α-TCP is monoclinic, while β-TCP follows rhombohedral symmetry. Due to the structural symmetry differences between α-TCP and β-TCP, the atomic re-arrangement of Ca and phosphate ions in the space require sufficient time. Thus, generally, quenching of TCP in the air is enough to have a metastable α-TCP phase after a solid-state reaction [27]. The structure of α-TCP is more loose compared to β-TCP (the density of β-TCP is higher than α-TCP); consequently, it leads α-TCP phase having higher solubility compared to β-TCP in the aqueous environment [24].

α-TCP synthesis can be accomplished with the thermal transformation of a precursor with Ca/P≈1.5 or a solid-state reaction of precursors. In the first synthesis method, the precursor with Ca/P≈1.5 beforehand is fired above 1400 °C for several hours to complete the transformation of β-TCP to α-TCP. The second route is performed by mixing calcium and phosphate sources by keeping the Ca/P=1.5 and later powder mixture is heated to a temperature at which α-TCP is stable. Like the other solid-state synthesis, precursors are milled together to increase their surface area and reduce their particle size to have a better homogeneous mixture. Generally, the second route

consumes less energy than the first route. However, stoichiometric deviations may lead to formation of second phases other than α-TCP and presence of water vapor in the system may also affect the stability of α-TCP, as shown in Figure 1.5 [24].

For biological applications, α-TCP is generally used as a solid phase for cement products. When α-TCP is mixed with water, it undergoes hardening reactions and becomes calcium deficient hydroxyapatite (CDHAp) rather than stoichiometric HAp. Due to the chemical resemblance of CDHAp to the natural bone mineral, it shows better osteoconductivity than the HAp and leads to better osteointegration for the bone tissue [24, 28].

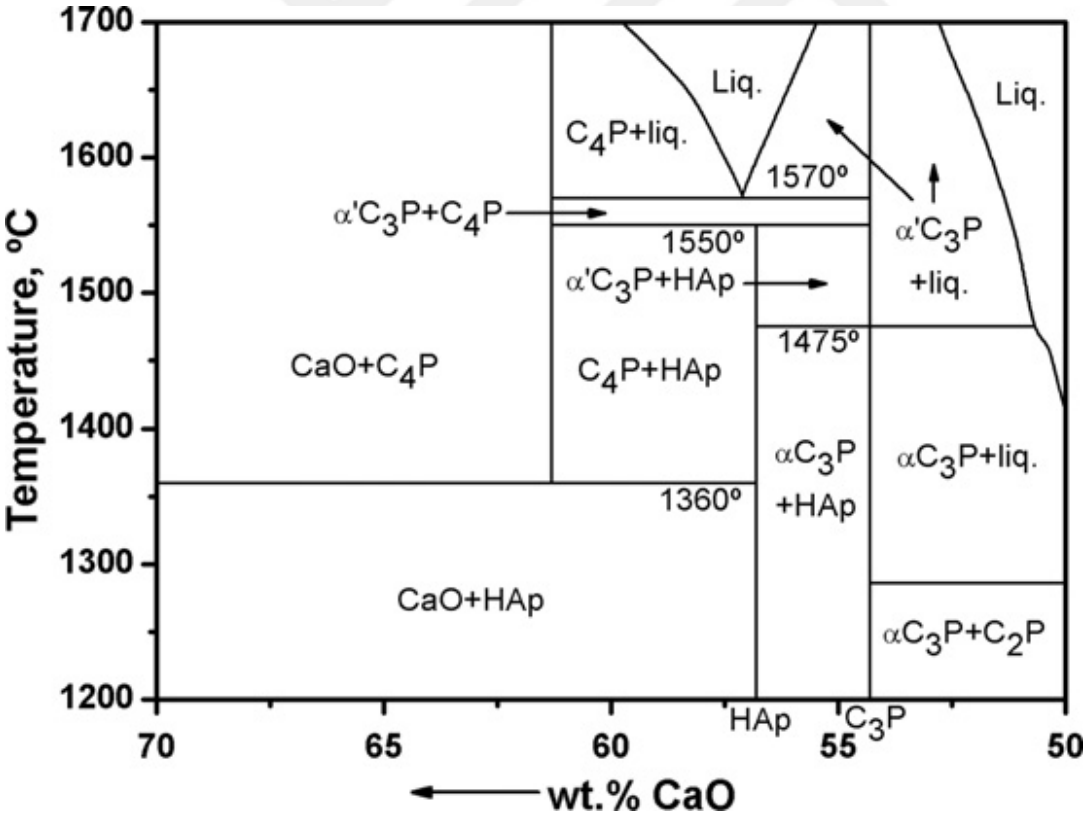


Figure 1.5: Phase diagram of $CaO\text{-}P_2O_5$ system in the presence of $P_{(H_2O)} = 500\text{mm} - Hg$ [24]

1.2.2.4 Dicalcium Phosphate

Dicalcium phosphate is a CaP mineral with a Ca/P ratio of 1.00, as shown in Table 1.1. There are two forms of dicalcium phosphate exist as the anhydrous form (DCPA or $CaHPO_4$), which is called monetite mineral and the hydrate (DCPD or $CaHPO_4 \cdot 2\,H_2O$) form, which is called brushite [7]. Monetite can be synthesized in aqueous environment. by precipitation method at low pH. At the same time, the cement-end products generally form brushite after mixing alkaline Ca source and acidic phosphate source with water [29]. Thermodynamically, brushite transforms to monetite above 80 °C by removing physically bonded water molecules. Further heating of monetite above 400 °C calcium pyrophosphate (CPP) formation removes chemically bonded water molecules from the system.

1.2.2.5 Tetracalcium Phosphate

Tetracalcium phosphate (TTCP or $Ca_4(PO_4)_2O$) is a basic CaP mineral with a Ca/P ratio of 2, as shown in Table 1.1. TTCP generally forms by heating HAp with a higher Ca/P=1.67 above 1300 °C and during cooling, it decomposes to HAp and CaO. TTCP can still be obtained by quenching as a metastable phase at room temperature. Like the other metastable CaP, TTCP can be employed as a potential bone cement as it transforms to CDHAp when mixed with water. The solid-state synthesis route achieves the synthesis of TTCP by combining calcium and phosphate sources in a ratio of 2. Later on, the mixture is fired above 1450 °C for 6-12 h then the powder mixture is quenched in the air to prevent the formation of other CaP phases [30]. TTCP can be used as single-component cement or multi-component cement in various applications.

1.2.2.6 Amorphous Calcium Phosphate

Amorphous calcium phosphate (ACP) is a phase that can be present as a transient phase in the aqueous solutions. ACP is generally precipitated as the first phase from supersaturated solutions by rapid mixing of calcium-containing and phosphate-

containing solutions. The crystallinity of ACP decreases as the concentration of Ca and PO4 increases, additionally in basic pH levels and low crystallization temperatures. Ca/P ratio of ACP varies with these experimental parameters. Also, adding ions of pyrophosphate, carbonate and magnesium to the solution promotes ACP formation in the solution and prevents ACP precipitates from transforming more crystalline CaP minerals. Due to the amorphous characteristics, fast dissolution in the physiological environments. As a bioceramic, ACP is used as the bone cement additive and filling material in dentistry applications [7].

1.2.3 Calcium Phosphate and Calcium Sulfate Cements

Dissolution-precipitation behavior of the inorganic salts in aqueous environment is the main principle of cement-type hydration. Cement reactions occur by dissolution and re-precipitation reactions. One of the well-known cements is calcium sulfate hemihydrates ($CaSO_4 \cdot (1/2)\,H_2O$ or CSH), also called plaster, which undergoes a setting and hardening reaction by turning into calcium sulfate dihydrate ($CaSO_4 \cdot 2\,H_2O$, or CSD) in the presence of water due to favored thermodynamic stability of CSD. This process requires moderate solubility of the reactant and thermodynamic equilibrium of the product precipitated phase. Thus, supersaturation of the most stable phase is needed [18]. In the 1980s, commercial calcium phosphate cements (CPCs) were developed by Brown and Chow and began to be used in biomedical applications, later on replacing calcium sulfate cements [31]. CPCs undergo dissolution and precipitation reactions similar to the calcium sulfate analogs, however only several CaP compounds can exhibit cement-type setting/hardening reaction when mixed with DI water by alone or a mixture. The main CPCs are constituted of DI water as the liquid phase and CaP (single or mixture) as the solid phase(s), there can be additives for CPCs such as organic polymers, common ions and nucleation agents to accelerate decelerate the cement reactions [32]. CaP cement is typically divided into two classes according to their end products and they are called brushite cement and apatite cements.

1.2.3.1 Brushite Cements

Brushite cement was started to be used as bone cement by Mirtchi and Lemaitre in 1989 [33]. Their cement composition consisted of monocalcium phosphate monohydrate (MPM) and β-tricalcium phosphate as the solid phases and water as the liquid phase. Brushite cements are usually being resorbed very quickly in the physiological environment of the human body as brushite is a metastable CP phase and their biological applications were studied thoroughly [34]. The main components of the brushite cement system can be classified as an acidic phosphate source, an alkaline calcium source and water. Generally, β-TCP is used as an alkaline component and MPCM is used acidic component of the brushite cement. In the last few decades, different types of calcium sources and phosphate sources have been examined to increase their mechanical properties and control their setting mechanisms. Similar to the other CPCs, they are also prepared with several additives to achieve stable cement. The typical additives that are used in brushite cement are as follows; the pyrophosphates are used to regulate setting reactions; carboxylates are used as retardants; polymers are used to improve injectability and cohesion of the cement and mechanical properties of the end-product; sulfates are used to promote the setting reaction [29].

1.2.3.2 Apatite Cements

Like the brushite cement, apatite cement is precipitated after certain CaP solids are mixed with water and harden to non-stoichiometric hydroxyapatite($Ca_{10}(PO_4)_6(OH)_2$) (also called calcium deficient hydroxyapatite) with a Ca/P ratio of 1.5 to 1.67 [7, 16, 18, 32]. CDHAp is formed with a low crystallinity in an aqueous environment like the bone and teeth minerals. This property is attributed to the excellent biocompatibility, bioactivity and osteoconduction features of apatite cement [35]. Like the brushite cement, a chemical or setting reaction occurs between a solid phase and liquid mass when mixed to form a paste-like structure. However, compared to the brushite cement, the solubility of the apatite cements are lower in the physiological pH of the human body [36]. The setting reaction mechanism starts with the CaP source's dissolution and when the supersaturation level is reached, reprecipitation of new CaP crystals occurs in the system [37]. Reprecipitated CaP crystals have needle-like or

plate-like morphology and the hardening of the cement paste occurs via the interlocking mechanism related to morphological changes after cement reaction [38]. The morphological changes within the CPC enable the intrinsic microporous formation, which helps the biological fluids to migrate inside the structure and increases the resorption rate of the CPC part to accelerate the bone formation when it is implanted in the body [39, 40].

Components of the CPCs are not only solid CaP and liquid water phases. Considering the kinetics of the cement type reaction, different types of additives are used to regulate the setting reaction of CPCs. Thermodynamically, it is possible to predict the final product of the cement reactions; however kinetic of the reaction may change and these changes may lead to several structural differentiation and different setting times. The studies primarily focus on the crystallinity of the final product, the initial particle size of the reactants, the temperature and the effect of additive material [32]. Setting time is an critical issue for clinical applications. Setting time should be neither fast nor slow for surgical operations. Fast setting reactions prevent injectability due to the hardening of the CPC, while slow setting reactions delay the operation [37]. To decrease the setting time, the following factors are increasing reaction kinetics: smaller particle size, low crystallinity, accelerators in the liquid and solid composition, higher temperature and low liquid to powder ratio (L/P ratio or LPR) [36]. Moreover, a standard method to decrease setting time is adding a common ion-containing reactant such as Na_2HPO_4 and/or formerly precipitated HAp seeds to accelerate reaction kinetics [41].

The cohesion of the CPC requires hardening before disintegration into small particles [42]. This situation is achievable with the help of additive materials that increase particle-particle interaction. The factors similar to setting time reduction can be applied for cohesion. Additionally, increasing the viscosity of the liquid phase improves the cohesion of CPC. Generally, polymers such as sodium alginate, hydroxypropyl methylcellulose, hyaluronic acid, chitosan and modified starch improve cohesion properties [32].

TTCP-based apatite cements are frequently used as in multi-solid component cement systems and rarely employed as a single solid component in cement applications. Hydrolysis of single-component TTCP can be seen Equation (1.1) below:

$$\mathrm{Ca_4(PO_4)_2O + 3\,H_2O \rightarrow Ca_9(HPO_4)(PO_4)_5(OH) + Ca(OH)_2} \tag{1.1}$$

When the TTCP phase is the only solid phase in the CPC, a complete hydrolysis reaction cannot be seen unless the ambient temperature is above 80 °C. This situation shows that TTCP shows no hydrolysis behavior while having the highest solubility in an aqueous environment among CaP at pH < 4. This phenomenon might be related to the thin layer formation of HA around TTCP particles that inhibit further water migration into the TTCP particles [31]. The prolonged ball-milling procedure enables single-component TTCP cements to be used by resulting in the amorphization of the crystal and increased kinetic solubility [43]. However, $Ca(OH)_2$ formation increases the alkalinity of the environment, which may harm the implanted tissue. Multi-component TTCP cements are more common and can be combined with a lower Ca/P ratio of CaPs such as monetite or brushites [30]. It is possible to obtain stoichiometric HAp by mixing the components accordingly. Hydrolysis of the multi-component cement can be seen Equation (1.2) as follows:

$$\mathrm{Ca_4(PO_4)_2O + CaHPO_4 \cdot 2\,(H_2O) \rightarrow Ca_5(PO_4)_3OH} \tag{1.2}$$

This reaction takes place initial dissolution of monetite that results in the formation of CDHAp. Further dissolution of TTCP particles leads to stoichiometric HAp by accumulating Ca ions on previously precipitated CDHAp [30]. The reaction kinetics can be controlled by particle size distributions of the components, mixing ratio of the reactants and increasing the solution's salinity.

α-TCP-based apatite cements are single-component cements that show hydration behavior when mixed with the water solution. The final product of the cement reaction is CDHAp and Ca/P ratios of CDHAp change between 1.5 and 1.67. The cement reaction of α-TCP can be seen in the Equation (1.3) as follows:

$$\mathrm{3\alpha - Ca_3(PO_4)_2 + H_2O \rightarrow Ca_9(HPO_4)(PO_4)_5(OH)} \tag{1.3}$$

Hydrolysis of α-TCP follows three identical steps: wetting and dissolution of α-TCP, nucleation of HAp crystals and growth of HAp crystals according to the isothermal

calorimetric studies [38]. The temperature of the hydrolysis reaction enormously affects reaction kinetic by decreasing the duration of the setting reaction. The effect of the particle size of the initial α-TCP also influences the hydrolysis of α-TCP. Reducing powder size or increasing the specific surface area leads to an increase in the reactivity of α-TCP [44]. Additionally, calcination of α-TCP postpones the setting reaction by removing nanosized defects at the α-TCP powders, which results in the annihilation of nucleation sites and the increase in the crystallinity of α-TCP powders, resulting in a decrease in dissolution [43]. As discussed above, many factors can influence the kinetics of the setting reaction of α-TCP, as represented above. The factors affecting reaction kinetics can be classified as particle size, temperature, the crystallinity of α-TCP and composition. Also, these properties strongly influence the injectability of the CPCs [36].

1.3 Injectability/Shaping Ability of Calcium Phosphate Cements

For successful surgical operation through in-situ (defect filling) hardening or for ex-situ shaping (3D printed analogous scaffolds development) some clinical and physical requirements should be achieved for cement pastes. There are several factors for direct application of bone cements to fulfill the requirements of the surgical procedure in a physical or biological aspect [45]. The bone cement should meet the four conditions: Adjustable setting time, sufficient working time, anti-washout property in the physiological environment and adequate mechanical properties. Setting time is crucial for bone cement applications to satisfy surgical operations in clinically relevant time span. A fast-setting time may inhibit the injectability of bone cement and prevent the complete delivery of the bone cement to the surgical area. The bone cement with a long-setting time may be delivered to the surgical zone completely; however, preserving mechanical stability would not be possible for the bone cement if it takes too much time to harden [37, 45].

The bone cement preparation time and the cement delivery to the bone defect are called the working time, which the bone defect filling operation is strongly dependent on. Generally, the working time should be long-enough to allow placement and adjustment of the bone cement inside the surgical area. Liquid to Powder ratio (LPR), the liquid and solid phase composition and the particle size affect the setting time of bone cement, thus the working time [46]. The anti-washout property of bone cement is another crucial factor. When bone cement is injected into the bone fracture zone, it should maintain its shape and place by resisting the internal body flow. In case of low viscosity, the particles that form the bone cements may be removed from the main body and the original shape may deform [47]. Bone cements generally have poor mechanical properties due to their brittleness and low strength, preventing them from being used in load-bearing applications. For bone cement to be used as a bone filler for a certain time, it should meet the mechanical requirements of the mechanical properties of the implanted tissue. Usually, bone cement substitutes the cancellous (porous) bone in surgical operations. A bone cement phase incorporated with polymeric materials with a composite-like structure may exhibit improved mechanical properties as a filler cement. The cooperation of biodegradable polymeric materials

with bone cement compromises the biological response of the material, enhancing mechanical properties while showing no adverse tissue response [48, 49].

In addition to all the before mentioned physical requirements for the bone cements, the injectability of the bone cements is another critical issue for both a bone defect filling operation and scaffold construction. Injectable CPCs or CSCs are clinically used in maxillofacial (locations higher than neck) surgeries. In contrast, CPC is injected into the bone to fill the bone fracture area and accelerate the healing process of the bone [50]. Additionally, the hydration mechanism of the bone cements and the versatility of the cement products make them attractive materials for different techniques rather than injectable bone cement, such as the scaffold fabrication. Scaffold fabrication can be achieved by numerous methods such as leaching, foaming, emulsion, freeze-drying templates and rapid prototyping methods [51]. Specific rapid prototyping methods require injectability for the scaffold fabrication. In the following part critical factors for shaping operations of cement pastes (solid:liquid mixtures) will be discussed, which can be simply referred as injectability characteristics/parameters.

1.3.1 Effect of Packing Fraction of Powder and Liquid to Powder Ratio

A powder network is strongly related to maximum packing solid volume fraction SVF_{max}. The liquid should fill the voids between the particles to have a flowable solid-liquid network. The increased amount of a liquid in such a network increases the distance between particles and initiates the flow of the network. Thus, when LPR increases, the powder network will be readily flowable; however, increased amounts of LPR will create more porosity which lowers the mechanical properties of the paste. Generally, increasing powder SVF_{max} is a better approach to obtaining better injectability values. SVF_{max} can be adjusted by the following parameters: particle size, particle size distribution and shape [50]. Particle size does not directly affect the packing ability of powders. The monodisperse powder network typically has a nominal SVF_{max} around 0.64 [52]. Using finer particles may cause agglomeration, which reduces SVF_{max}; thus, it prevents injectability [53]. Generally, reducing particle size increases the viscosity of cement or paste, affecting the permeability of the powder network. Decreasing powder network permeability improves the injectability of the

system until, to some extent, agglomeration starts [54].

Particle size distribution is essential to increase SVF_{max} by adding smaller particles different than bulk powder. Permeability of the powder network decrease as the smaller particles fill the space between the larger bulk powder network; thus, it increases the injectability of the system. The distribution of fine particles along with coarse bulk networks can be optimized to have an ideal SVF_{max} for the powder network [52]. It was investigated that the injectability of pastes with α-TCP powders with different sizes and distributions influenced injectability [55]. However, there is no general ideal formula for calculating the proportion of fine particles to coarse particles in a bimodal powder network, as other independent factors can be influential.

Particle shape is strongly related to the SVF_{max} since spherical particles will have higher packing efficiency compared to the irregular particles [56]. It was noted that certain geometric shapes (e.g., cubes and parallelepipeds) would have reached higher SVF_{max} compared to the spherical particles. Nevertheless, it is not generally possible to obtain CaP with geometrical features.

1.3.2 Effect of Particle-Particle Interaction

Particle-particle interactions excessively occur in the powder network and these interactions impact the flowability of the cement paste. There are two factors, which are considered as particle-particle interactions, influence the flowability of the cement paste: Colloidal interactions and direct frictional contact [50]. To assess the critical effect of colloidal interactions between the particles, the particles that form a particle network should be less than 10 μm in size [57]. α-TCP powders (employed in this study) synthesized via solid-state reactions typically have a particle size bigger than 10 μm as-synthesized condition [58].

Direct frictional contact is a significant influencing factor dependent on the roughness of the particle and SVF of the particle network. Increasing the LPR ratio reduces the friction between particles, leading to better injectability. It is reported that using a lubricating agent, glycerol, improved the injectability of the paste by reducing the frictional contact [59].

1.3.3 Effect of Setting (Cement) Reaction

Setting reaction is a critical factor that influences the particle-particle interactions due to the change in morphology of the newly crystallized HAp phase. Precipitated HAp particles have a needle-like structure that increases the powder's roughness and they are mechanically interlocked in the powder network. Thus, it decreases the injectability of the paste [50]. This situation in the powder network would change the permeability and flowability of the powders. Eventually, a phenomenon called phase separation starts to occur [60]. Phase separation causes different LPRs along with the syringe. It is known that reducing LPR reduces the setting time of CPC and the injectability of the paste alters as time passes once the paste is prepared [54]. The ideal case for the injectability is changing the setting reaction to occur until all paste or bone cement is used.

1.3.4 Effect of Extrusion Parameters

The injectability of the cement paste can be altered by changing extrusion parameters. Generally, reducing the inner diameter by assembling a needle at the end of the syringe reduces the injectability of the cement paste [61]. In a former study, it is reported that changing the tip's size does not affect the injectability of the cement paste very much. Still, the geometry of the tip strongly influences the injectability [60]. Increasing the extrusion rate by applying a higher load by preventing the liquid phase from migrating increases injectability [62]. It is also essential to have a homogenous paste to be forced through the syringe since LPR strongly affects the setting reaction; thus injectability. In this sense, the blending of pre-cement mixture can be considered as an extrusion parameter and it is a critical parameter in preventing the phase separation inside the syringe [50].

1.3.5 Effect of Viscosity

Viscosity can be defined as the resistance of a fluid when the shear stress is applied to the system. For an injectable system, the paste's rheological behavior depends on the viscosity of the liquid phase and the viscosity of the paste. Increasing the viscosity of the liquid phase improves the injectability of the paste by preventing or limiting phase separation [63, 64, 65]. The addition of polymeric binders can alter the viscosity of the liquid phase. Also, the viscous binder helps the cohesion property of the paste in exchange for higher load parameters for the cement paste [63]. In a previous study, hydroxyethyl starch, sodium dextran sulfate, cyclodextrin, alginic acid, polyvinylpyrrolidone, hyaluronic acid and chondroitin sulfate are used as polymeric binder either as a surfactant or a viscosifier in the powder network system [66]. When LPR is 0.35, the addition of polymeric binder increases the injectability in most cases; when LPR is 0.4, no significant change in injectability is observed for the cement.

In another study, anti-washout agents were studied to evaluate the cement paste's structural stability [67]. Chitosan, sodium alginate and modified starch were used as anti-washout agents and they all increased the viscosity of the cement paste. All polymeric binders improved the anti-washout property and the injectability of the CPCs until certain content; then, a decrease in the injectability of CPCs was observed while the anti-washout property remained the same or improved after the addition of more anti-washout agents in the solid component of the CPC.

Environmentally sensitive hydrogels, such as those given above, show great potential to change the viscosity of liquid components by stimulating them accordingly [68]. The environmental crosslinking mechanism can be achieved with pH stimuli in the system, closely related to temperature-sensitive stimuli or electrical and light-sensitive stimuli. Among environmental sensitive hydrogels, thermoresponsive hydrogels are easy to handle in biomedical applications since they do not need a complicated cross-linking mechanism compared to the other hydrogels [69]. Thermoresponsive hydrogels show a change in gelling behavior when temperature fluctuations occur in the systems. By adjusting the concentration of polymeric binders, it is possible to change the gelling temperature of hydrogel systems. For a polymer to show

gelation behavior, it should exceed a specific temperature and that threshold is called lower critical solution temperature (LCST). Above LCST, their viscosity significantly increases compared to the initial condition. Widely used polymers are methylcellulose, chitosan, dextran, xyloglucan, gelatin, polyethylene oxide-polypropylene oxide-polyethylene oxide (PEO-PPO-PEO) copolymer called Pluronic®F127 are available as a thermoresponsive hydrogel.

It is crucial to understand the behavior of the liquid phase when it is prepared with the polymeric binder. Pluronic F127 shows inverse thermoresponsive behavior when the critical micelle concentration exceeds and entanglement occurs between PEO and PPO parts since LCST of PEO and PPO are different [78]. Further, an increase in temperature leads to gelation of the polymer. The concentration of the Pluronic F127 in the solution is a parameter for gelation temperature. According to a study, Pluronicd F127 concentration should be over 15 wt.% for gelation to occur when mixed with UP water [70]. Another essential feature of Pluronic F127 is gelation behavior close to the physiological temperature of the human body and it is reported that Pluronic F127 solutions at 15 wt.%, 20 wt.% and 25 wt.% and 30 wt.% exhibit gelation at 30 °C, 27 °C, 19 °C and 10 °C respectively. Additionally, the viscosity of the liquid solutions prepared with Pluronic F127 and UP water increases as polymeric binder content increases, adjusting to the liquid solution's viscosity [71]. Using phosphate buffer during the preparation of Pluronic F127 decreases the gelation temperature of the solution compared to when the solution is only prepared with UP water [72]. This indicates that ions present in the solution may alter the gelation behavior of the Pluronic F127 solutions. Pluronic F127 had been utilized in CPC systems a liquid phase/component and the use of Pluronic F127 prevented the phase separation problem in the CPC by increasing the viscosity of the liquid phase [73]. The injectability trend of the CPC paste prepared with only DI water showed that the necessary load to move the plunger continuously increased due to phase separation. In contrast, the CPC paste was prepared with 20 wt.% Pluronic F127 liquid solution showed a steady-state trend by keeping the L/P ratio at 0.35 ml/g and temperature at 0 °C during the injection. However, as the temperature of the CPC is increased to 20 °C, the requisite load was increased even, so the CPC paste showed a steady-state trend during injection due to gelation of the Pluronic F127. In rapid prototyping applications, such as

robocasting or direct-ink writing, crosslinking of the binder is necessary to give structural stability to the printed scaffolds [50]. For this purpose, it is reported that using Pluronic F127 as a polymeric binder in a liquid solution is beneficial for 3D printing applications by providing structural strength to the as-printed state of the scaffold [63].

1.4 3D Printing of Bioceramics

Numerous ceramic materials are extensively used due to their excellent biological performance, chemical stability, high strength and hardness, thermally durability and high optical, electrical and magnetic properties related to applications. Engineering ceramic parts are generally produced by starting from powder and powders are employed with a binder or without a binder and other additives for shaping purposes. Currently utilized technologies for such applications include injection molding, tape casting, die pressing, or similar applications [74]. These methods commonly require sintering at high temperatures to achieve higher densification than initial green body states. This might limit producing highly complex shapes and interconnected structures such as scaffolds. Additive manufacturing (AM) technologies such as the three-dimensional (3D) printing method enable the fabrication of ceramic components which have complex geometries point-by-point, line-by-line, or layer-by-layer with unique features [75].

Several 3D Printing methods can produce ceramic components; each production approach has a different resolution, surface quality, process cost and feedstock cost for end-product. 3D printing methods are classified by considering the forming techniques of feedstock ceramic material. Feeding stock material used in 3D printing could be slurry-based, powder-based and bulk solid-based [76]. However, for bone tissue engineering, main 3D printing methods can be categorized as inkjet writing, stereolithography (SLA), direct ink writing (DIW) for slurry-based systems; selective laser sintering (SLS) and selective laser melting (SLM) for powder-based systems and fused deposition modeling (FDM) for bulk solid-based systems [76, 77, 78].

1.4.1 Selective Laser Sintering

As its name implies, in the selective laser sintering (SLS) method, a laser beam with high energy is utilized as an energy source and the beam targets the surface of the powder bed. Heated ceramic particles undergo sintering (i.e., interparticle fusion) reaction [76]. Once the layer is formed after sintering, a new powder layer is spread on top of the previous layer, repetitively, laser sintering is applied on the powder bed surface. The disadvantages of the SLS process are low resolution (limited to particle size), poor surface finish and micro porosities after printing. Having microporosities in the printed scaffold is not always avoided since it helps nutrient and fluid diffusion within the structure for biological applications.

SLS method requires the cooperation of ceramic particles with polymeric binders for printing ceramic components by considering the high melting temperatures of ceramic powders. Since this process does not involve the melting of ceramic powders, during operation, macroporosities remain even after the process [78]. Coating ceramic powders with polymeric binders provide structural integrity during the fabrication of the scaffolds [79]. Using bioresorbable organic polymeric binders increases the osteoconductivity of the printed scaffold besides the availability of creating complex architecture. However, it is impossible for metastable ceramic powders, such as α-TCP and TTCP, to be used in SLS because of high heat generation.

1.4.2 Stereolithography

Stereolithography (SLA) is one of the 3D printing techniques which is widely used in the world [80]. Polymerization (liquid monomers into a solid resin) mechanism activated by the light-stimuli advances point-to-point, line-to-line, or layer-to-layer to build up the 3D structure. As polymerization is completed for one layer, the structure can stand without any support or with the reinforcement of another component, depending on the SLA method. Compared to the other 3D printing techniques, SLA printed components have high surface quality and an exquisite resolution that can reach a micrometer scale.

SLA requires photopolymerization of a photocurable polymer, ceramic slurries are prepared by mixing polymer medium and ceramic particles [81, 82]. A ceramic suspension is generally utilized with surfactants and additives to disperse ceramic particles homogenously. When the suspension is exposed to light stimuli, photocurable polymers surrounding the ceramic particles start to crosslink and the layer-by-layer build-up process is achieved. Later on, the printed green body is generally fired for the densification process and removing organic polymers from the printed components [83].

Although using the SLA method for printing scaffolds seems advantageous, this technique has limitations. Since the SLA process involves the photopolymerization of a polymer, it is limited to photocurable polymers [77]. Additionally, printed green bodies generally require a firing process and eliminate the use of metastable ceramic particles. HAp, β-TCP are commonly used CaP powders for this technique [84, 85].

1.4.3 Fused Deposition Modeling

The fused deposition method (FDM) is one of the most commonly used 3D printing processes globally. FDM involves the utilization of thermoplastic polymers in filament form while the filament is constantly supplied to the heated nozzle. The temperature of the heated nozzle is set to just above the melting point of thermoplastic polymers to have adequate viscosity for the medium. After extrusion of viscous polymer, it solidifies when it reaches the platform. The cooperation of ceramic powders with polymeric materials is accomplished without using any liquid medium. However, for an easy extrusion of ceramic-polymer filament, polymeric binder can take up space of around 40-45 vol% is a necessity for this application [78]. Furthermore, this process includes optimizing thermoplastic content, filament fabrication, processing parameters during printing and firing treatment for removing polymers from the printed structure and sintering the green body. Since it involves the firing process after printing, this limits the number of CaP powders used.

1.4.4 Inkjet Writing

Inkjet writing (IJP) is a commonly used technique, especially for 3D printing of ceramics. IJP utilizes liquid phase material (or ink) in droplet form by ejecting it onto the powder bed. When an ink droplet contacts with the powder, the powder solidifies. As it solidifies, the powder bed moves one level below and the same procedure is repeated until the entire structure is printed without any support. The printed structure generally undergoes post-processing to remove the excessive binder and give sufficient strength [85].

CaPs bioceramics are widely used for this technique because of their excellent osteoconductive property due to their chemical resemblance with the natural bone tissue. Binder-based ink temporarily holds the structure together until the sintering of the green body. Additionally, the green body may be subjected to the hydration process, eliminating high energy consumption post-processes for specific CaPs [76, 78]. Various binders such as phosphoric acid solution and polyvinyl alcohol (PVA) are utilized for IJP.

Advantages of the IJP process are low cost, convenient processing and versatility of material selection, making IJP a good candidate for the 3D printing of ceramic components. Furthermore, the surface quality of printed 3D structures by this technique is better compared to previous methods.

1.4.5 Direct-Ink Writing

Direct-Ink Writing (DIW) or known as robocasting (RC), is a technique for processing viscous paste-like materials similar to injectable bone cements [76]. DIW method requires the development of highly viscous ink or paste and extrusion of prepared paste through the nozzle at room temperature to build up 3D structure after deposition and representation of process shown in Figure 1.6 [89]. Like the FDM technique, direct layer-by-layer deposition of the material is achieved via moving nozzles. DIW provides an inexpensive and faster production. They have viscous semi-liquid pastes that help the printed structure's shape retention without the need for any support. Still, some printed parts may be subjected to a sintering process for further densification.

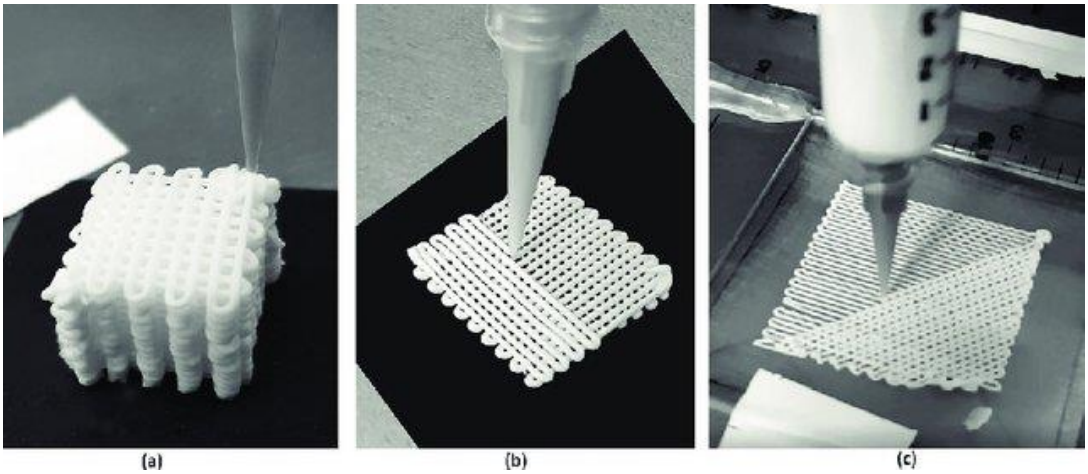


Figure 1.6: Represantive view of Direct-Ink Writing process, 3D printing of CaP scaffolds [89].

Remarkably, the DIW technique is carried out at room temperature; it offers a wide range of CaPs and metastable CaPs, especially α-TCP, to be used in 3D printing applications [63, 86, 87, 88, 89, 90]. Transportation of the solid ceramic powders is ensured with a liquid medium, for most cases with DI water, along with some additives. Previously reported injectability issues are present for this technique and the improvement of cement pastes is achieved by resolving related injectability problems. In a study conducted by Huh, J. et al., α-TCP scaffolds were printed with the cooperation of gelatin and water (25 wt.%) employed to give sufficient viscosity to a liquid medium for shape retention of the scaffold [88]. According to complex viscosity data with varying temperature (no data for solid:liquid composition), as the barrel temperature increases, complex viscosity of the pastes drops from 30 kPa.s to 1 kPa.s. Additionally, another plot had been made by changing pressure from 50 kPa to 300 kPa and barrel temperatures of 15, 25, 35 ,and 45 °C. In the process, printing speed is kept constant around 12.5 mm/s and nozzle diameter is set to 400 µm. Findings show that an optimum value between barrel temperature, printing speed and pneumatic is found by trial and error methods for printing scaffolds. Complete hydration of scaffolds was apt only after adding crosslinking agent for gelatin. In another study conducted by Maazouz, Y. et al., the α-TCP powder was used as a solid component of the paste and gelatin solution (10 wt.%) was prepared with DI water for DIW application [89]. The presence of gelatin decreased the micro/nano porosity

level of the scaffolds from 55.7% (pure TCP scaffold) to 45.8% for non-crosslinked gelatin-TCP scaffold and to 41.4% for crosslinked gelatin-TCP scaffold (all scaffolds were hydrated at room temperature for 7 days). Similarly, pore entrance size decreased from 2.0 μm for TCP scaffold to 0.5 μm for non-crosslinked gelatin-TCP scaffold and further to 0.1 μm for crosslinked gelation-TCP scaffold. Even though both crosslinked and non-crosslinked α-TCP scaffolds were hardened in water after seven days, crosslinked gelatin-TCP scaffolds showed higher compressive strength around 16 MPa while non-crosslinked gelatin-TCP scaffold had compressive strength around 10 MPa.

In a study conducted by Lee, G. et al., 2 wt.% alginate solution was used as liquid content of the cement-ink/paste [86]. The average particle size of TCP powder was measured as 4.79 μm. Powder to liquid ratios between 1.0 and 2.0 g/g were possible. It is reported that higher than 2.0 g/g powder to liquid ratios of cement-inks could not be printed due to high viscosity. Scaffolds were fabricated with different gauge sizes (23-27G) successfully. Rest of the study is mainly related to biological performance of printed scaffolds.

Pluronic F127 have been used in 3D applications due to its easily controllable viscosity behavior with a temperature change [63, 87, 90]. In a study conducted by Franco, J. et al., the concentration of Pluronic F127 in water varied between 20 wt.% and 30 wt.% for the liquid component of the ceramic pastes [63]. Solid component of the paste is chosen as HAp with average particle size of 2.4 μm and β-TCP with average particle size of 1.6 μm. It was reported that a paste prepared 20 wt.% Pluronic F127 concentration requires less load (45 N for 8 mm/s) than 30 wt.% Pluronic F127 solutions (75 N for 8mm/s) for any printing speed. Additonally, in order to see the effect of nozzle geometry, cone and standard tips were used. For same cement formulation and printing parameters, while 5 N pushing powder was sufficient to flow the paste, for standard tip the force required to ensure flowability of the paste was 30 N. Furthermore, it is reported that as the printing speed of the paste is gradually increased from 4 mm/s to 15 mm/s, the pushing force is also increased from 30 N to 50 N. In another study with Pluronic F127 conducted by Barba, A. et al., to ob-

serve effect of nozzle tip size, α-TCP (starting mean powder particle size of 2.8 μm) scaffolds were printed with 30 wt.% Pluronic F127 with LPR of 0.65 and nozzle tip sizes of 250 and 450 μm were used [87]. Printed scaffolds are hydrated for seven days for completion of hydration. Compression test results suggested that increasing resolution during printing (decreasing tip size) slightly improved the compressive strength of the hydrated scaffolds from 4 MPa to 5 MPa. Total porosities measured by mercury-intrusion porosimetry of printed scaffolds with different nozzle tips were almost identical (64.8% and 65.4% for 450 and 250 μm respectively). Additionally, FT-IR data showed that Pluronic F127 is washed away from a scaffold at the end of 7 days.

1.5 Objective and Rationale of the Thesis

Bone related diseases or bone fractures are commonly experienced in the population and there are several biomedical applications present to augment/heal the injured bone tissue. Bioceramics are good material of choice for such operations due to its biocompatibility and similar mechanical properties of the natural bone tissue. Bone grafts were developed based on these properties and they can be harvested from patient or produced synthetically.

Bone cements (synthetic bone grafts) are frequently used for bone defect filling operations especially for irregular bone defects. Bone cement can be utilized as a putty material or injecting through the needle into the damaged bone tissue. Due its chemical nature, synthetic bone cements set and converts to new hardened phase. Based on the bone cement formulation, setting reaction occurs as polymerization reaction for polymer-based bone cements (such as polymethylmethacrylate or PMMA) or hydration reaction for ceramic based bone cements (such as Calcium Phosphate Cement or CPC). While polymeric based bone cements undergo a in situ hardening, they show highly exothermic characteristic and they do not degrade with time in biological environment. On the contrary, ceramic based bone cements show bioresorbable characteristic which dissolves in physiological environment and exhibit much lower heat generation during the setting reaction of the bone cement.

Calcium phosphate cements are research of interest since CPC-end products show chemical resemblances of the inorganic component of the natural bone known as calcium deficient or carbonated hydroxyapatite (HAp or $Ca_{10}(PO_4)_6(OH)_2$). Clinically used cements are prepared as multi-component or single component system and both cement formulations set to calcium deficient HAp (CDHAp) as the cement-end product. Best known single cement precursor α-tricalcium phosphate (α-TCP or $Ca_3(PO_4)_2$) harden to biomimetic CDHAp when it is combined with water. Relatively controllable reaction kinetics, excellent bioactivity and the simplicity of conversion mechanism enable them to be utilized as the bone cements. Therefore, CPC can be used as graft material for irregular defect filling operations. There are a variety of number products with clinical approval for in-vivo (within the body) use.

Besides direct use of CPCs as injectable bone graft, these cement systems can be also employed for processing and obtaining bioceramic structures as investigated in this thesis. The main objective of the thesis is to explore the potential of the direct use calcium phosphate cements in obtaining irregular or geometrically complex bioceramic structures or forms by 3D printing. In other words, hydration driven cement reaction is used to provide in-situ shaping ability during and after printing process. In that sense proposed approach is unique, because a consolidated bioceramic form of any desired shape can be obtained without sintering. A major part of the experimental studies in the thesis focus on validation of this rationale and establishing processing details for Ink-Jet printing involving synthesis of calcium phosphate precursor, formulation of a printable ink formulation, understanding the extent of cement-conversion for printed preforms and chemical and microstructural characterization of printed structures.

The printing precursor, i.e cement component, was phase pure and reactive α-TCP custom synthesized to be used in cement-based printing pastes. Initial versions of printing pastes were prepared with Pluronic F127:water and Alginate: water solutions and α-TCP and their injectability and structural integrity upon injecting was assessed in printing-simulating conditions by manual printing studies. Optimized cements paste was adapted for Ink-Jet printing to in fabricate macroporous scaffolds, via layer by layer construction of an arbitrarily chosen mesh-like 3D construct. Meanwhile, some cement formulation was modified with calcium sulfate hemihydrate (CSH or

$CaSO_4 \cdot \frac{1}{2} H_2O$) by blending α-TCP at different weight ratios. The objective adding another cement precursor was two-fold. First, to provide a faster and more effective setting and hardening in practically shorter and more relevant time span. Additionally, to improve structural integrity and mechanical properties in as-printed condition. The microstructural modification upon addition CSH has been also explored; pure α-TCP and dual-cement containing printed structures has been comparatively investigated for cement conversion efficiency and mechanical properties.

CHAPTER 2

MATERIALS AND METHODS

The main constitute of 3D printed scaffolds, i.e. α-tricalcium phosphate (α-$Ca_3(PO_4)_2$ or α-TCP) powders were synthesized by carrying out solid state reaction. In this chapter, experimental procedures for synthesis of phase pure α-TCP by different routes; preparation of α-TCP/water/alginate, α-TCP/water/Poloxamer 407 (α-TCP/water/ Pluronic F127) printings pastes by using previously synthesized α-TCP powders and adaptation of optimized α-TCP/water/ Pluronic F127 paste formulations into 3D printing operation are described and explained in detail. Furthermore, the analytically material characterization methods used in this thesis are presented.

2.1 Materials

α-TCP powders were synthesized by using calcium carbonate ($CaCO_3$, reagent grade Merck, Germany) as the calcium source and phosphoric acid (H_3PO_4 reagent grade, 85 wt.%, Merck, Germany) as the phosphate source. First, dicalcium phosphate anhydrous ($CaHPO_4$, DCPA or Monetite) were synthesized. Some amount of chemically synthesized monetite was fired at 600 °C in order to obtain calcium pyrophosphate ($Ca_2P_2O_7$ or CPP). Solid state reactions at 1200 °C in open air were conducted to stoichiometric powder mixture of $CaCO_3$ and $CaHPO_4$ or stoichiometric powder mixtures of $CaCO_3$ and $Ca_2P_2O_7$ to obtain phase pure α-TCP. Liquid phases of cement pastes are prepared by mixing DI water with alginate (Sigma Aldrich, USA) or mixing DI water with Pluronic F127 (Sigma Aldrich, USA) at different weight ratios.

2.2 Methods

2.2.1 Synthesis of α-TCP Powder

Monetite ($CaHPO_4$) is synthesized after calcination of 36 g of calcium carbonate ($CaCO_3$, Merck, Germany) and by adding excess deionized water (DI water) to the calcination product (CaO), followed by addition of aqueous phosphoric acid (H_3PO_4, Merck, Germany, 85 wt. %).

In the preparation of $CaHPO_4$, first $Ca(OH)_2$ is obtained by following steps; calcination of $CaCO_3$ to CaO at 1010 °C for 2 h followed by immersing of CaO (approximately 20.20 g) into 400 ml DI water and mixed thoroughly for 1h for completion of the reaction. 42.15 g (or 24.8 ml) of H_3PO_4 was added to the system at molar ratio of 1:1 with $Ca(OH)_2$ while keeping temperature of the slurry at 60 °C for additional 1.5 hours to obtain $CaHPO_4$. The slurry is vacuum filtered and then dried at 70 °C for 2 days. Resultant powder was weighed 45.5 g and divided into two batches to observe the effect of removing chemically bounded H_2O from CaP precursors. This can be critical for phase purity and properties of the final end-product of α-TCP. While first batch is used as-prepared condition; second batch of resultant powder was fired at 600 °C for 1h.

Alpha tricalcium phosphate (α-TCP) was synthesized by the following two different routes: For the first batch, $CaHPO_4$ and starting powder of $CaCO_3$ with molar ratio of 2:1 were mixed and milled simultaneously using Turbula T2F mixer (System Schatz, Switzerland)in high density polyethylene container (HDPE or Nalgene™) in an acetone medium. After 1 h mixing, powder mixture was left to dry overnight at room temperature in open atmosphere. After drying, the powder mixture was filled into alumina crucible and fired at 1200 °C in open atmosphere for 2 h. The solid-state reaction is shown in Equation (2.1) below:

$$CaCO_3 + 2CaHPO_4 \rightarrow Ca_3(PO_4)_2 + CO_2 + H_2O \tag{2.1}$$

After 2 h-long firing the product powder was air quenched to room temperature and powder was downsized by using a hand mortar and pestle. As-synthesized α-TCP powders were additionally milled with 20 zirconia balls (1 cm in diameter) in Nalgene™ container in an acetone medium by using Turbula T2F mixer. The powder slurry was left to air dry overnight at room temperature in open atmosphere. End product of this solid-state reaction is named as TCP1. For further use, TCP1 powder was sealed and stored in desiccator. For further use, α-TCP powders were sieved down to 40 μm.

For the second batch, mixing of $Ca_2P_2O_7$ and $CaCO_3$ with molar ratio of 1:1 was done using a HDPE container (Nalgene™) in acetone medium by using Turbula T2F mixer. After 1 h mixing, powder mixture was left to dry overnight. After drying, the powder mixture was filled into alumina crucible and fired at 1200 °C in open atmosphere for 2 h. The solid-state reaction of powder mixture is given in Equation (2.2) below:

$$\mathrm{CaCO_3 + Ca_2P_2O_7 \rightarrow Ca_3(PO_4)_2 + CO_2} \tag{2.2}$$

After 2 h-long firing the product powder was air quenched to room temperature and powder was downsized by using a hand mortar and pestle. As-synthesized α-TCP powders were additionally milled with 20 zirconia balls (1 cm in diameter) in Nalgene™ container in an acetone medium by using Turbula T2F mixer. The powder slurry was left to air dry overnight at room temperature in open atmosphere. End product of this solid-state reaction is named as TCP2. For further use, TCP2 powder was sealed and stored in desiccator. For further use, α-TCP powders were sieved down to 40 μm. Overall reaction scheme is shown in Figure 2.1.

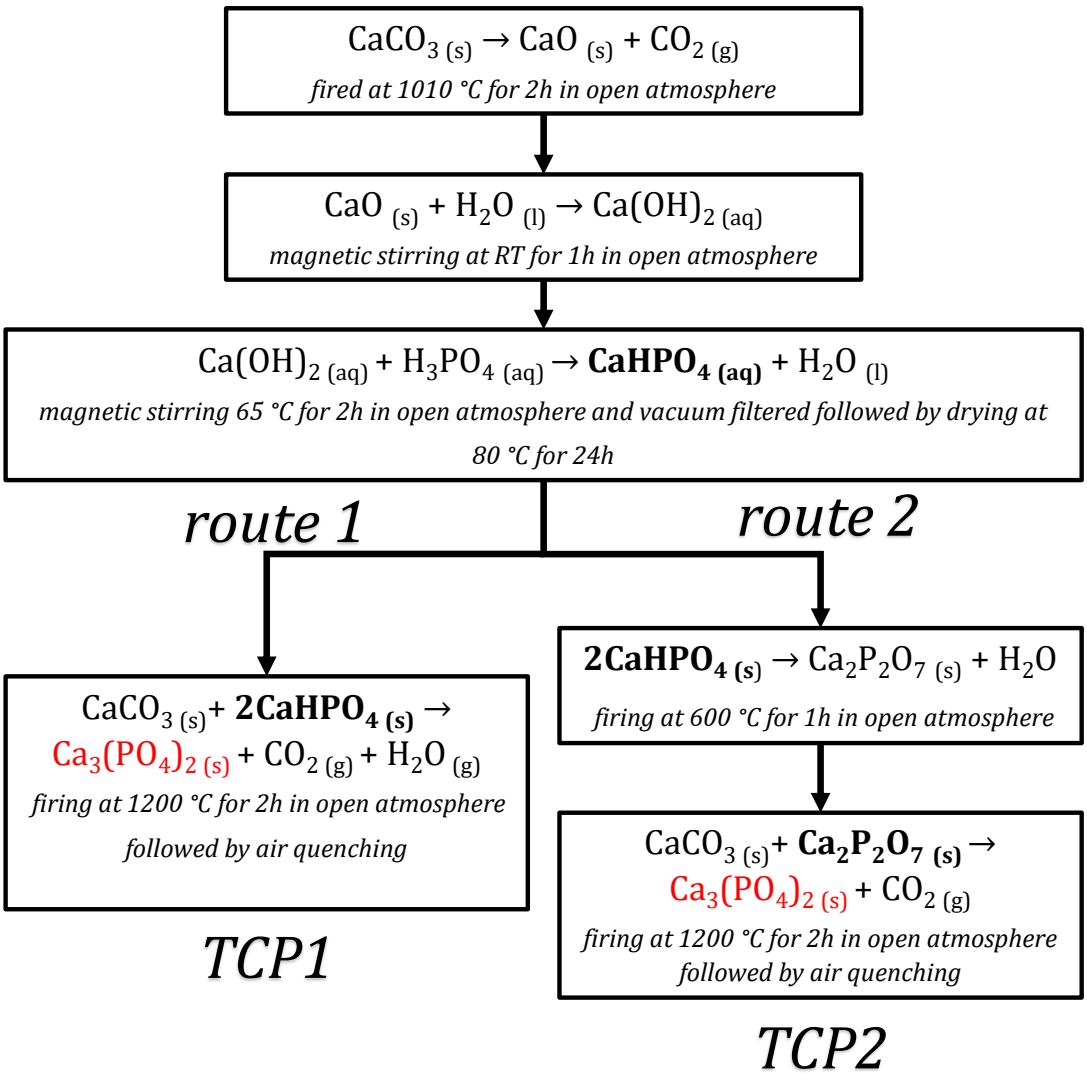


Figure 2.1: Flow chart of solid state synthesis of α-TCP by adding one additional step to compare purity of end-products and the experimental details of each step are shown.

2.2.2 Cement Paste Preparation

For the α-TCP powders to be used in 3D printing, a parametric optimization is required to obtain printable cement pastes. For this purpose, different types of water soluble polymeric additives were added to ceramic powders in order to control the viscosity of the final ceramic-polymer mixture and to achieve structural stability for printed parts during and after printing. One of the polymeric additives was 2 wt.% alginate solution that was prepared by mixing with DI water with magnetic stirrer (Hei-Tec, Heidolph). This solution was typically kept in room temperature for further use.

In addition, Pluronic F127 containing solutions were prepared at different weight ratios (20 wt.%, 25 wt.% and 30 wt.%) by mixing with DI water. Since solubility of Pluronic F127 increases at lower temperature, the liquid mixture were cooled to 0 °C inside water/ice bath and sonication was performed during storage inside of the water/ice bath. For further use, prepared Pluronic F127 solutions were stored in the refrigerator at 4 °C. The set of experiment is given with the binders that were used during the preparation of the cement paste are given in Table 2.1.

Table 2.1: Printing paste formulations with varying liquid (binder solution) to powder (α-TCP powder) ratios and binder type. Powder amount is an equivalent amount of 3 gr in all cases.

	Type of Binder			
	Pluronic F127			Alginate
Concentration in Water (wt.%)	20 wt.%	25 wt.%	30 wt.%	2 wt.%
Liquid to Powder Ratio (ml/g)	0.55	0.55	0.55	0.55
	0.6	0.6	0.6	0.6
	0.65	0.65	0.65	0.65

The injectability of the cement pastes and their shape preservability during and after printing were explored. For the cement paste preparation, liquid phase and 3 g of α-TCP powders were hand-mixed with different LPRs in 50 ml Nalgene™ container until ensuring that paste is homogeneous. Prepared pastes were delivered into 5 ml commercial syringes. In order to remove bubbles present in the calcium phosphate cement (CPC) paste, syringes barrels were gently tapped. Injectability test was conducted by pushing syringe plungers by hand. Then, injectability of the cement pastes were estimated by the following calculation.

$$Inj(\%) = (w_f - w_a)/(w_f - w_e) \tag{2.3}$$

where w_e is the weight of the empty syringe barrel, w_f is the weight of fully loaded syringe barrel and w_a is the weight of the syringe barrel after loading. The hand-injection operation took approximately 2 minutes for each test. The stability of injected pastes are crucial for 3D printing part thus, the cement pastes did not preserve their shape after injecting paste were not evaluated further.

2.2.3 3D Printing of α-TCP Scaffolds

3D printed α-TCP Scaffolds were fabricated with Bioscaffolder® (SYS+ENG, Germany). Calcium phosphate cement (CPC) inks were prepared with 25 wt.% Pluronic F127 containing liquid phase and 6 g α-TCP powder at L/P ratio of 0.6-0.7 ml/g by previously described procedure (in Section 2.2.2) of hand-mixing. Then, CPC-inks was delivered into syringe barrel (20 cc Optimum Syringe Barrels, Nordson EFD, USA). A tapered dispensing tip with inner diameter of 400 μm (Gauge 22) was used in 3D printing of scaffolds. Rectangular scaffolds (10 mm in width, 10 mm in length and 5 mm in height) were prepared with CAD Software (Solidworks, USA). The geometry of the scaffold was created by continuous fiber deposition with 1 mm distance between each fiber; then same pattern was created by rotating 90° with respect to previous layer and total of 16 layers were set to form after printing. Printing parameters for all scaffolds are given as: the nozzle size of the set as 320 μm (20% decrease due to layer overlapping), needle offset was set as 320 μm, transfer height of nozzle head was set to 4 mm, temperature of the syringe barrel was set to 17 °C. Deposition speed

of the nozzle tip varied between 4 mm/s and 12 mm/s and air pressure of the plunger varied between 1.5 and 4.5 bar during printing of the scaffolds.

Dual cement inks were prepared by loading calcium sulfate hemihydrate (Sigma Aldrich, Germany) and α-TCP powders in Nalgene HDPE container with excess acetone solution and mixing in T2F Mixer for an hour. Hybrid cement-inks were prepared by mixing weight ratios of TCP:CSH of 90:10 wt.% and 75:25 wt.%. The hybrid cement sacaffolds were called CSH10 and CSH25 for the rest of the thesis. The summary of the prepared cement-inks (described in Section 2.2.2) to be used in 3D printing of scaffolds is given in Table 2.2 with respect to solid powder composition of TCP:CSH.

Table 2.2: The composition of TCP:CSH dual-cement hybrid printing pastes. The liquid component was Pluronic F127-containing aqueous solution in all cases.

	Amount of Solid Phase		**Amount of Liquid Phase**	
Scaffold Name	TCP(CaP Cement)	CSH(CaS Cement)	DI Water	Pluronic F127
TCP	6 g	-	2.7 g	0.9 g
CSH10	5.1 g	0.9 g	2.9 g	1 g
CSH25	4.5 g	1.5 g	3.15 g	1.05 g

2.2.4 Post-Printing Treatments of 3D Printed Scaffolds and Dummy Scaffolds

Dummy scaffolds were prepared with same procedure described above (Section 2.2.2) because it was assumed that their hardening behavior is identical with 3D Printed Scaffolds. Dummy scaffolds were created by hand-injection to evaluate hardening behavior of α-TCP with excess DI water. The hand-injected dummy scaffolds were immersed in water to initiate the cement hydration at various time intervals (6 h, 12 h, 24 h, 48 h, 72 h) by keeping as-injected scaffold as the control group. Cement-end products are crushed with alumina mortar and pestle for further analyses. Cement setting time and post-treatment parameters for printed scaffolds were concluded by XRD and FTIR analyses of dummy scaffolds. The procedure described above was repeated for hybrid cement dummy scaffolds.

The 3D printed scaffolds were placed inside of the oven at 37 °C with 100% relative humidity for 24 h to achieve partial cement setting and hardening before the hydration of α-TCP scaffolds since α-TCP scaffolds may disintegrate upon direct contact with aqueous water. α-TCP scaffolds were immersed in DI water at 37 °C for 72 h. Additionally, 3D printed hybrid cements were hydrated in phosphate buffer solution (PBS) solution to ensure complete hydration of the cement precursors. The composition of the PBS solution is given in Table 2.3.

Table 2.3: PBS solution is prepared at 25 °C in 1 litre of DI water with the compounds and amounts

Compound	Solubility
$K(PO_4)$	26.22g/l
$NaCO_3$	7.78g/l

2.3 Material Characterization of Solid-State Synthesis, Cement End and Scaffold Products

2.3.1 Characterization of Solid-State Synthesis Products and Cement Products

2.3.1.1 Particle Size Analysis

Particle size of milled α-TCP powders was analyzed by using Malvern Mastersized 2000 Particle Size Analyzer. Prior to the analyses, synthesized α-TCP (or TCP2) powders were sieved down to 40 μm. For the first measurement, the particle size of α-TCP particles were measured plainly. For the second measurement, α-TCP particles were dispersed in DI water by using ultra sonic horn.

2.3.1.2 Phase Identification: X-Ray Diffraction Analysis

X-Ray Diffraction analyses for intermediate products and end products during the synthesis of α-TCP were performed for phase identification. The diffractometer (Rigaku, Germany) equipped with X-ray tube with CuKα radiation of λ:1.5418 Å which operated at 40 kV and 30 mA. XRD data were collected with step size of 0.02° and with scan speed of 2°/min within 2ϑ range of 20-50° for intermediate products and 2ϑ range of 20-40° for solid-state reactions end products. Phase identification of diffraction patterns were identified by using JCPDS cards of monetite (JCDPS PDF 00-09-080), calcium pyrophosphate (JCDPS PDF 00-09-345), α-TCP (JCDPS PDF 00-09-348) and CDHAp (JCDPS PDF 00-009-0432).

XRD data of dummy scaffolds were collected with step size of 0.02° and with scan speed of 2°/min within 2ϑ range of 10-40°. Phase identification of diffraction patterns were identified by using JCPDS cards of calcium sulfate hemihydrate (JCDPS PDF 00-23-128), calcium sulfate dihydrate (JCDPS PDF 00-33-311), α-TCP (JCDPS PDF 00-09-348) and CDHAp (JCDPS PDF 00-009-0432).

2.3.1.3 Microstructural Investigation: Scanning Electron Microscopy

The microstructure of solid-state synthesis intermediate products, end products and hydrated dummy scaffolds were investigated by a FEI Quanta 400F model field emission scanning electron microscope (SEM) at 20 kV. Cement products were investigated by following same procedure at 20 kV. Ceramic particle surfaces were coated with thin layer of gold.

2.3.1.4 Chemical Analysis: Fourier Transformed Infrared Spectroscopy

Fourier transform infrared (FT-IR) spectroscopy analyses were carried out with FT-IR Frontier spectrometer (Perkin Elmer, USA) equipped with attenuated total reflectance (ATR) aperture (Perkin Elmer, USA) for solid-state synthesis end products and hydrated dummy scaffolds. The FTIR spectra were collected between 400-4000 wavenumbers cm^{-1} with resolution of 4 cm^{-1}. Dissolution of polymeric additives at

different time intervals and chemical structure of cement end products were analyzed by using FT-IR spectra.

2.3.2 Characterization of 3D Printed Scaffolds

2.3.2.1 Mechanical Test: Compressive Strength Test

The mechanical properties of the TCP, CSH10 and CSH25 scaffolds were carried out with Mechanical Tester (Shimadzu AGS-X Universal Test Machine equipped with a load-cell of 10 kN, Japan). The uniaxial compressive tests were performed on the printed and the hydrated (immersed in DI water for 72 h) α-TCP,CSH10 and CSH25 scaffolds at a crosshead speed of 1mm/min. Typically at least five scaffolds were tested for obtaining representative data for each data set.

2.3.2.2 Archimedes Porosity Measurement

The densities of α-TCP, α-TCP:CSH scaffolds after hydration were determined by Archimedes method and compared with the theoretical densities. Total porosities of scaffolds were calculated by the following Equation (2.4):

$$\%Porosity = 1 - (bulkdensity/theoriticaldensity) \times 100 \tag{2.4}$$

The theoretical densities of the hydrated scaffolds were calculated by considering that α-TCP and CSH were fully hydrated to HAp and CSD and hybrid cement densities were calculated by the rule of mixtures. The theoretical densities of HAp and CSD are 3.10 and 2.32 $\mathrm{g/cm^3}$ respectively.

2.3.2.3 Micro Computed Topography

α-TCP and α-TCP:CSH scaffolds were scanned with micro computed tomography (Bruker μ-CT 1172, Belgium) with the application of 14.75 μm/pixel size, using aluminum filters at 167 A with voltage of 59kV. Samples were rotated 0.2° throughout 360°. Porosity and pore size distributions were calculated by using CTAn software (Bruker μ-CT, Belgium).

CHAPTER 3

SYNTHESIS AND CHARACTERIZATION OF CEMENT COMPONENT OF THE PRINTING PASTES/INKS

In this chapter,intermediate (monetite and calcium pyrophosphate) and solid-state reaction products via different routes will be characterized. Experimental procedures of different reaction schemes were given in the Chapter 2 Materials and Method. Phase analyzes of intermediate and solid-state products were performed by XRD analysis to detect the phases present after reactions, FTIR analyzes was performed to detect chemical bonding characteristics of intermediate and solid-state products; microstructures of intermediate and solid-state products were investigated by SEM. The phase purity of solid-state reaction products was elucidated by the characterization methods given above.

3.1 Characterization of Intermediate Products

$CaHPO_4$ (or monetite) was synthesized in aqueous solution by mixing $Ca(OH)_2$ and 85 wt.% H_3PO_4 in stoichiometric ratio of 1:1. Later on, the slurry was left to dry physically bounded water from the synthesized powder. The XRD pattern of the powder is given in Figure 3.1 given at the top and was matched the with monetite phase JCPDS card no 09-080. Half of the monetite was subjected to further heat treatment at 600 °C for 1 h to remove chemically bounded water from monetite. The XRD pattern of the resultant powder is given in Figure 3.1 given at the bottom and is matched with γ-calcium pyrophosphate (or γ-CPP) phase JCPDS card no 09-345.

FT-IR spectra of monetite and CPP is shown in Figure 3.2. There are several bands were observed for P-O bonds with small deviations within both samples and shown

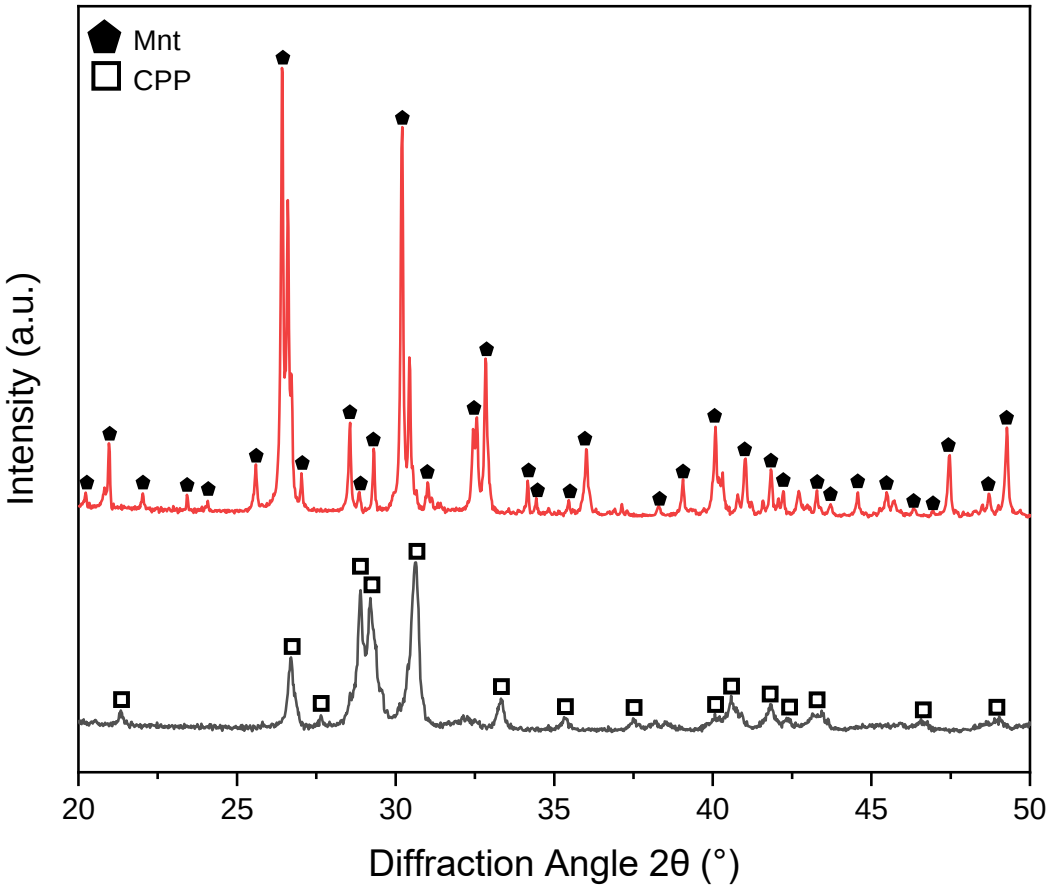


Figure 3.1: The XRD diffractograms of the intermediate products (Monetite with JCPDS 09-080 and Calcium Pyrophosphate with JCPDS 09-345 respectively] obtained as it shown in the flow chart of synthesis protocol.

as blue highlighted region. Removal of chemically bounded water can be clearly detected by the FT-IR analysis. It was reported that P-OH stretching vibrations are observed nearby 890 cm^{-1} for monetite and seen as one large broad absorption band in the FT-IR spectra [91]. Additionally, O-H bending mode band was detected as two broad absorption bands between 1300-1500 cm^{-1} That kind of band was not detected for CPP which shows that chemically bounded water is removed from monetite after heating to 600 °C for 1 hour and FT-IR spectra of γ-CPP is confirmed with the literature [92].

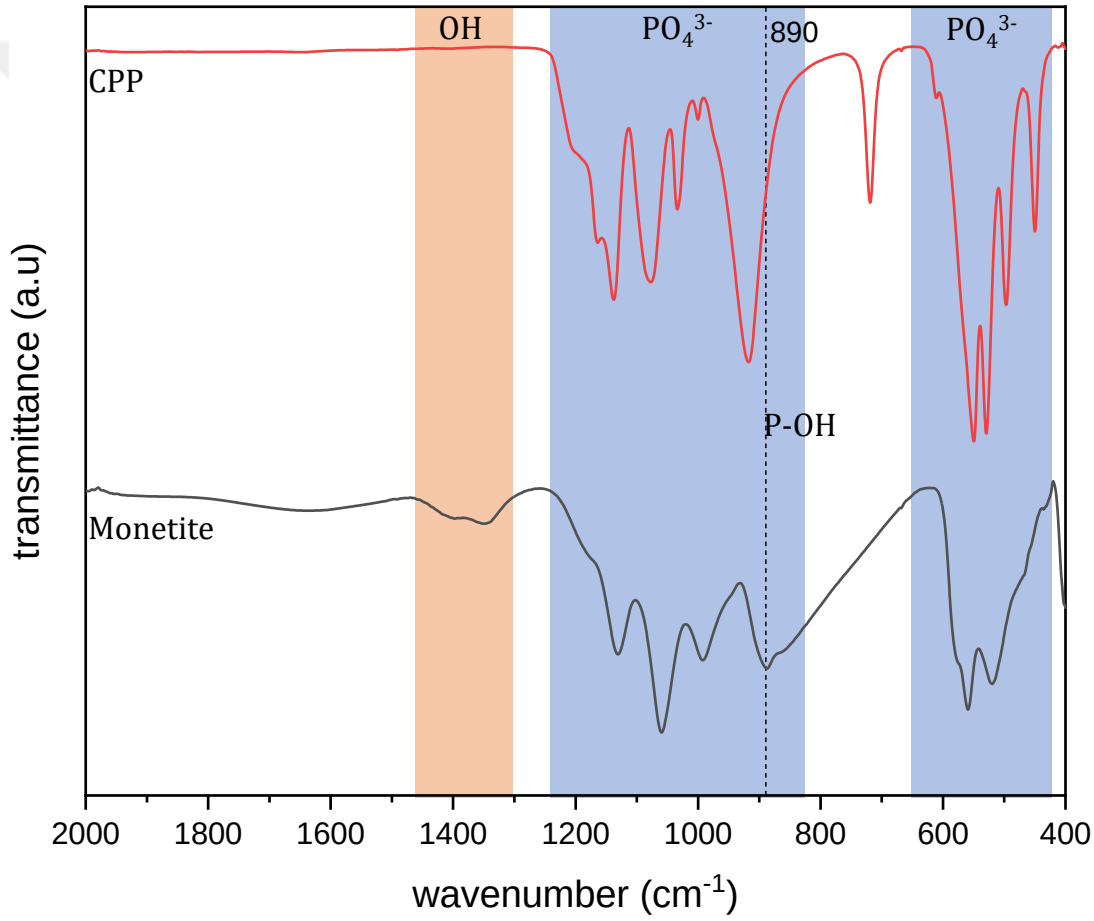


Figure 3.2: FTIR spectrum of Monetite and Calcium Pyrophostate in the range of 2000-450 cm^{-1}

3.2 Characterization of Solid-State Products

Both $CaHPO_4$ (or monetite) and CPP powders are blended with $CaCO_3$ separately and the powder mixtures were fired at 1200 °C for 2 h followed by air quenching. The XRD diffractograms of TCP1 and TCP2 are given in Figure 3.3. TCP1 includes two phases: major phase α-TCP with JCPDS card no 09-348 and HAp phase with JCPDS card no 09-432 while TCP2 XRD diffractogram is matched with only α-TCP phase. XRD data reveals that both powders are effectively air-quenched since no β-TCP formation is detected (From now on, α-TCP will be referred as TCP since no other polymorph of TCP is present in the study). However, TCP2 powder has higher purity compared to TCP1 powder according to XRD diffractograms.

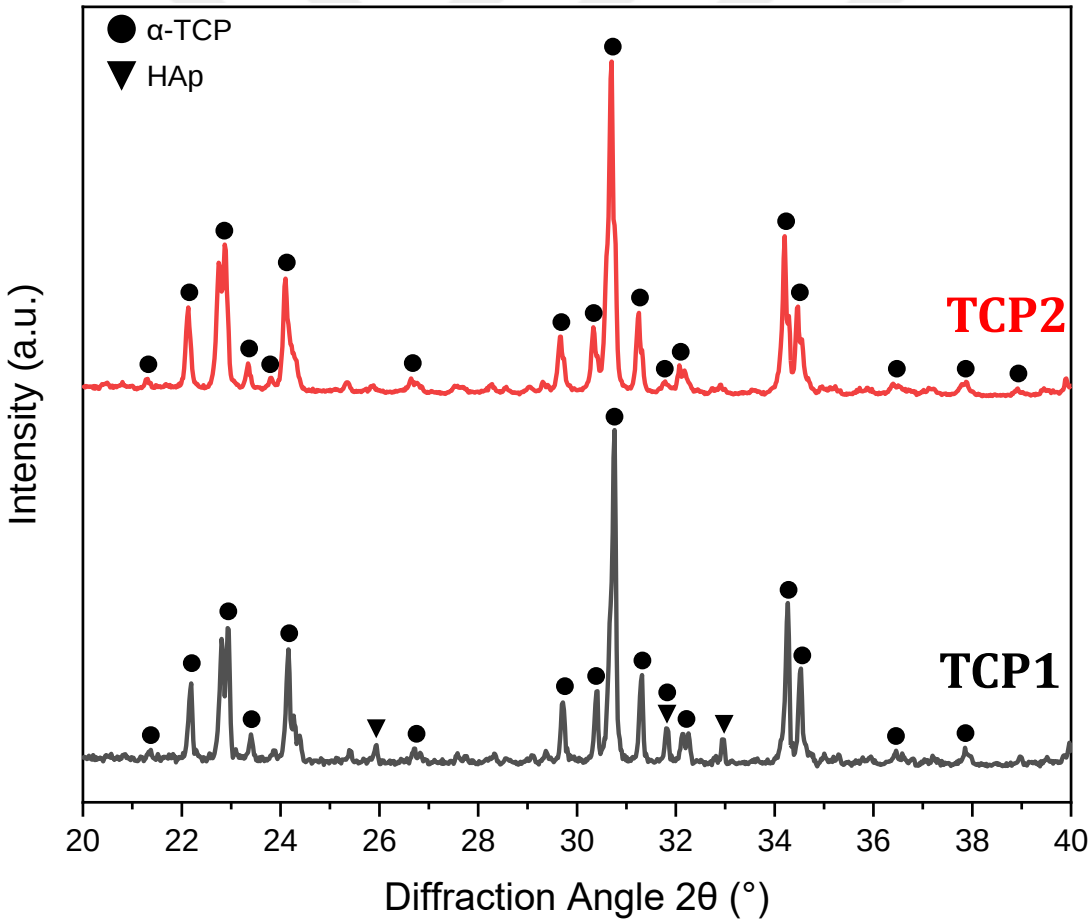
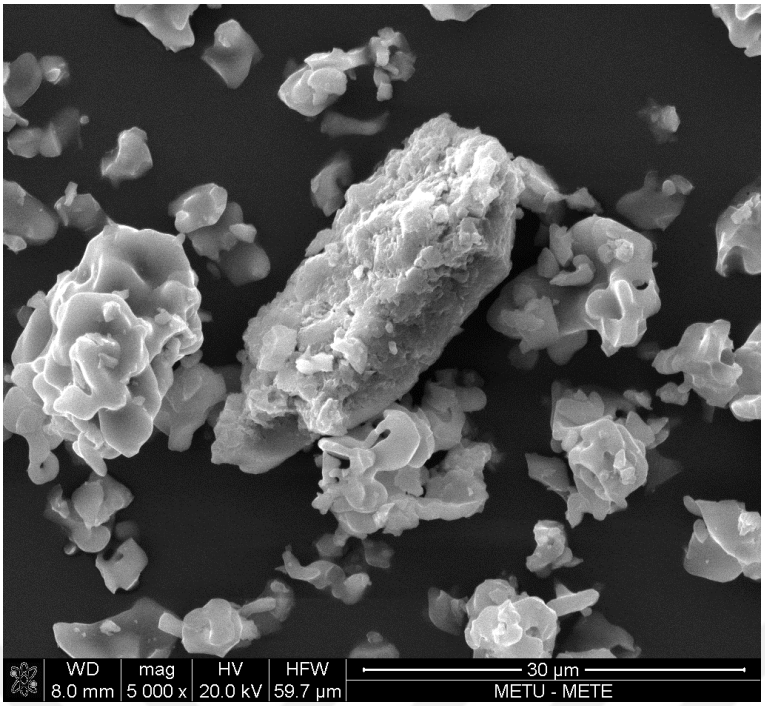


Figure 3.3: The XRD diffractograms of the solid state synthesis products by following different routes named TCP1(below) and TCP2 (above)

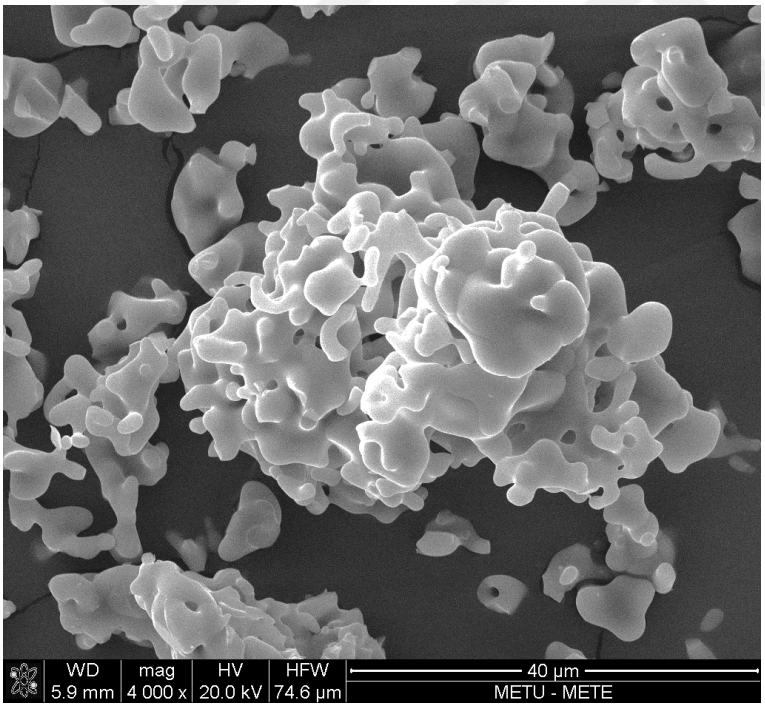
In TCP1 powder, HAp peaks are observed which is undesired for the purity reasons. The presence of water vapor may lead HAp formation if there is any deviation from Ca/P ratio of 1.5 in the powder batch prepared just before the solid-state reaction [24]. The elimination of possible water vapor sources was necessary prior to the solid-state reaction by firing monetite powders (see Equation (2.1) and Equation (2.2)). The presence of HAp peaks for TCP1 powder's XRD diffractogram shown in Figure 3.3 were considered as impurity. Thus, removal of water molecules from monetite, in other words using CPP as solid state reaction precursor, provided higher purity for the end-products. Even though both TCP1 and TCP2 powders were prepared with same Ca/P ratio of 1.5, H_2O vapor formed during sintering can not be removed from the furnace. Thus, it is critical to remove chemically bonded water molecules from the system.

The importance of obtaining pure TCP arises from setting reaction of TCP. The presence of another phase may alter the reactivity of TCP powders in overall [41]. However, HAp phase is not completely undesirable since as a result of setting reaction, CDHAp form as a product. HAp particles formed during the solid-state reaction might act as a nucleating agent in the system which accelerate the setting reaction. Acceleration of setting reaction may show adverse effect in the following studies covered in this thesis. SEM images of TCP1 and TCP2 are given in Figure 3.4. In Figure 3.4a, among TCP1 particles, a secondary particle was observed with different morphology and this secondary particle was attributed to presence of HAp (as revealed also by XRD). In Figure 3.4b, on the other hand, no other foreign particle different than typically semi-fused TCP morphology was detected and this is in an agreement with XRD result given in Figure 3.3. For the remaining part of the thesis, TCP2 particles were employed in preparation of printing cement pastes/inks.

As seen in Figure 3.4, metastable TCP is synthesized at the sintering temperature followed by rapid quench, hard aggragates or agglomerates are commonly observed. To check the ultrasonication effect on dispersing TCP2 (phase pure α-TCP) particles, following particle size distribution graphs are given in Figure 3.5. Ultrasonication eliminate the bigger particles (between 30 to 40 μm) at certain extent. In addition, volume weighted mean is decreased from 11.18 μm to 8.93 μm after ultrasonication. However, agglomarates are present even after aggresive ultrasonication treatment.

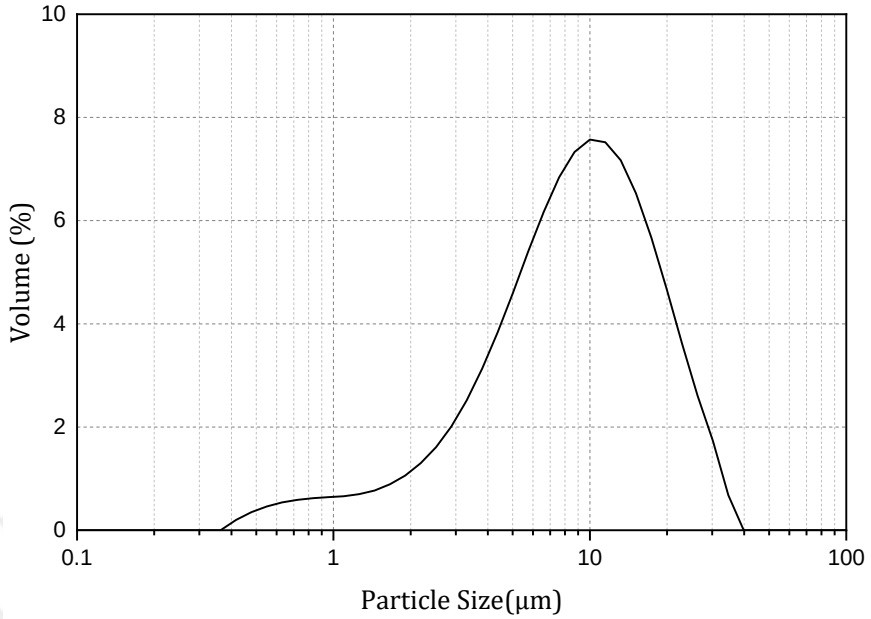


(a) End Products of Solid State Synthesis Route 1

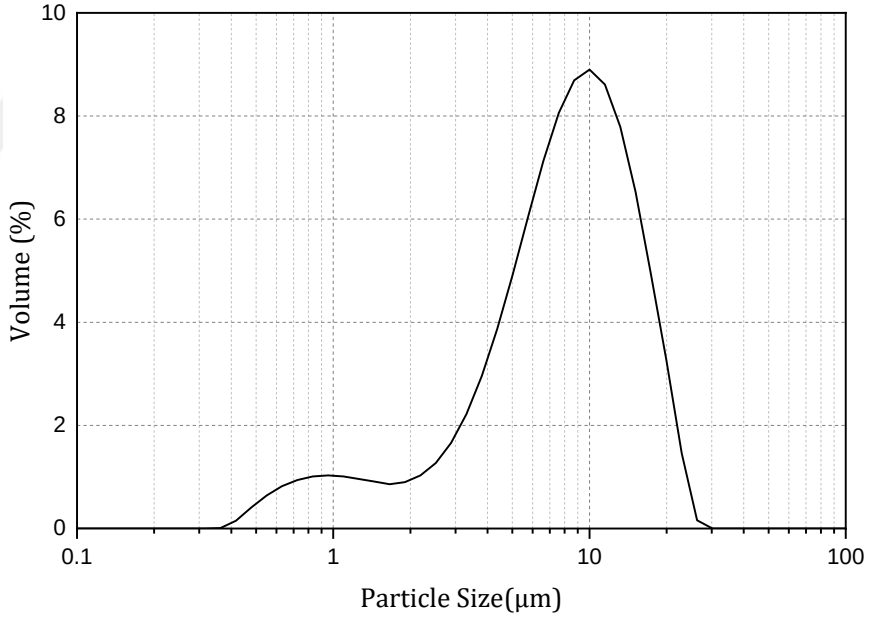


(b) End Products of Solid State Synthesis Route 2

Figure 3.4: The SEM images of end-products of the solid state reactions (a) Two different morphologies were observed which is likely to HAp surrounded by TCP particles; (b) Pure α-TCP particles varying in size.



(a) TCP2 particle size distribution without ultrasonication treatment



(b) TCP2 particle size distribution with ultrasonication treatment

Figure 3.5: The particle size distribution of TCP2 powder (a) without any treatment; (b) with ultrasonication treatment

CHAPTER 4

INJECTABILITY/MANUAL PRINTING STUDIES WITH DIFFERENT CEMENT PASTE FORMULATIONS

In this chapter, preliminary studies of the printing pastes prepared with different binder solutions and liquid-to-powder ratios (LPRs) are examined thoroughly. After the preliminary study on the injectability of CaP paste, the binder solution and LPR to be used during fabricating scaffolds were determined. For preliminary investigations, pastes were prepared and manually injected through the syringe tip to create dummy scaffolds for pure (α-TCP only) and hybrid (dual cement mixture, α-TCP:Calcium Sulfate hemihydrate) cement pastes. TCP and hybrid dummy scaffolds were hydrated in excess DI water at 37°C at various time intervals. XRD analysis was performed to detect phases and cement conversion (to hydroxyapatite or calcium sulfate dihydrate) after hydration; FTIR analyses were conducted to identify chemical bonding characteristics of the hydrated products and the morphological changes after the hydration was examined by SEM for each sample. In summary, the rationale of the main processing approach, i.,e. using cement-based printing paste for obtaining shape preserved has been validated with the help of some practical means and a variety of analytical techniques.

4.1 Effect of Binder Solution and LPR on Injectability of Calcium Phosphate Cement Paste

Binder solutions were prepared with different polymeric additives at variable concentrations were employed to increase/control the viscosity of the liquid solution and the plasticity of the paste to achieve a stable form with structural stability during and after the printing process. This is also critical to have easy handling during the injection through the needle tip, as discussed in Chapter 2. Table 4.1 summarizes the printing formulations composed of two different polymeric binders (Pluronic F127 and Alginate) at variable concentrations (wt.%) of polymeric binder in DI water combination; these can be considered as parametric factors defining the LPR values of the pastes and therefore injectability in semi-quantitative manner.

Liquid to Powder Ratio (LPR) defines the necessary amount of liquid medium to transport paste and effectively bind the particles together during the injection process. Although theoretically, an LPR value of 0.35 is sufficient for the particles to move through the syringe, particle morphology and particle-water interaction due to hydration can affect the injectability. A higher liquid amount or implementation of surfactant to the system is required to push particles via a liquid medium. According to percent injectability determined through the protocol described in Chapter 2 Materials and Methods, Section 2.2.2. As summarized by the Table 4.1, increasing

Table 4.1: % Injectability values of different printing paste formulations determined according to Equation (2.3)

	Type of Binder			
	Pluronic F127			**Alginate**
Liquid to Powder Ratio (ml/g)	20 wt. %	25 wt. %	30 wt. %	2 wt. %
0.55	41.9 ± 3.5	21.2 ± 7.7	-	81.0 ± 4.1
0.6	82.1 ± 3.6	79 ± 2.8	55.0 ± 8.0	85.9 ± 2.6
0.65	90.7 ± 1.4	90.2 ± 1.4	86.4 ± 3.4	94.4 ± 1.0

LPR from 0.55 to 0.60 and further to 0.65 enhanced the injectability of the CaP paste for all binder solutions at all concentrations, especially for the binder solutions prepared with Pluronic F127. However, 30 wt.% Pluronic F127 solutions exhibited no injectability for LPR=0.55, while the paste prepared with 2 wt.% alginate with the same LPR values showed better injectability. However, the CaP cement paste prepared with alginate solutions with LPR values of 0.6 and 0.65 collapsed right after printing, as shown in figures Figure 4.1a and Figure 4.1b, suggesting that alginate pastes require immediate or in-situ crosslinking during printing. In addition, alginate and TCP powders are hydrophilic and they have a high affinity for water absorption degrading overall injectability [86]. For those reasons, further parametric studies about the concentration of alginate solution are not conducted.

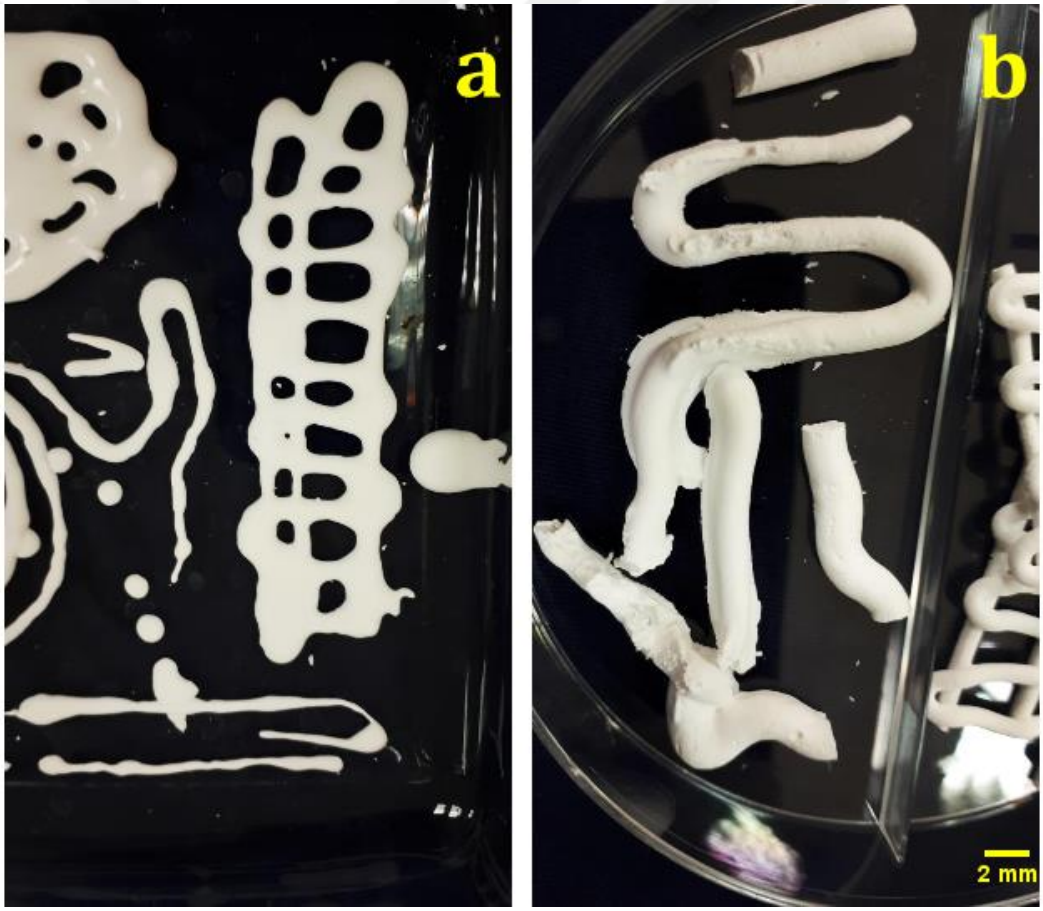


Figure 4.1: Digital camera images of dummy scaffolds, printed using cement paste prepared with 2 wt.% alginate:DI water liquid solution (a) at LPR=0.55 collapsed right after injection; (b) at LPR=0.6 showed excessive spreading after injection.

While alginate-water liquid solutions seem problematic to be utilized as printing pastes, handling properties of Pluronic F127:water liquid solutions, including TCP particles, were more manageable. Increasing the amount of polymeric plasticity provider, i.e., increasing the concentration of Pluronic F127 binder did not show (as observed by visual observations) any adverse effect on the structural integrity for most of the injected parts, even though using an LPR value of 0.65 (in the upper limit of the studied range of 0.55-0.65) for 20 wt.% Pluronic F127 cement paste showed the best injectability value (90.7±1.4) and character. However, at such a high liquid amount, the structural features of injected parts started to disintegrate/spread and the sharp features of the layers began to fuse 25 wt.% and 30 wt.% Pluronic F127 cement pastes showed good structural integrity for almost all LPRs and a representative example of hand-printed structure is shown in Figure 4.2 for 20 wt.% Pluronic F127-containing cement mixture with a low LPR value of 0.6. However, the injectability was adversely changed and altered with the increased binder concentration.

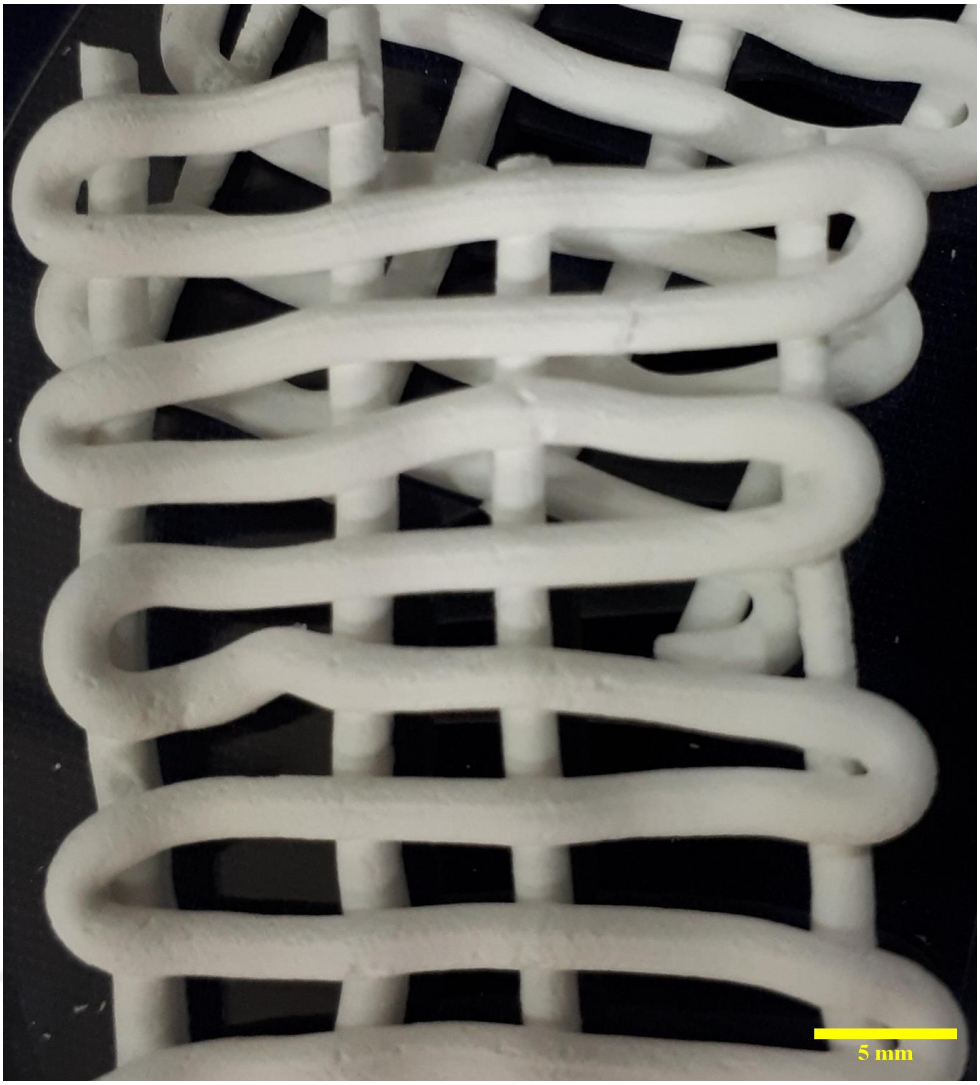


Figure 4.2: Digital camera image of a dummy scaffold prepared with 20 wt.% Pluronic F127:DI water liquid solution at LPR=0.6 with distinct structural features without fusion between the layers and well integrated form.

The best candidate cement paste recipe, with an optimal LPR and concentration, was determined/chosen as LPR of 0.6:Pluronic F127 concentration of 20 wt.% providing structural stability of the printed scaffold and the ease of injection are ultimate crucial parameters for the automated 3D printing process. It is worth mentioning that both parameters may be influenced by the viscosity of the paste, which is controlled by concentration and the printing temperature.

4.2 Characterization of Dummy Scaffolds

Multiple dummy scaffolds (strips with circular cross-sections more or less overlayed on each other) were formed by hand injection using the cement mixture with optimum formulation (with liquid solution of 20 wt.% Pluronic F127 and LPR of 0.6). Each hand-printed dummy scaffold was hydrated (in water-filled plastic vials submerged in a water bath tank) at 37 °C in excess DI water for 6, 12, 24, 48, or 72 h to induce cement hydration (α-TCP → HAp). The XRD data of the time-dependent hydration kinetic study is shown in Figure 4.3. In this figure, the pattern of the as-prepared powder (TCP, the bottom pattern) as a reference; together with as-printed TCP:Pluronic F127 dummy-scaffold and TCP:Pluronic F127 dummy scaffolds hydrated for different time intervals, are shown.

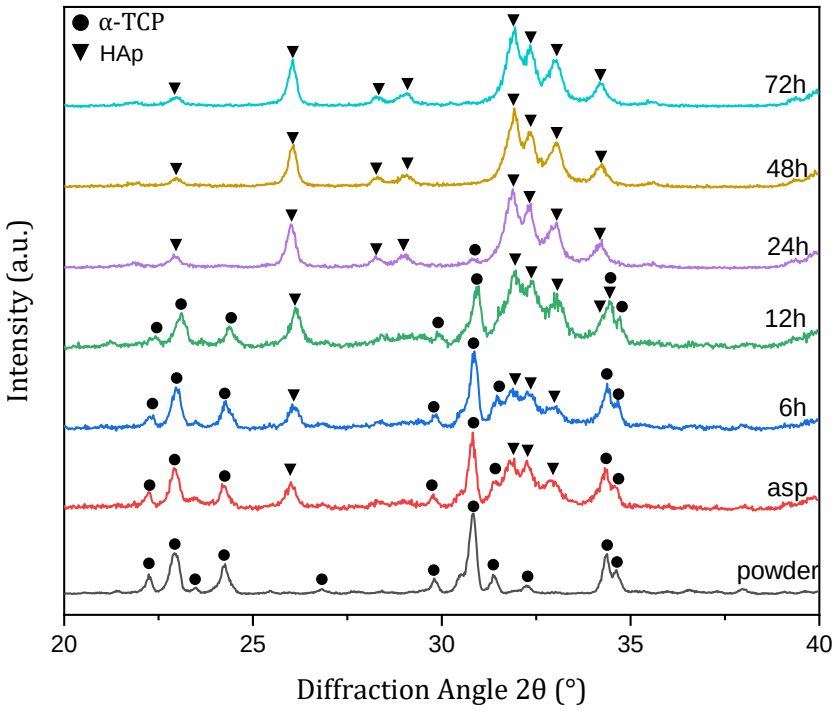


Figure 4.3: The XRD diffractograms of TCP:Pluronic F127(20 wt.%) scaffolds in as-printed condition and after hydration for 6, 12, 24, 48 ,and 72 h in excess DI water.

As shown in Figure 4.3, TCP dummy scaffolds were partially hydrated even in printed conditions indicated by the presence of HAp diffraction peaks (2ϑ range of 32-34°) together with strongest diffraction peak of TCP (2ϑ at around 31°) in the diffractogram of this sample (second pattern at the bottom). It is worth mentioning that the printing blend contains aqueous polymeric binder solution and therefore, it can partially initiate hydration of TCP. This also implies a high hydraulic reactivity for TCP, i.e., conversion efficiency to HAp. This partial hydration (cement-type setting and hardening) is beneficial/crucial for the printed structure to preserve its formed shape and hamper the disintegration, because when these dummy scaffolds are immersed in water to complete hydration, as the binder (here Pluronic F127) can readily dissolve in excess DI water. It is known that crosslinking mechanism of Pluronic F127 is related to its concentration in water and it loses gelled nature/structure below 15 wt.% Pluronic F127:H_2O [71]. The other diffractograms in Figure 4.3 correspond to longer hydration times (12, 24, 48 and 72, h) and show well-defined and higher intensities for prolonged hydration times for HAp peaks (2ϑ range of 32-34°). Meanwhile, the TCP peak's (2ϑ at around 31°) intensities gradually decrease and diminishes at some point indicating complete conversion to HAp. According to the data in Figure 4.3, complete transformation from TCP phase to HAp phase of TCP:Pluronic127 dummy scaffolds occurs sometime between 24-48 h. These results in an agreement with more precise isothermal calorimetry-based kinetic studies for pure TCP powder [41]. It can be said that Pluronic F127 did not alter the hydration activity/kinetics of TCP particles that much.

After the preliminary studies with α-TCP, similar investigation was performed with dual cement mixtures with calcium sulfate hemihydrate (CSH) which also undergoes a cement reaction ($CaSO_4 \cdot \frac{1}{2} H_2O \rightarrow CaSO_4 \cdot 2\,H_2O$ or CSH $\rightarrow$ CSD) In other words, two different cement powders were used together with Pluronic127. Mechanical properties of the ceramic bodies formed after cement reaction are directly related to phase transformations which leads morphological changes for the starting powder. Typically, after hydration/cement setting loose powders convert to a reticulated/interlocked crystal network leading to a hardening. A dual cement mixture therefore can provide improved structural and mechanical integrity, upon simultaneous conversion to end interlocked products.

In hybrid cement studies, first CSH was mixed with TCP (according to the details in Section 2.2.3 of Materials and Methods Chapter 2) at different weight ratios with an intention improve the mechanical properties of printed scaffolds, as CSH sets to harder compacted form faster compared to TCP when it is mixed water [93]. The optimized formulation was employed in hand printing the dummy hybrid scaffolds. Similar hydration kinetics/efficiency examination was also performed for dual cement precursor containing TCP:CSH (90:10 wt.% respectively, names as CSH10 set) printing mixtures. The XRD diffractograms of starting powders (α-TCP:CSH and hand-printed dummy scaffolds hydrated at 37 °C for different time intervals (6 h up to 72 h) are given in Figure 4.4. Addition of 10 wt.% CSH did not alter the initial hydration of α-TCP → HAP for dummy scaffolds in as-printed condition (second pattern at the bottom); indicated by the presence HAp peaks in the 2ϑ range of 32-34°. Also, in as-printed condition low intensity CSH peaks (second pattern at the bottom) were disappeared except the peak around 25.6°, the observation of CSD peaks for as-printed (CSD) were started to be seen 2ϑ of 11.7, 20.8 and 29.2° which validates the previous suggestion that CSH phase set faster than TCP. As it was stated above, an initial maturing hydration is desirable for any paste formulation. However, CSD peaks disappeared between 12-24 h, which can be due to dissolution of CSD particles.

According to Figure 4.4 there is a peculiar calcium sulfate phase besides possible reactant (α-TCP, CSH) or/and product phases (HAp, CSD). This is pointed out by the diffraction peak around 2ϑ of 25.6° for a calcium sulfate anhydrous (or mineral known as anhydrite or CSA). The presence of high concentration of common ions (Ca^{2+} etc.) in the cement hydration solution may alter the hydration mechanism (as can be also seen for body fluids, miscellaneous ionic solutions etc.) may cause ease dissolution CSD particles and therefore formation of different calcium sulfate phase(s) on HAp particles. [94, 95]. Also, another possible reason for CSA formation might be related to the presence of Pluronic F127, since it is reported that polymeric additives change the relative stability of CaS phases in the structure [96]. As the hydration proceeds to longer times, the intensity of the CSD peaks decreased and CSD peaks disappear after 6 h. Additionally, TCP particles were not fully converted to the HAp in the presence of second cement phase (CSA) phase since a TCP peak around 2ϑ of 30.8° were still observable for 72 h (comparing to time-equivalent pattern for only TCP cement in

Figure 4.3) hydrated dummy scaffolds. Thus, CSH addition altered and marginally hampered the complete hydration of TCP particles.

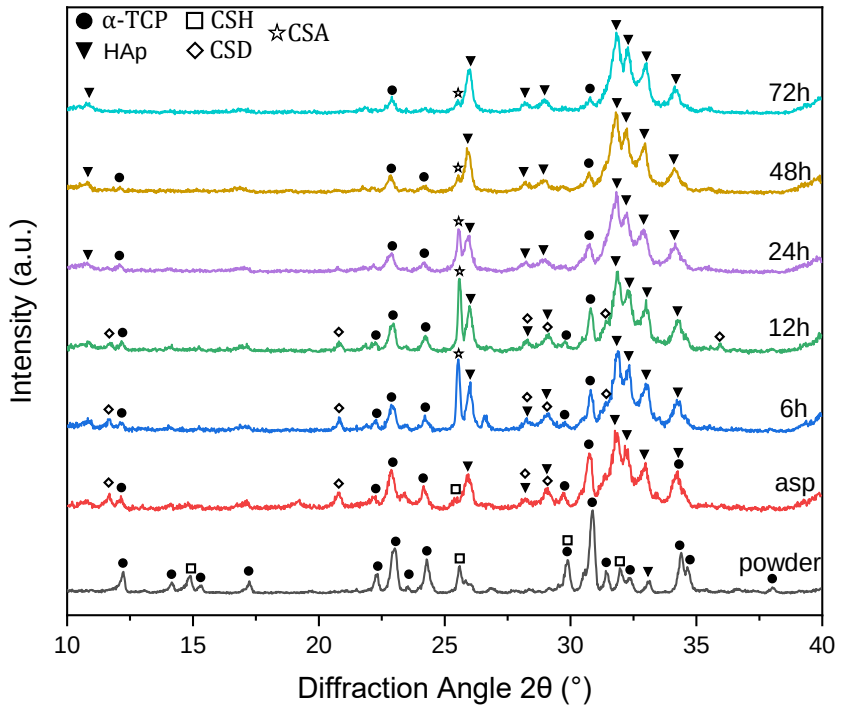


Figure 4.4: The XRD diffractograms of CSH10:Pluronic F127(20 wt.%) scaffolds in as-printed condition and after hydration for 6, 12, 24, 48 ,and 72 h in excess DI water.

For a chemical composition analysis, interpretation is made by EDS results to have an idea about degradation/dissolution of calcium sulfate phases in dual-cement pastes. Thus, the chemical composition of CSH10 set, as determined by EDS results as function of hydration time are given in Table 4.2. As seen from the table, sulfur content of 5±1.8 at.% (indicative for presence of CSH or CSD) in the system decreased as the hydration time increased and the lowest sulfur content (2.4±0.3at.%) was observed for 72 h hydrated dummy scaffolds. The XRD results also suggested the dissolution of calcium sulfate phases was observed as the hydration time increases in excess DI water. Therefore, chemical composition analyses with EDS somewhat correlate with the XRD based finding of Figure 4.4.

Another set was prepared with TCP:CSH (75:25 wt.%, respectively, named as CSH25) again composed of dual cement printing pastes. XRD diffractograms of starting α-

Table 4.2: Chemical composition (by EDS) CSH10 scaffolds. (Data was collected at 300x for 3 different zones and average composition is given in at. %)

	powder	**asp**	**6h**	**12h**	**24h**	**48h**	**72h**
Ca (at. %)	61.1 ± 0.6	62.6 ± 2.9	63.2 ± 1.3	62.1 ± 3.5	60.7 ± 0.4	61.3 ± 1.4	61.5 ± 0.4
S (at. %)	5 ± 1.8	6.0 ± 0.3	4.9 ± 0.5	4.5 ± 0.5	4.1 ± 0.4	3.0 ± 0.2	2.4 ± 0.3
P (at. %)	33.9 ± 1.3	31.4 ± 2.5	31.9 ± 0.8	35.4 ± 0.6	35.2 ± 0.8	35.7 ± 1.2	36.1 ± 0.5

TCP:CSH powder mixture and as-printed and all hydrated CSH25 dummy scaffolds is given in Figure 4.5. HAp peaks can be again seen in as printed condition. Presence of CSH at higher amount is more distinctively indicated by the XRD data. Although CSD peaks (cement product phase) were seen for CSH10 dummy scaffolds in as-prepared condition, CSD peaks for CSH25 dummy scaffolds started to be observed after 6 h they were hydrated in water. It looks like hydration of CSH slows down, because CSD was observable even as-printed condition for 10 wt.% CSH mixture. For the CaP phases; even after 72 h, there are still TCP peaks are present and it is seen at top pattern of Figure 4.3. TCP conversion to HAp was not completed and the residual TCP amount was the higher. Meanwhile, CSH hydration product phases; CSD and CSA still remain after 72 h. It was concluded that adding more CSH altered TCP's hydration mechanism/kinetics more evidently. Same is also valid vice versa, i.e. TCP changes CSH's hydration and also it is phase stability behavior, it more effectively convert by products of CSD and CSA.

The chemical composition based on EDS results for this set are given in Table 4.3 and it can be seen that sulfur content in the CSH25 dummy scaffold shows different trend to that for CSH10 dummy scaffolds. Sulfur content remains almost constant (with a slight decrease) in the range of 11.8±0.5-8.1±0.6 at.% during hydration . Meanwhile, the XRD peak intensities of calcium sulfate phases (CSD and CSA) are remarkable and increase with hydration. Therefore, XRD and EDS results are somewhat contradictory. This might due to amount of initial CSH, which higher for 25 wt.% CSH containing system and dissolution of CaS phases does not proceed even after 72 h.

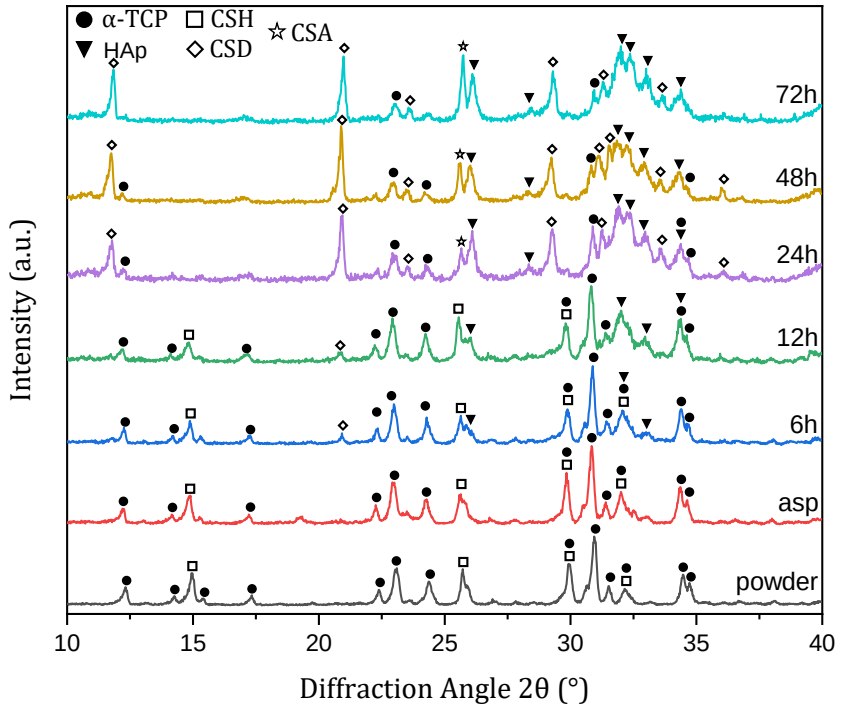


Figure 4.5: The XRD diffractograms of CSH25:Pluronic F127(20 wt.%) scaffolds in as-printed condition and after hydration for 6, 12, 24, 48 ,and 72 h in excess DI water.

The summary of XRD data, pointing out phase changes for all sets (TCP, CSH10, CSH25) are given in Table 4.4 to provide a help. The changes for each cement reactant(s) and time lapses for phase formations/losses during 72 h of hydration are tabulated. The time spans were determined from the observation of the most intense peak of corresponding phase. The conclusion from this table are: TCP phase converts fully to HAp after 72 h. ii. Initial CSH converts to two new phases of CSD and CSA,

Table 4.3: Chemical composition (by EDS) CSH25 scaffolds. (Data was collected at 300x for 3 different zones and average composition is given in at. %)

	powder	**asp**	**6h**	**12h**	**24h**	**48h**	**72h**
Ca (at. %)	59.7 ± 0.4	60.4 ± 0.2	60.0 ± 0.2	59.7 ± 0.9	60.0 ± 0.4	60.3 ± 0.6	60.5 ± 0.7
S (at. %)	11.8 ± 0.5	11.4 ± 0.6	11.5 ± 0.1	10.9 ± 0.7	10.2 ± 0.1	9.3 ± 0.3	8.1 ± 0.6
P (at. %)	28.5 ± 0.6	28.2 ± 0.6	28.5 ± 0.2	29.4 ± 0.4	29. 8 ± 0.4	30.4 ± 0.6	31.4 ± 0.3

which dissolves in the case of 10 wt.% CSH, but remain for 25 wt.% CSH-containing hybrid cement.

Table 4.4: Summary of XRD results of TCP,CSH10 and CSH25 samples are sorted by phases present XRD data and include information about when did the peaks start to be observed or disappeared in time.

Cement Formulations	**Phases**	**Most Intense Peak (2theta)**	**First time seen**	**Last time seen**	**Change after 72 h**
TCP	TCP	30.8	as-prepared	24 h	dissolved
	CDHA	32	as-printed	72h	remained
CSH10	TCP	30.8	powder	72h	remained
	CDHA	32	as-printed	72h	remained
	CSH	14.7	as-prepared	as-printed	dissolved
	CSD	20.8	as-printed	12h	dissolved
	CSA	25.6	6h	72h	remained
CSH25	TCP	30.8	as-prepared	72h	remained
	CDHA	32	as-printed	72h	remained
	CSH	14.7	powder	12h	dissolved
	CSD	20.8	6h	72h	remained
	CSA	25.6	24h	72h	remained

FTIR spectra of pure TCP and hydration product of TCP (HAp) and also pure calcium sulfate hemihydrate (CSH) and hydration product of CSH (CSD) are given in Figure 4.6 to show the changes after hydration and to help in understanding following FTIR analyses of dummy scaffolds with multiple chemical constituents. In other words, these are reference spectra. As it can be seen from the Figure 4.6, main P-O bands for CaP phases overlap with S-O bands for CaS phases. Therefore, distinguishing between TCP-CSH powders is quite difficult. However, the change in the O-H bonding of calcium sulfates can be evidence whether calcium sulfates are hydrated or not and H-PO_4 group band can be indicative for the chemical nature of HAp formed upon hydration of TCP. This band reveal the formation of stoichiometric ($Ca_{10}(PO_4)_6(OH)_2$) or calcium deficient HAp (CDHAp or $Ca_9(HPO_4)(PO_4)_5(OH)$) [97].

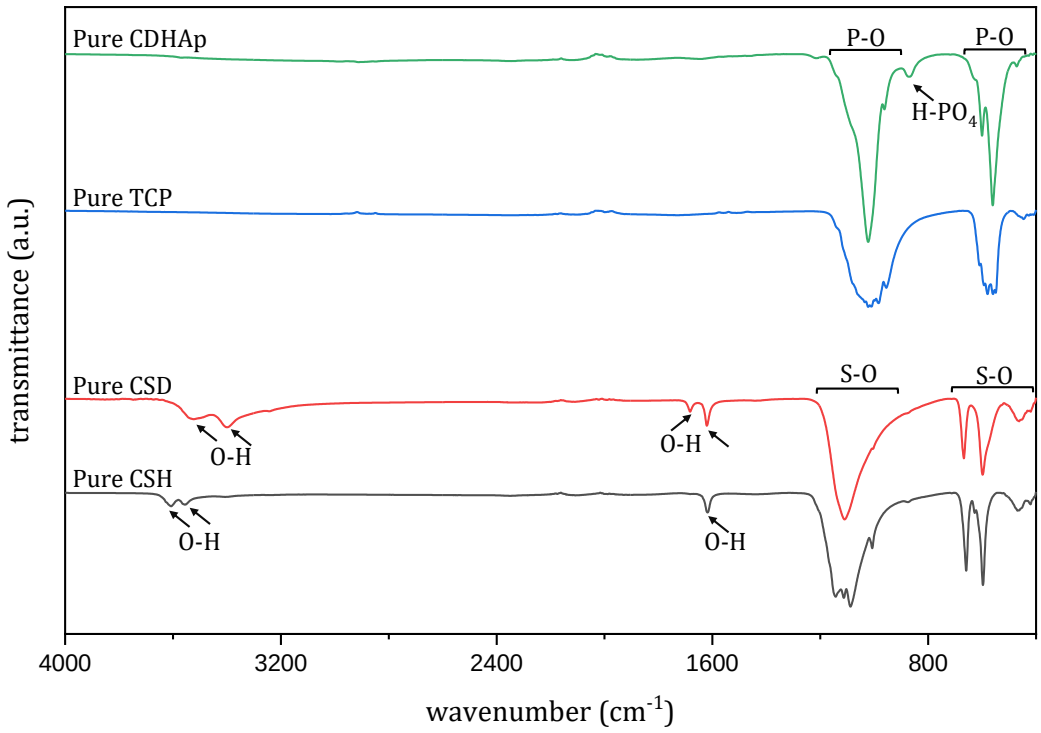


Figure 4.6: FTIR spectra of pure TCP, CDHAp, CSH and CSD given in mid-IR range. Specific bonds designated to specific phase(s) shown with arrows and P-O/S-O bonds are shown with ranges.

Further chemical analyses with FTIR were performed to elucidate the chemical nature/changes for the organic component of the cement pastes, Pluronic F127, with hydration. Figure 4.7 shows the spectra for TCP, CSH10 and CSH25 dummy scaffolds, in as-printed condition and after 6 h together with the reference spectra of Pluronic F127. As-printed and 6h-hydrated samples spectra, independent than the cement type, look all similar in terms of absorption bands and their position. There is no physical/chemical water bonds as indicated by the absorption band free region in 3600-3800 cm^{-1}. Presence of Pluronic F127 for as-printed samples is revealed by the weak absorption bands for C-O-H bands in the range of 1200 and 1500 cm^{-1}, as well by the absorption band around 2900 cm^{-1}. Since the hydration of dummy scaffolds was accomplished thorough by immersing them in excess DI water, water soluble Pluronic F127 was expected to be dissolve in the system by leaving only ceramic particles within the structure. At the end of 6 h, fingerprint absorption bands for Pluronic F127 (low intensity bands 1200-1500 cm^{-1} (C-O-H bonds) and at 2900

cm^{-1} (C-H bonds)) simply disappeared. Such chemical degradation and a related microstructural change might be beneficial since the removal of polymeric binder can be accomplished without firing operation, which may be destructive for structural integrity of a 3D-printed structure. This removal procedure can be considered a green and soft chemical operation for the fabrication of scaffolds with controlled porosity. The removal of polymeric binder is advantageous for the final functional property of a 3D-printed structure as a bioceramic, which can exhibit better osteoconductivity/bioactivity (initial bone tissue formation) and inflammation risk may also possibly decrease with the elimination of organic binder content [7,11]. In summary, FTIR analyses showed that binder remains as it is during printing and dissolves degrades after 6 h hydration.

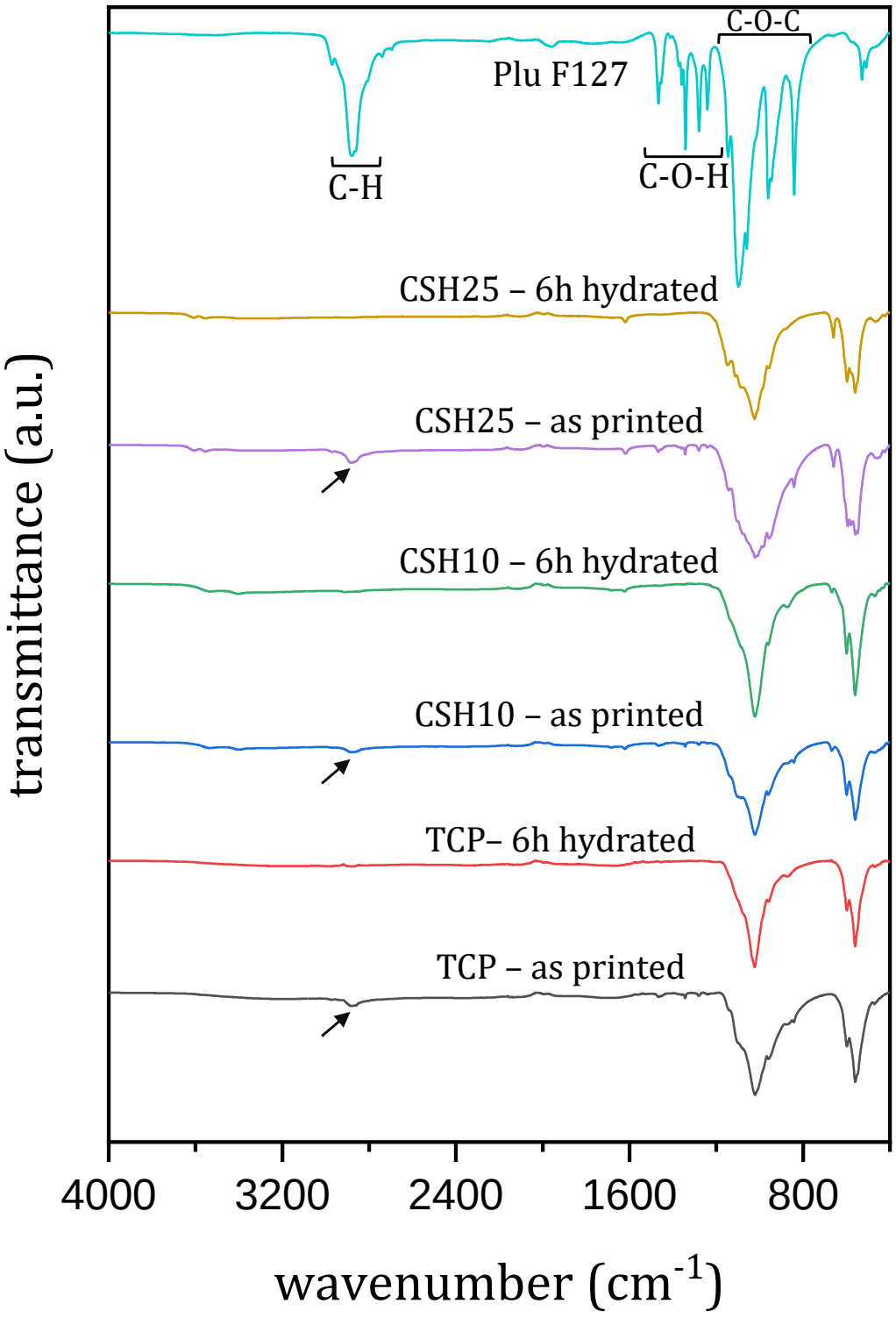


Figure 4.7: FTIR spectra of TCP, CSH10 and CSH25 scaffolds, designating binder (Pluronic F127) time. Arrow indicates the finger-print absorption band (C-H bond) for Pluronic F127.

FTIR examinations have been also employed in understanding the chemical changes for the inorganic, cement, components of the hybrid printing paste. Figure 4.8a shows the hydration time dependent FTIR spectra of CSH10 dummy scaffolds. The inset on the right site for the spectral range of 1700-1550 cm^{-1} shows the details and differences among different samples. O-H bending vibration of physically bounded water can be seen around 1683 and 1620 cm^{-1} as double band for CSD (hydrated state of calcium sulfate); and as a single band at 1620 cm^{-1} for CSH (non-hydrated state of calcium sulfate) [98] . Therefore, presence and types of O-H bending mode absorption(s) can be used to detect the chemical change/state of calcium sulfate phases. The spectra of 6 h,12 h and 24 h-hydrated samples include split absorption events with double O-H bands. Meanwhile, the absorption intensities of these bands decrease at prolonged hydration times and nullify after 48 h. This suggest that starting calcium sulfate phase CSH initially hydrates to CSD before 6 h, but this hydration product dissolves and disappear sometime after 24 h. These results are somewhat parallel with XRD results.

Figure 4.8b shows hydration time dependent FTIR spectra for higher amount CSH-containing CSH25 scaffolds. As again shown by the inset; double band of O-H bending vibration mode indicative for hydrated state, i.e. CSD, can be observed for the samples hydrated for 24 h and longer. The 6 h and 12 h hydrated dummy scaffolds exhibit single band of O-H bending (centering at 1620 cm^{-1}) indicating presence of CSH. This time hydration of calcium sulfate phase starts with a delay compared to the CSH10 cement paste. This result indicates that increasing amount of CSH in the cement paste somehow alter the hydration reactivity for calcium sulfate component of the cement.

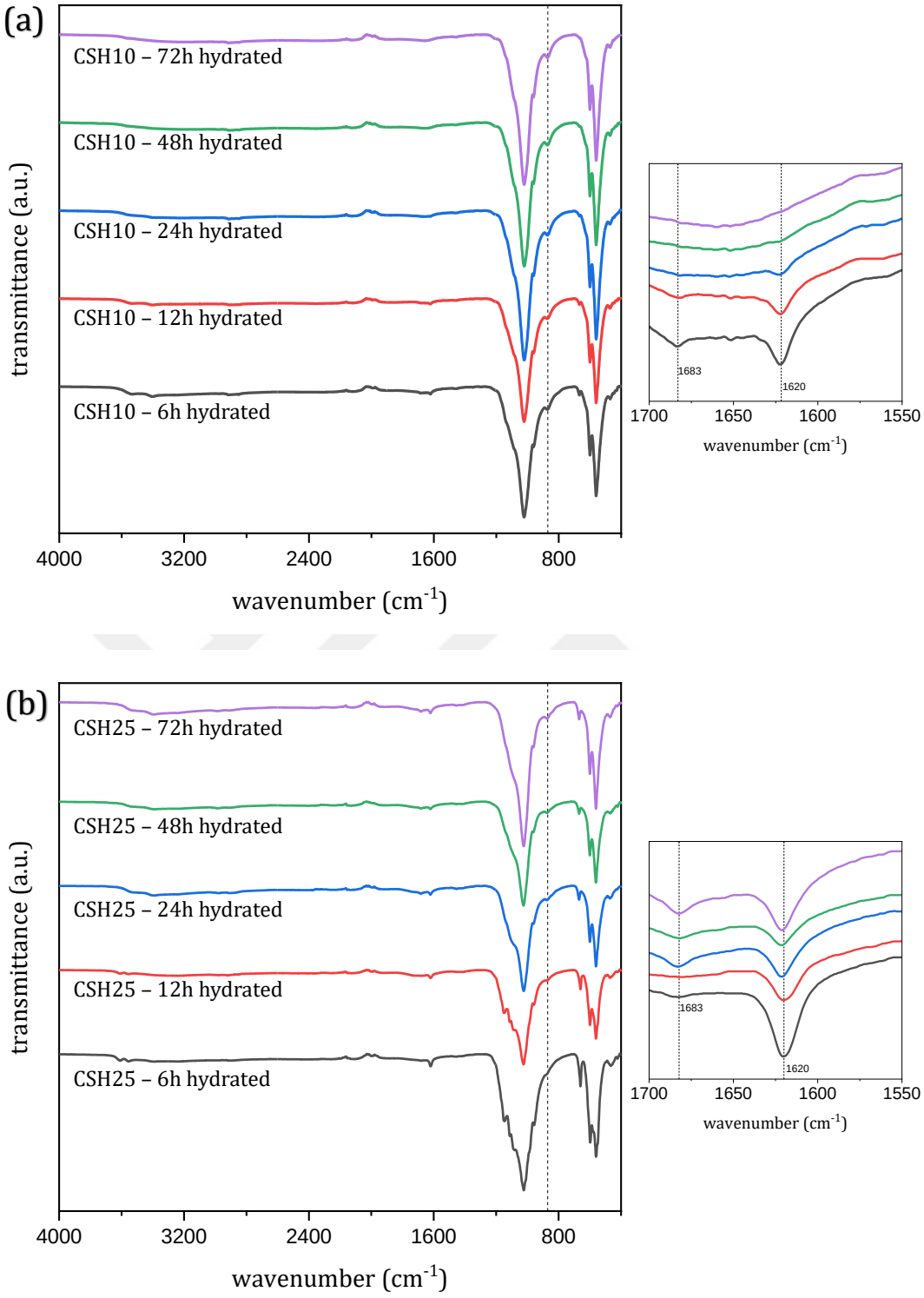


Figure 4.8: FTIR spectra of CSH10 (top) and CSH25 (bottom) scaffolds are given with inset of finger print region for OH band (1700-1550). FTIR spectra of each scaffold formulations are given for different hydration time intervals.

For microstructural investigation of hydration products, SEM analyses were performed and SEM images of unreacted TCP and hydration product of TCP (CDHAp) and unreacted CSH and hydration product of CSH (CSD) are given in Figure 4.9. Hydrated samples were obtained with hydration in DI water, in the absence of binder, of reactant powders. The objective was simply demonstrating microstructural characteristic of hydration-driven cement conversion. These images can be a microstructural reference for hybrid scaffolds. The morphologies of the CaS and CaP phases are quite different, however interlocking mechanism of both hydrated products gives sufficient mechanical strength after cement setting. CSD crystals have plate-like morphology

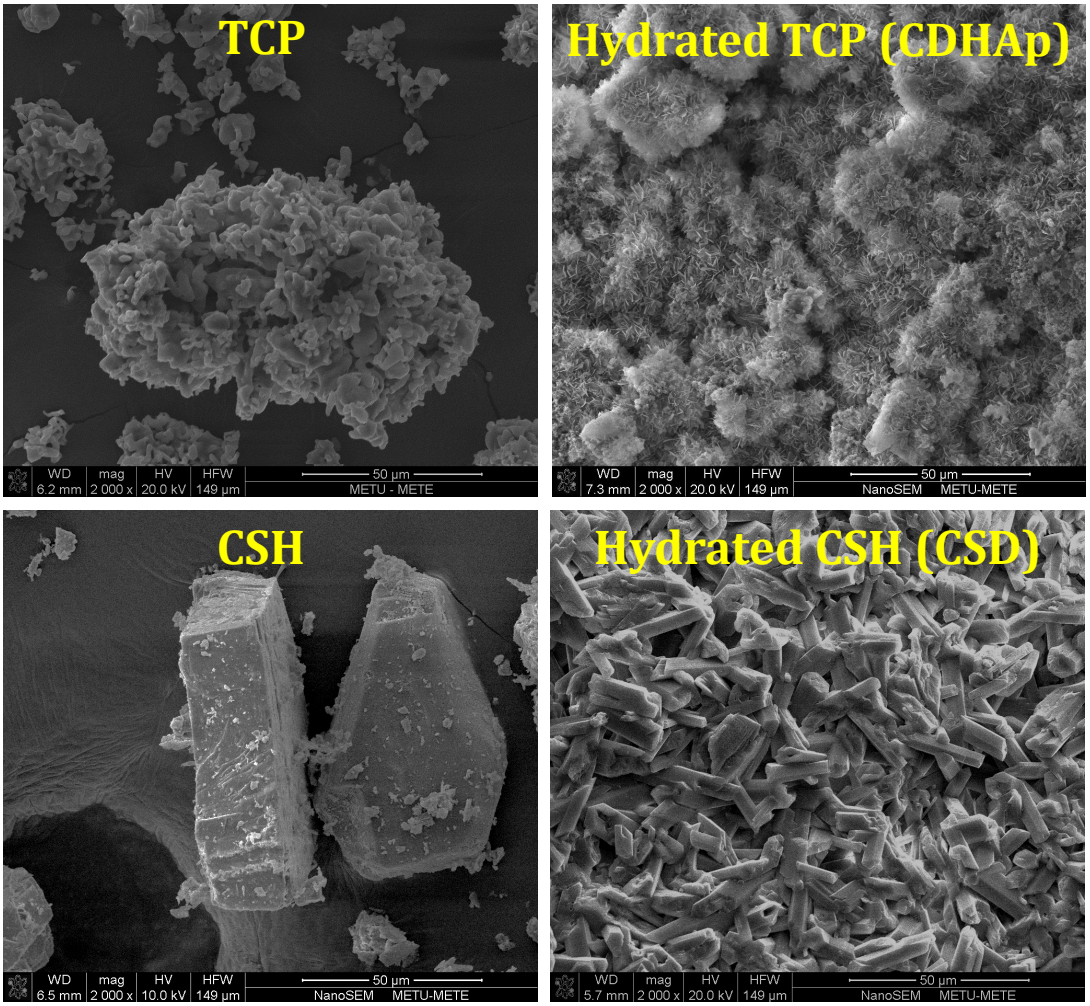


Figure 4.9: SEM micrographs of TCP, CDHAp, CSH and CSD revealing typical microstructural/morphological changes upon hydration, i.e. cement conversion. All samples were hydrated at 37°C in excess DI water.

and are quite large and exhibit bulkier crystal, CDHAp crystals are smaller and have more reticulated plate-like structure. Additionally, CSD particles shows continuous interlocked network while spacing between CDHAp particles may lower the mechanical integrity of the network.

SEM images of as printed and 6-72 h hydrated TCP dummy scaffolds are shown Figure 4.10. It is seen that small flaky features partially covering reactant particles (here TCP) can be seen for as-printed condition. As the hydration time for the samples increases, flaky crystal thickens and grows in 2D dimension become plate-like. The sharp flaky features indicative for precipitation of CDHAp for as-printed sample proliferate gradually with time for 6 h and 12 h hydrated samples. Plate-like HAp crystals can be seen for the 24 h hydrated sample and as the hydration time increases, plate-like features grow in size and observed more evidently for the whole matrix which reach largest size for 72 h hydrated sample. This microstructural investigation show a time-dependent conversion to CDHAp (as also shown by XRD and FTIR) and expected cement type morphological conversion for TCP, which may physically mature a printed structure.

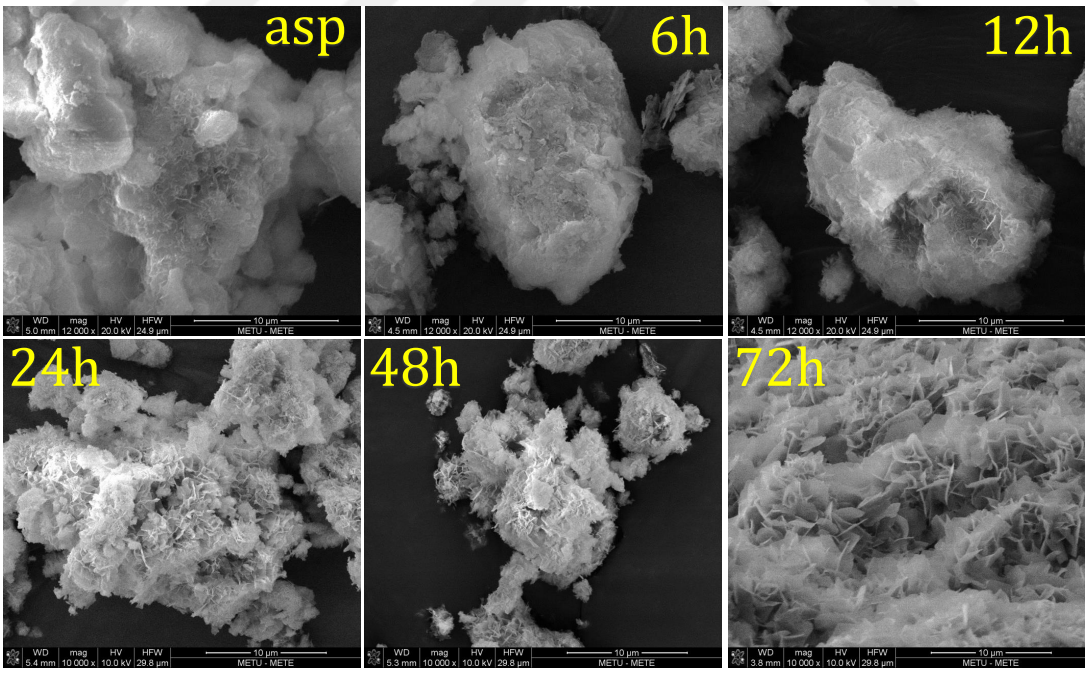


Figure 4.10: Microstructural changes of TCP-based scaffolds during hydration as a function of hydration time. (All samples were hydrated at 37°C).

Similary, SEM images of as-printed and 6-72 h hydrated CSH10 samples are given in Figure 4.11 to distinguish morphological differences of pure TCP cement and dual TCP-CSH cement. Figure 4.11 shows that hydrated calcium sulfate particles were precipitated rod-like morphology while TCP particles were hydrated and precipitated as plate-like morphology. CSD particles are started to be observed (indicated by arrows and circles) readily as-printed samples and more in number and size for 6-12 h hydrated samples. Even though CSD particles are present in the structure, they did not reach the size of CSD particles shown in Figure 4.9. CSD particles became harder to detect in the SEM images for 24 h or further hydrated samples. As it was stated above previously, dissolution of calcium sulfate particles within structure is probable by looking at XRD and EDS findings. Plate-like features of HAp phase of 72 h hydrated sample was not large as much bare TCP cement samples (time-equivalent sample) which may be contributed to the sluggish cement conversion kinetic of dual cement systems.

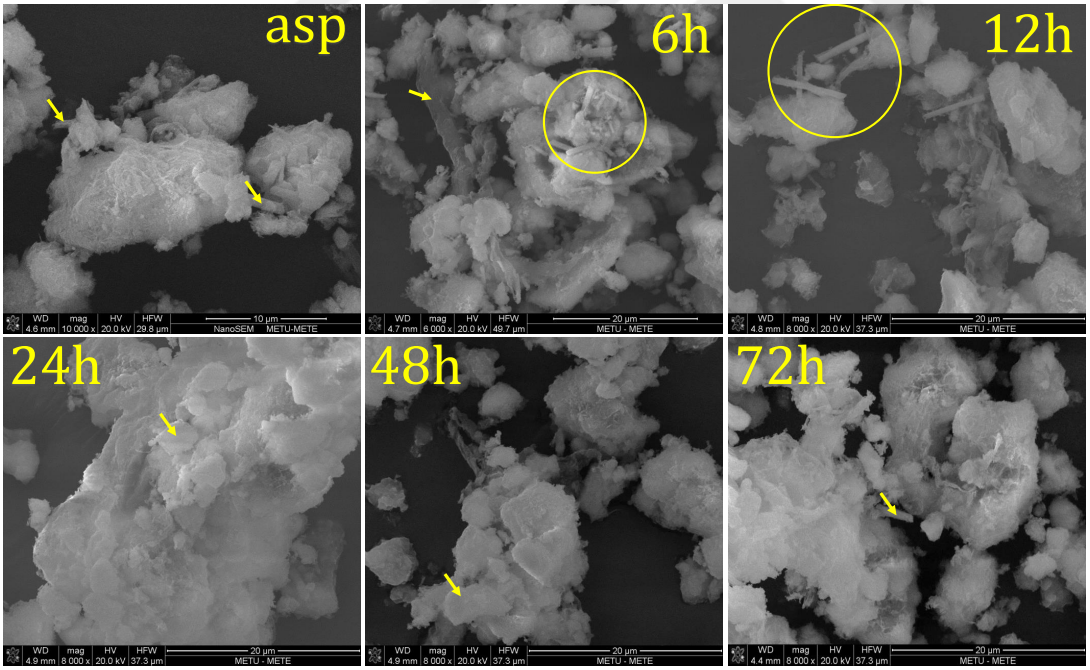


Figure 4.11: Microstructural changes for CSH10 scaffolds during the hydration of as a function of hydration time. (All samples were hydrated at 37°C).

SEM investigation was performed for CSH25 dummy scaffolds and SEM images of as-printed and 6-72 h hydrated are presented in Figure 4.12. For as-printed condition, TCP particles were clearly chosen from the image unlike the other cement formulations which confirms XRD results that TCP to HAp conversion is very low. It is observed that the samples that were immersed in DI water for 6 and 12 h have HAp precipitates and circles show unreacted CSH particles were present in the structure. However, particles with cornered and sharp features were started to be seen and shown with an arrow in 24 h hydrated sample and EDS data of that feature demonstrated that it contains high amount of sulfate within the structure. As the hydration time increased for the CSH25 samples, the particles (shown by arrows in 48 and 72 h hydrated samples) were to be grown in size in a directional manner. This kind of directional growth might be related to the excess amount of water which is used for hydration, the hydration temperature and the concentration of common ions like Ca^{2+} which may change reactive scheme of dissolution-reprecipitation of calcium sulphate particles [18]. Also, consideration for the mechanical properties of dual cement pastes, the presence of this type of bulky structures may disrupt the overall interlocking mechanism of the hydrated CaP particles and may result in decrease in mechanical strength of the material [93].

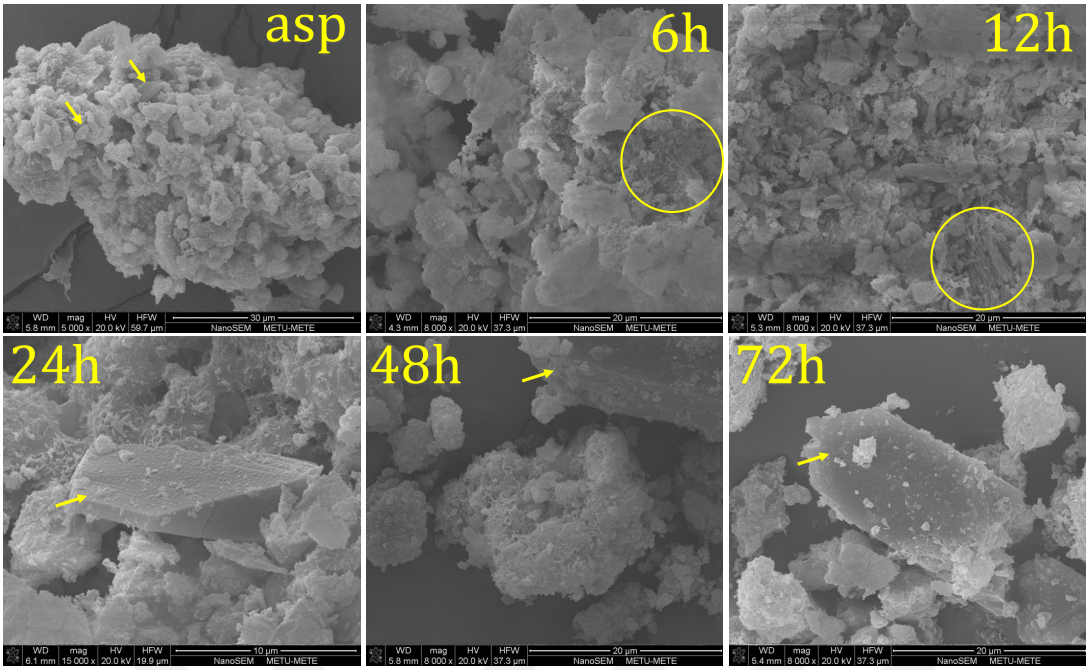


Figure 4.12: Microstructural changes for CSH25 scaffolds during the hydration of as a function of hydration time. (All samples were hydrated at 37°C)

The results and conclusive findings on dummy scaffold characterization can be seen as a proof of concept validation for the main processing rationale of the thesis. These analytical conclusions were implemented to automated 3D-printing studies in the next chapter. The determination of formulation for CaP or CaP-CaS dual phase hybrid printing cement paste emerges as practically the most important finding of this part. Meanwhile, a vast of material characterization results for the studied systems has been gathered, which can be adapted to processing on automated printer without or minimal tedious parametric studies.

CHAPTER 5

DIRECT-INK WRITING STUDIES WITH CEMENTS INKS

In this chapter, microstructural, physical and mechanical characterizations of 3D scaffolds printed using an automated system have been presented. First, 3D printing of scaffolds (constructs) by using Direct-Ink Writing approach (using Bioscaffolder) was achieved by utilizing, but also modifying previously optimized manual printing parameters and experience. These fine tuning studies aimed obtaining custom and reproducible printing parameters for the printer. The printed structures (layer by layer mesh form) obtained for this purpose were examined by visual means; and relevant data are presented by optical camera images. The printing conditions were finalized with these parametric studies (by some trial and error approach) and a standard protocol for printing pristine structures was experimentally determined. Proper TCP, CSH10 and CSH25 hybrid cement inks prepared and multiple (10 or so) identical defect-free scaffolds were printed according to fine tuning studies explained in the following section. The perfectly constructed scaffolds were hydrated for 72 h and characterized by Archimedes density measurement for rough estimation of their porosity values. Meanwhile, micro-CT images were constructed after the CT scan to investigate open and close porosities within the structures. In addition, SEM investigations were performed to reveal the morphological features after the hydration. The compression test had been conducted for evaluating the mechanical properties of selected 3D printed scaffolds.

5.1 Optimization Automated Printing Parameters

This part focuses on printing trials performed by changing the printing ink formulations for TCP based inks and also altering other parameters such as printing speed, printing pressure, temperature.

The starting ink formulations originate from manual cement paste printing studies, which need to be adapted to Direct-Ink Writing (DIW) 3D printing process. Ink printing is simply controlled injection of the cement paste through a needle attached to the syringe nozzle, that way hand simulates hand printing with more precise control. The first ink printing test was performed using the optimal formulation derived in hand printing studies, i.e. LPR of 0.6;Pluronic F127 concentration of 20 wt.%.

The optical camera images in Figure 5.1-5.6 show the gradual shape formation/preservation improvements for mesh-formed printed scaffolds as a function of several printing parameters. The first images in Figure 5.1 are representative for an ink with binder solution 20 wt.% Pluronic F127 in DI water, LPR:0.6. The syringe tip opening size was 0.6 mm and syringe temperature was 22 °C as it previously optimized. Printing speed and air pressure were 3 mm/s and 2.5 bar respectively. As it is seen from the

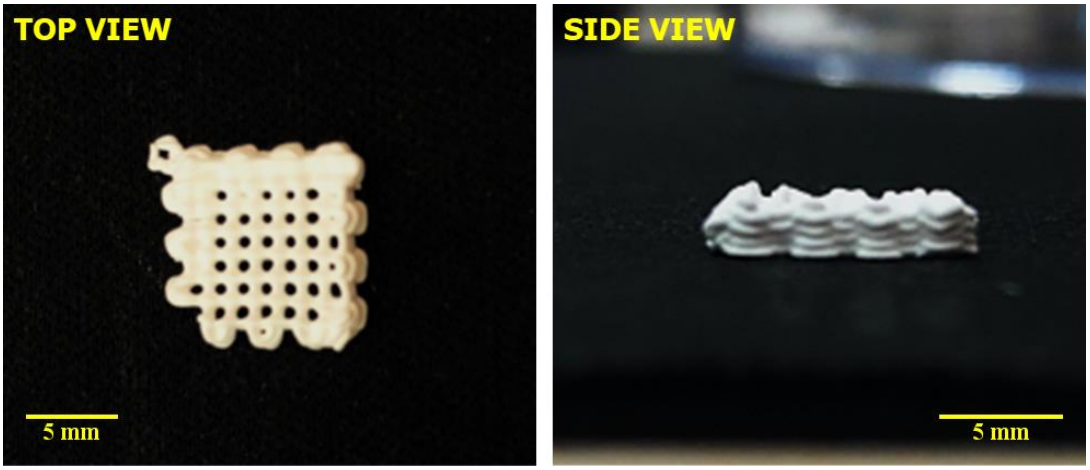


Figure 5.1: Initial printing trial of previously optimized cement-ink with the following parameters: LPR:0.6 ml/g, Concentration of binder: 20 wt.% Pluronic F127.

Figure 5.1, even though layer by layer formation of the scaffolds was accomplished (top view, left hand side figure), the strands in the final structure were partially fused to each other (side view, right hand side figure). For this case, either liquid amount in the cement paste was high or the viscosity of the solution was too low.

The construct printed changing the LPR from 0.6 to 0.55, is shown in Figure 5.2 which reflects the effect of increasing viscosity attained by lowering LPR (a more solid-containing ink). Increasing the viscosity of the paste by reducing LPR showed better layer formation in more discrete appearance. Also the collapse of the structure in height (in z-direction) seems to be eliminated. However, to be able to print the scaffold, at standard printing speed of 3 mm/s the air pressure had to be raised from 2.5 bar to 4.5 bar, which is the upper limit for device and some discontinuities were observed in the construct. Reaching upper limit for the air pressure is problematic for further printing operation, in other words injectability becomes poor. Meanwhile a longer printing operation leads to partial hydration of the TCP particles to HAp increases the viscosity of the ink and consequently higher pushing power or pressure is required and printing of thicker 3D scaffolds with 10-12 layers becomes difficult.

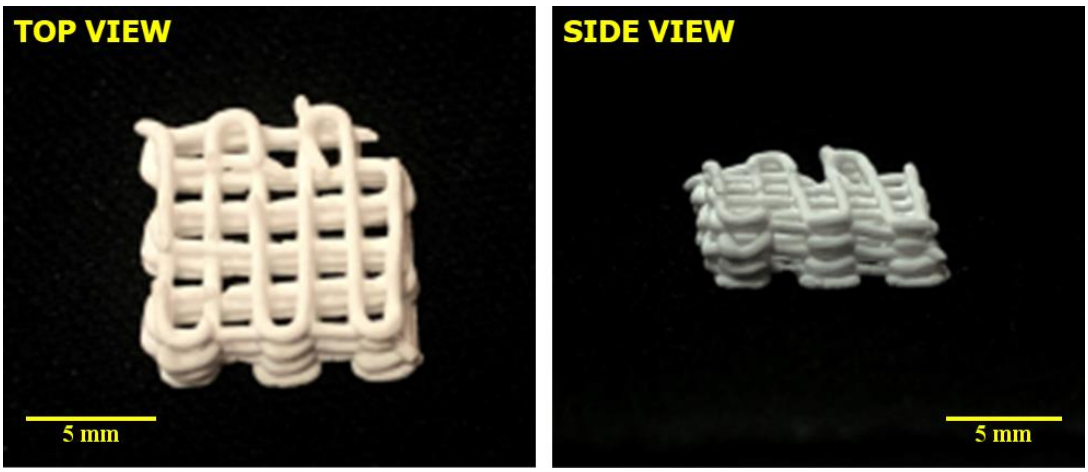


Figure 5.2: Effect of lowering LPR from 0.6 to 0.55 ml/g on the viscosity of the cement-ink, binder concentration:20 wt.% Pluronic F127.

Another approach to control and increase viscosity was using more viscous liquid binder solution. Accordingly, 25 wt.% Pluronic F127 solution was prepared-and replaced with 20 wt.% containing binder solution in a new modified ink. Meanwhile, LPR is increased from 0.6 to 0.65 according to an educated guess in order to catch an optimal window for injectability. The syringe barrel temperature was set also to 17 °C, to tune viscosity. Additionally, air pressure of the device was set 1.6 bar during the printing and printing speed was 3 mm/s. The printed scaffold is given in Figure 5.3 to show effect of viscosity by modifying binder amount. Apparently, the viscosity of the binder was still low, since fusion between the layers were observed and the scaffold collapsed again in the z-direction (side view). In the following printing studies binder in the ink was fixed to 25 wt.% Pluronic F127.

In the following trial LPR is decreased 0.65 to 0.60 and higher printing speed of 6 mm/s was employed at 17 °C and 2.5 bar to see the effect of printing speed on shaping and shape conversion. The construct is shown in Figure 5.4, the structural stability in z-direction (side view) was better, while fusion between the strands were still observable.

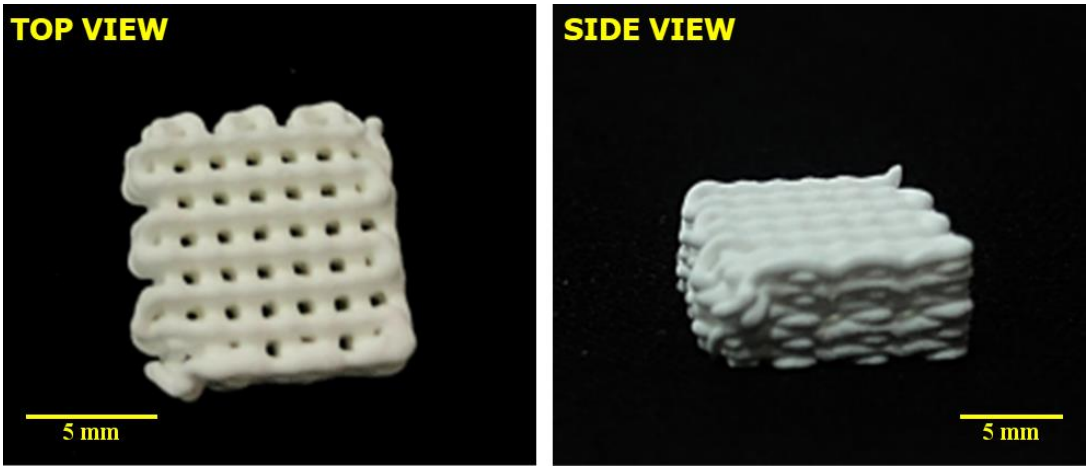


Figure 5.3: Effect of increasing binder concentration in DI water from 20 to 25 wt.% Pluronic F127 on the viscosity of the cement-ink, LPR:0.65

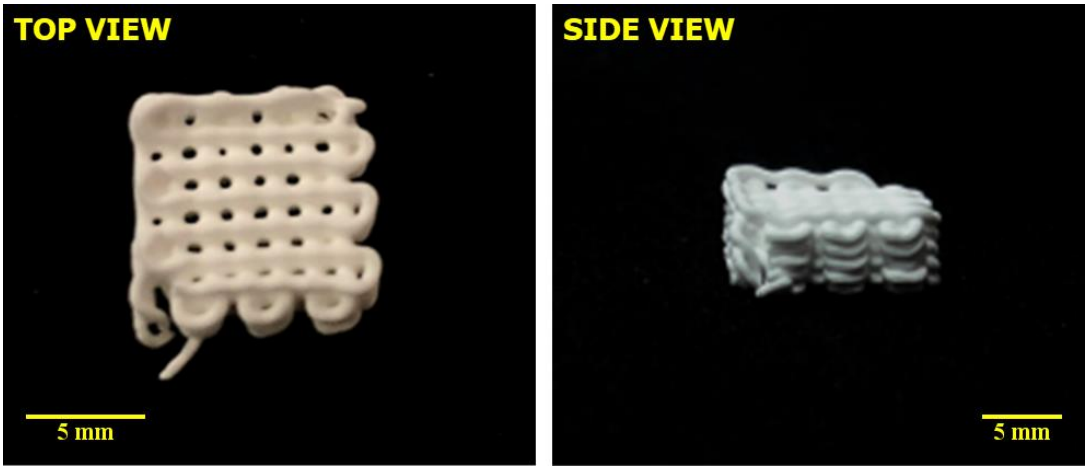


Figure 5.4: Effect of printing increased speed (from 3 to 6 mm/s) on the structural integrity of the scaffold; Binder concentration: 25 wt.% Pluronic F127, LPR:0.6

As an alternative strategy, printing tip diameter (opening orifice) was changed from 0.6 mm to 0.4 mm (20G to 22G). Space between the strands consequently decreased. Rest of the parameters (17 °C, 6 mm/s) were same with the previous ink-printing trial scaffold fabrication except air pressure since the smaller syringe tip requires more air pressure to push cement ink through the opening. By looking at the Figure 5.5, reducing the tip size provide better resolution for the features of the scaffold (top view) however it did not prevent partial collapsing of layers in z-direction (side view).

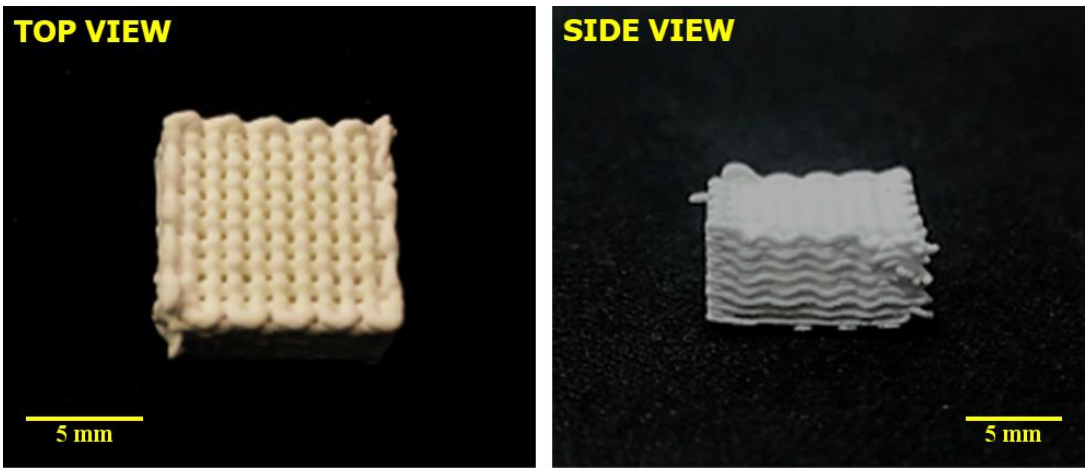


Figure 5.5: Effect of reducing tip(opening orifice) diameter on printing and on the scaffold integrity, Binder concentration: 25 wt.% Pluronic F127, LPR:0.6

As a final approach, to avoid and minimize collapse a new was fabricated fabricated by increasing the printing speed from 6 to 9 mm/s and air pressure is increased accordingly. As can be seen from scaffold in Figure 5.6, the fusion between strands in z-direction is at minimal and the individual layers are more distinct.

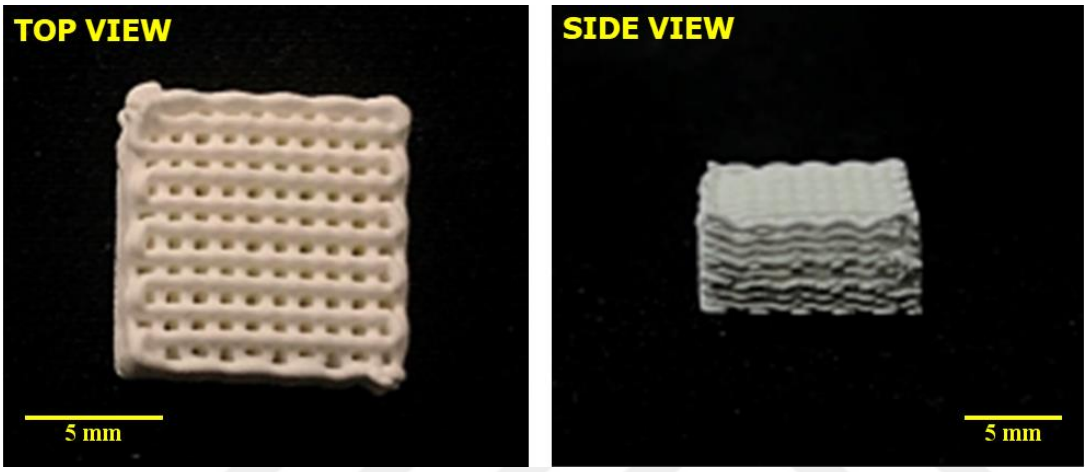


Figure 5.6: Effect of increased printing speed on the printing and on the scaffold integrity, Binder concentration: 25 wt.% Pluronic F127, LPR:0.6

After various trial and error based experiments by employing different ink formulations and equipment parameters, it is clear that some modifications on the previously optimized cement paste formulations for hand-printing (see Section 4.1) should be implemented. The ideal direct-ink writing conditions are as follows: LPR:0.6, Binder Concentration in DI water: 25 wt.% Pluronic F127, Printing Temperature:17 °C, Tip Size (Inner Diameter): 0.4 mm, Printing Speed: 9 mm/s, Pushing power: 2.5-3.5 bar. Some of the TCP scaffolds printed based on optimized parameters are shown in Figure 5.7.



Figure 5.7: 3D Printed TCP Scaffolds with the optimized parameters: LPR:0.6, Binder Concentration: 25 wt.%, Tip I.D:0.4 mm, Printing Speed:9 mm/s

Meanwhile, the hybrid ink formulations containing CSH together with TCP has to be modified some, as CSH sets faster than TCP and working-ability and injection becomes more difficult. This required a marginal compositional adjustment: LPR ratio was set 0.6 for TCP scaffolds, 0.65 for CSH10 scaffolds and 0.7 for CSH25 scaffolds due to fast setting reaction of CSH particles would make harder to push particles during the 3D printing of the pastes.

Additionally, printed CSH10 and CSH25 construct tended to disintegrate in the hydration media, DI water. XRD examination also suggested that complete hydration of TCP particles is not possible after 72 h condition. In order to ensure complete hydration, PBS solution was used as hydration media for CSH10 and CSH25 scaffolds to accelerate the cement conversion of the scaffolds.

5.2 Microstructural Characterization of 3D Printed Scaffolds: Porosity

3D scaffolds were deliberately fabricated with mesh-like structure in order to demonstrate the potential of suggested printing in developing intricate and complex structures. Such bioceramic forms with controlled geometrical pores may be potentially used as bone analogs and can be also employed as bone tissue engineering platforms. Another reason for constructing geometrically uniform constructs was to obtain sam-

ples for mechanical testing.

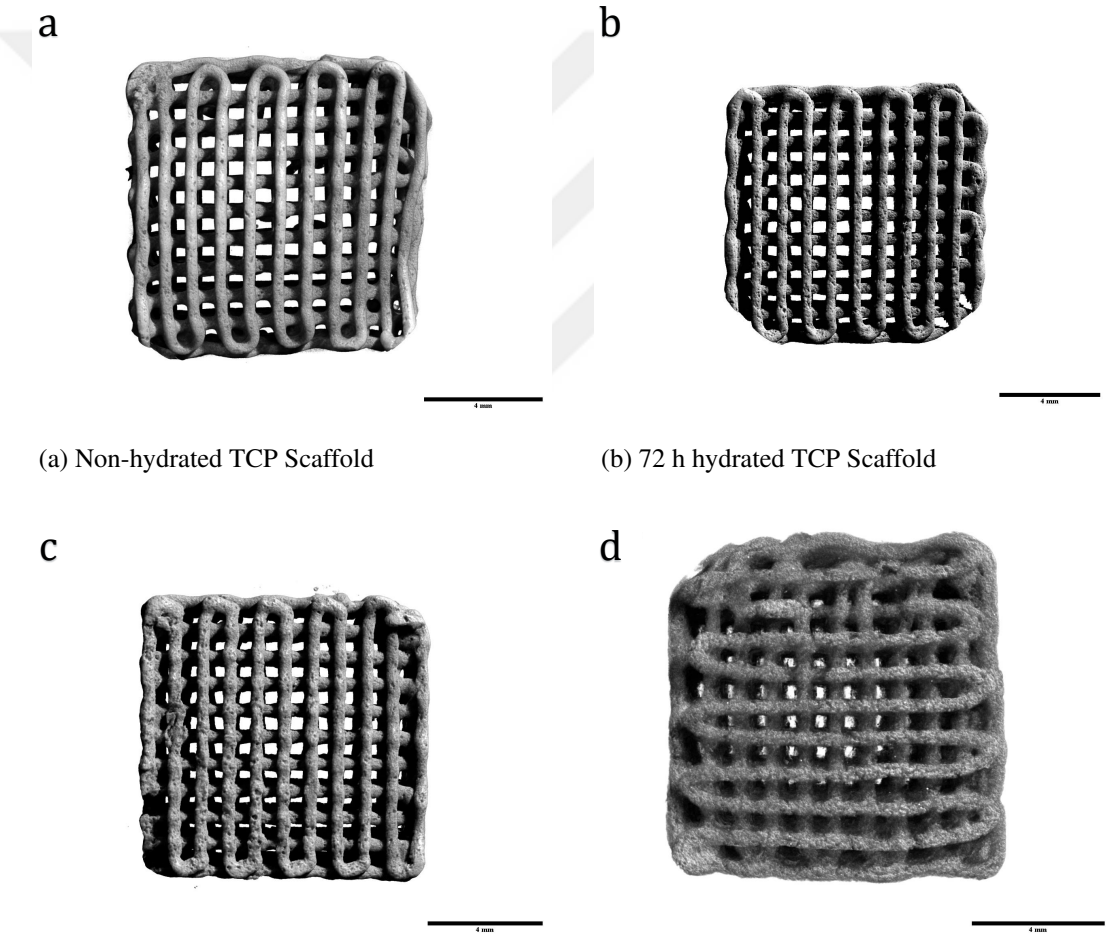
The size and distribution of open pores in a mesh construct can be controlled with the printing pattern/scheme. The intrinsic closed porosities, on the other hand, within the individual mesh lines (strands) can change with the amount of binder (by dissolution or degradation during hydration), or also by the possible chemical/physical changes for the inorganic component. The cement precursors as shown in previous chapter can convert to soluble by- and end-products. Additionally, the pore size and distribution is also related the hydration mechanism of the powders since hydration involves dissolution and precipitation of the matrix material. Even though obtaining closed porosities for building layers was not a direct intention of the study, it can be good strategy for obtaining printed bioceramic constructs with macro porosity(mm's in size) and microporosity (100 μm's). Therefore, the intrinsic porosity of the 3D Direct-Ink printed scaffolds has been investigated in detail. TCP 3D printed scaffold were hydrated in DI water at 37 °C for 72 h. CSH10 and CSH25 3D printed scaffolds were hydrated in PBS solution at 37 °C for 72 h and change in the porosity upon hydration was monitored by a combination of various analytical techniques. These involved characterization studies via Micro-CT (μ-CT), SEM and the Archimedes density measurement.

5.2.1 Micro-CT and SEM Images of the Scaffolds

Micro-CT is a great tool to detect open and closed porosities in a bulk structure. The Micro-CT images of non-hydrated TCP, 72 h hydrated TCP, CSH10 and CSH25 scaffolds were constructed using in-build software to investigate the structural integrity and the surface finish quality of the scaffolds. Top, isometric and cross-sectional views are given in Figures 5.8, 5.9 and 5.10 respectively highlighting the porosity differences between the samples and surface finish before and after the hydration.

As it seen in the Figure 5.8, non-hydrated TCP-based scaffold (given in Figure 5.8a) has the best surface quality with a smooth well-integrated appearance of the top layer. The 72 h-hydrated counterpart of this scaffold shown in Figure 5.8b, exhibits as relatively rough surface, designating some physical changes upon hydration. The scaffold obtained using TCP:25 wt% CSH hybrid ink (CSH25, hydrated for 72 h) at the other

end, shown in Figure Figure 5.8d, has distinctly different surface with rough, porous and somewhat disintegrated form. Partial disintegration and partially broken nature of CSH25 scaffold is also revealed by the discontinuities within the structure and thinning of the strands. 72 h-hydrated CSH10 scaffolds (given in Figure 5.8c) show moderate surface quality resembling that for TCP-based scaffold. It looks like that hydration may lead to a change on surface quality due to etching/dissolution creating porosity. This effect is more pronounced scaffold produced using high calcium sulfate containing cement inks.



(a) Non-hydrated TCP Scaffold

(b) 72 h hydrated TCP Scaffold

(c) 72 h hydrated CSH10 Scaffold

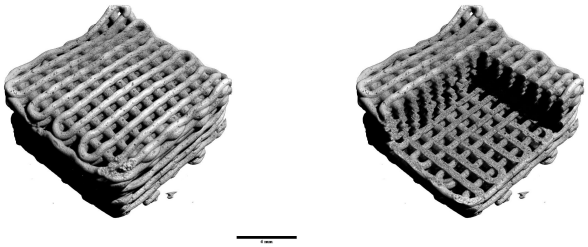
(d) 72 h hydrated CSH25 Scaffold

Figure 5.8: Top view of scaffolds after constructing 3D structure via software shows the alignment of the scaffold and surface finish quality before and after the hydration

Isometric views with cross-sectional cut images of the scaffolds, in Figure 5.9, show the structural details for the interior parts of the scaffolds. By comparing the micro-CT images, it is possible to say that CSH25 (given in Figure 5.9d) exhibits the highest porosity for the individual strands. This is also valid for all positional sections including the central part.Non-hydrated and hydrated TCP scaffolds remain with minimal porosity. The porosities surely may affect the mechanical properties of the scaffolds. The partial disintegration observed for CSH25 seems to be critical. However, the overall structural integrity of the scaffolds is maintained by perfect alignment and architecture of the strands. These were preserved for all scaffolds even though some scaffolds were de-fragmented on surface. Additionally, the cross-sectional images of the scaffolds confirmed that aqueous hydration solution infiltrated interior parts of the strands by creating porosities (comparing non-hydrated scaffold with others). This means that hydration does not occur only surface but proceeds every part of the scaffolds including strands.

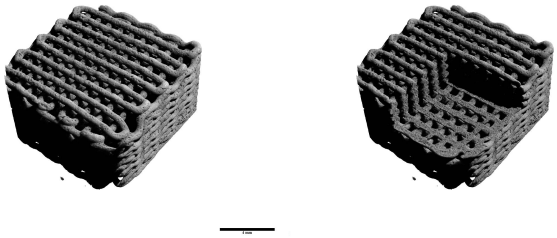
In Figure 5.10, cross-sectional views of scaffolds from top are given to show porosities formed within the strands. For each sample, porosities are present for the scaffolds and it is hard to say that dissolution of CaS particles occurred in the middle layer.From Figure 5.9, it is possible to say that surfaces of the scaffolds were greatly affected by the dissolution of the particles. For Figure 5.10a, porosities inside of the strands are clearly seen. The porosities present for non-hydrated TCP scaffolds were formed during the Direct-Ink Writing of the scaffolds. Formulation of the cement-ink had LPR value of 0.6 which was far away from most packing LPR value of 0.35. For Figure 5.10b and Figure 5.10c porosities were present but it is not comparable with non-hydrated condition. On the other hand, Figure 5.10d shows that the porosities present in the strands enormously increased for CSH25 scaffolds.Also the structural homogenity of the CSH25 scaffold is highly disturbed.

a



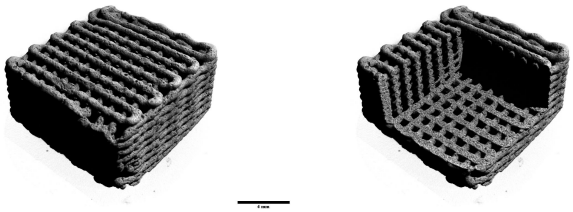
(a) Non-hydrated TCP Scaffold

b



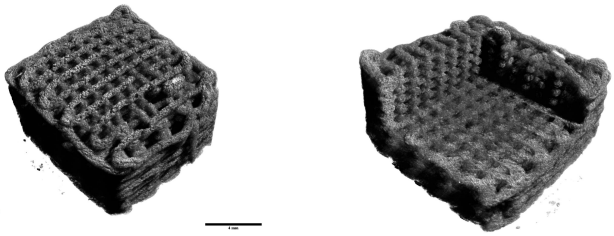
(b) 72 h hydrated TCP Scaffold

c



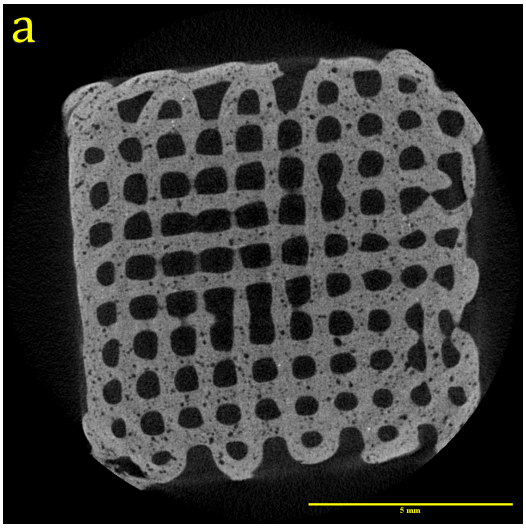
(c) 72 h hydrated CSH10 Scaffold

d

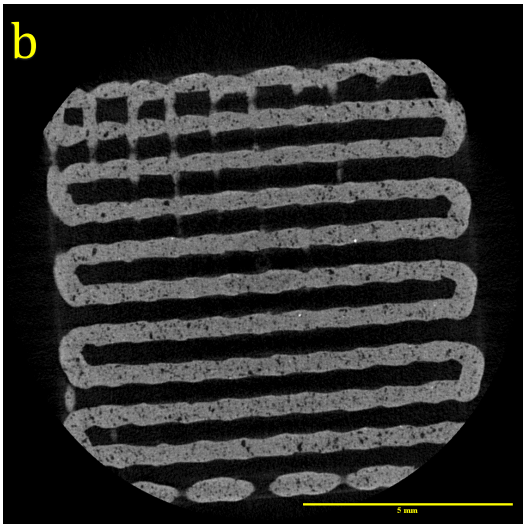


(d) 72 h hydrated CSH25 Scaffold

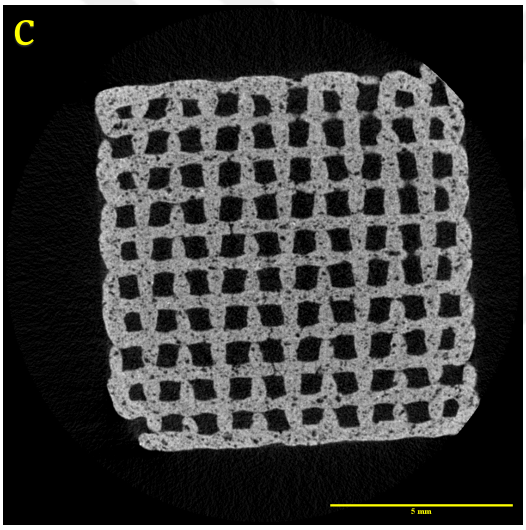
Figure 5.9: Isometric and cross-sectional views of scaffolds after constructing 3D structure via software shows the structural integrity before and after hydration and porosities are observable clearly



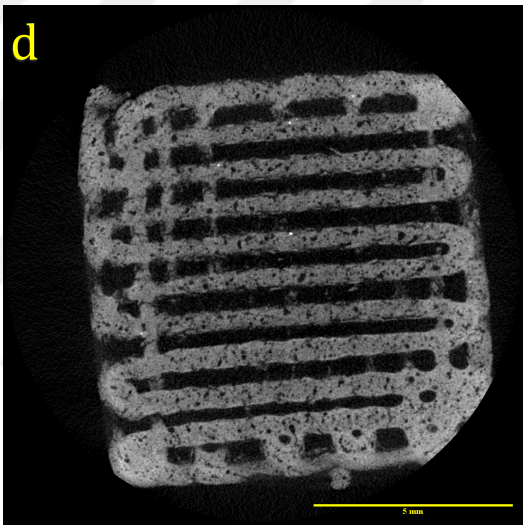
(a) Non-hydrated TCP Scaffold



(b) 72 h hydrated TCP Scaffold



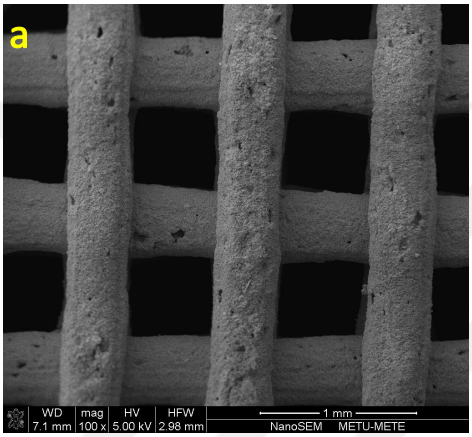
(c) 72 h hydrated CSH10 Scaffold



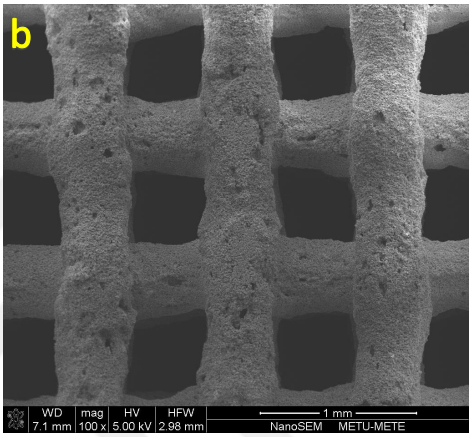
(d) 72 h hydrated CSH25 Scaffold

Figure 5.10: Cross-sectional views of the scaffolds directly taken without processing show the porosities inside the structures and alignment between the strands; (a) Non-hydrated TCP Scaffold, (b) 72 h hydrated TCP Scaffold and (c) 72h hydrated TCP Scaffold shows good alignment geometrically while (d) 72 h hydrated CSH25 Scaffold deteriorated.

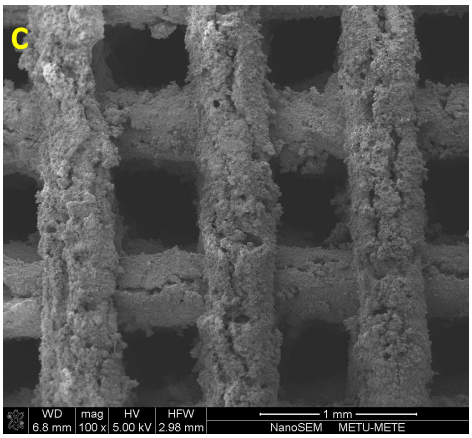
The printed scaffolds were investigated with SEM to reveal microstructural differences, porosities and to the detect any structural deterioration. SEM micrographs of 72 h hydrated samples are shown Figure 5.11, 5.12 and 5.13 with different magnifications. The general view images at relatively small magnification as shown in Figure 5.11, are somewhat similar to the top view of micro-CT images, exhibiting a gradual porosity increase and slight structural degradation as a function of CSH amount. The images obtained at higher magnification in Figure 5.12 exhibit details of individual strands and their surface quality for all scaffolds. The porosity change



(a) 72 h hydrated TCP Scaffold



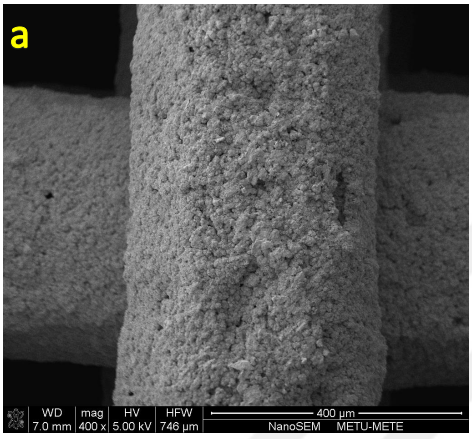
(b) 72 h hydrated CSH10 Scaffold



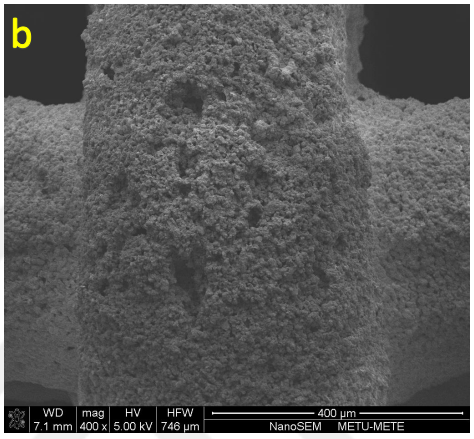
(c) 72 h hydrated CSH25 Scaffold

Figure 5.11: SEM images at x100 magnification shows as CSH content increases (from a to c), disintegration of the scaffolds increases (all scaffolds were hydrated for 72 h at 37 °C).

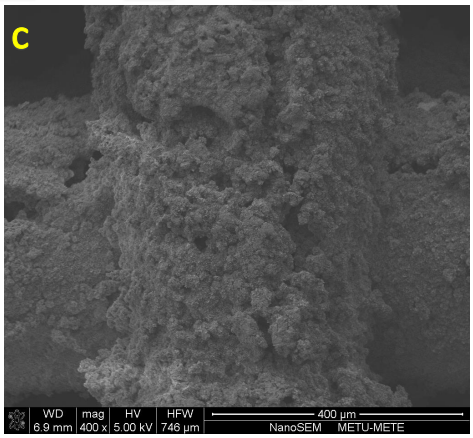
with highest CSH amount (CSH25) and dissolution of it is much more evident and clear. The porosity levels, as it appears from the surface, for TCP and CSH10 are comparable. Even though, a homogeneously distributed micro porosity can be beneficial from the biological perspective in case of potential use as an implant, a high porosity may cause immature mechanical stability and strength. For processing with printing the porosity distribution solely depends on the homogeneous distribution of the TCP and CSH particles within the ink loaded to the syringe which is difficult to control.



(a) 72 h hydrated TCP Scaffold



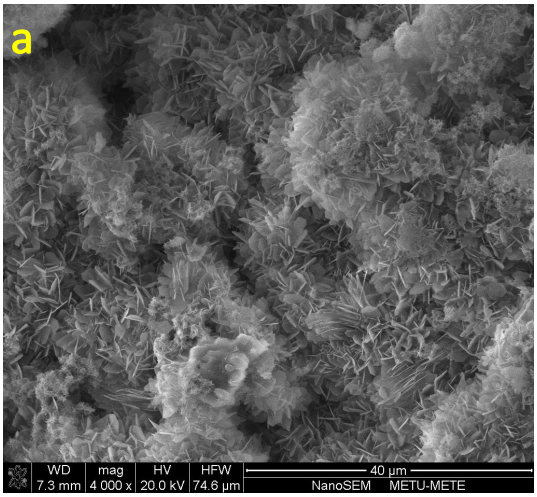
(b) 72 h hydrated CSH10 Scaffold



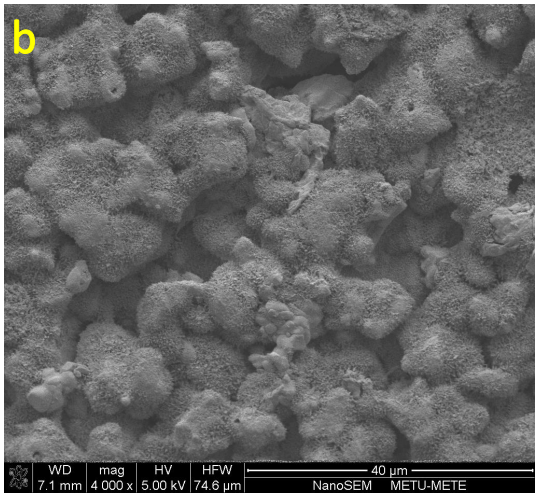
(c) 72 h hydrated CSH25 Scaffold

Figure 5.12: SEM images at x400 magnification show the single strand and its integrity. (a) TCP and (b) CSH10 scaffolds have kept its structural integrity where (c) CSH25 strands got thinner after the hydration (all scaffolds were hydrated for 72 h at 37 °C).

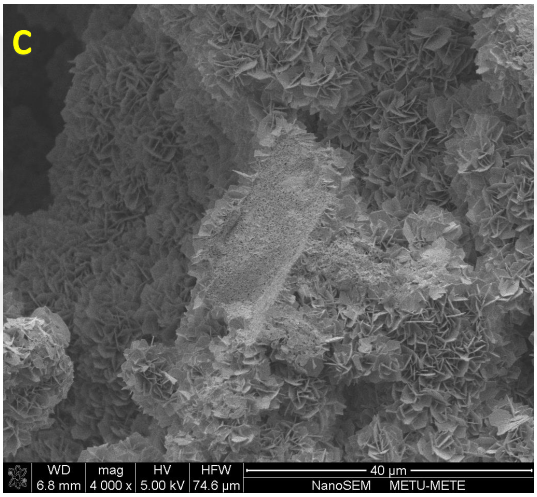
The crystal size level SEM images in Figure 5.13 with highest magnification show morphologies of Ca-phosphate and Ca-sulfate components iof the scaffolds. This figures are for hydrated 3D printed structures. Hydration of the TCP particles, as revealed by flaky HAp crystals were observed profoundly for the TCP scaffolds (as shown in Figure 5.13a). A partial hydration of TCP phase was observed for the CSH10 and CSH25 scaffolds after 72 h (given in Figure 5.13b and Figure 5.13c respectively). Using PBS solution accelerated the HAp formation for all formulations while XRD data given in the previous section suggested that full hydration of TCP particles was not possible by using only DI water. However, using PBS might had increased the dissolution of Ca-sulfate phases since the PBS solution contains phosphate ion and consequently increased the super saturation of the calcium and phosphate ions. Different and crystals Figure 5.13c) were attributed to the CaS phase, which presumably does not contribute any mechanical support for the scaffold since it does not show any evident that they help interlocking with the HAp plates in the structure.



(a) 72 h hydrated TCP Scaffold



(b) 72 h hydrated CSH10 Scaffold



(c) 72 h hydrated CSH25 Scaffold

Figure 5.13: The SEM images of different scaffold compositions shows the morphology of the hydrated particles. (a) plate-like morphology of CDHAp particles along with some unreacted TCP(left bottom), (b) smaller CDHAp particles compared to TCP scaffold, (c) plate-like morphology of the CDHAp along with spongy-like structure of CaS phase.

5.2.2 Archimedes Porosity Measurement and Compression Test of the Printed Scaffolds

Porosity shapes and the distribution of the porosities were characterized in the previous section, but Archimedes porosity measurement is given here to correlate mechanical testing results in a conclusive manner. Additionally, porosities (shown in Figure 5.10) inside of the strands cannot attribute to only CaS dissolution. Porosities present in the structure might be related to the cement-ink preparation for Direct-Ink Writing. CSH25 scaffolds were printed with LPR ratio: 0.7 while TCP scaffolds were fabricated LPR:0.6. Using more liquid phase eventually leads more porosity structure. Bulk porosity values are given in Figure 5.14. It is seen that bulk volume porosity of the CSH25 scaffold (average value of 52.0±3.7) enormously increased compared to TCP scaffold's bulk volume porosity (average value of 45.1±1.8). It was expected for two reasons: Increased amount of liquid phase during the preparation of the cement-ink naturally causes more porosity in the structure. Additionally, dissolution of Ca-sulfate particles in the hybrid cements may create more porous structure both on surface and the inside of the structure. CSH10 scaffolds have average porosity of 48.7±2.6 and it correlates the assumption that as CaS phase amount increase in the cement-ink formulation, the scaffold become more porous.

For determining mechanical properties of the scaffolds, uniaxial compression test is applied to the scaffolds. Initially, as a control group non-hydrated scaffolds were subjected to uniaxial compression test. However, green body state (or as-printed state) of the scaffolds was very low in strength ($\leq$0.1 MPa). Even though, few trials had been practiced and it showed that it is hard to get clear data. As printed scaffolds were squeezed to more condition state without showing any distinct yield point during the compression test. It might be related to Pluronic F127 content left in the structure.

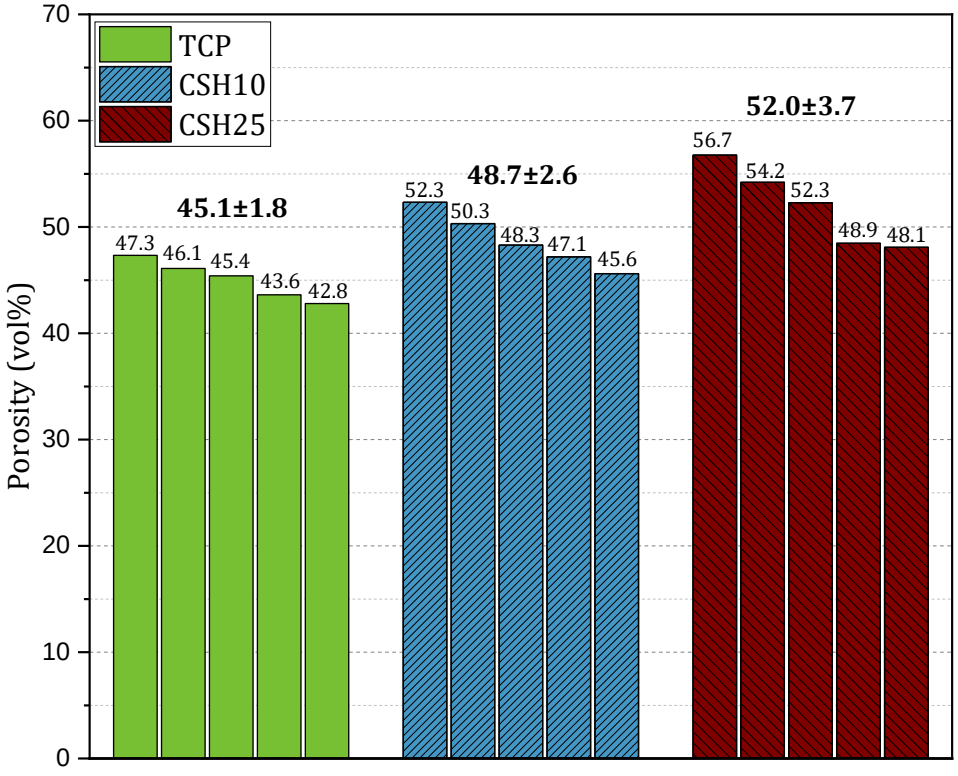


Figure 5.14: Bulk porosities (in volume %) of TCP, CSH10 and CSH25 scaffolds.

Uniaxial compression test results were given in Figure 5.15. As it is seen in the Figure 5.15, compressive strength of the TCP scaffolds decreased from 5.01±0.37 to 2.29±0.53 for CSH25 scaffolds. As the amount of CaS phase in cement-ink formulation increases, the mechanical strength of the scaffolds decreases. Micro-CT and SEM images of printed scaffolds already showed that CSH25 scaffold is highly disintegrated and have enormous pore sizes compared with other scaffold formulation. In any case, none of the CSH25 scaffold samples (max: 2.94 MPa) did not reach the compressive strength level of TCP scaffolds (min:4.55MPa) as it is expected. Also, SEM images showed that Ca-sulfate phase left in the scaffold may not interlock physically with the plate-like HAp. Thus, it does not provide any mechanical support at all for 72 h hydrated samples. However, CSH10 scaffolds showed intermediate compressive strength value of 3.52±0.27 MPa.

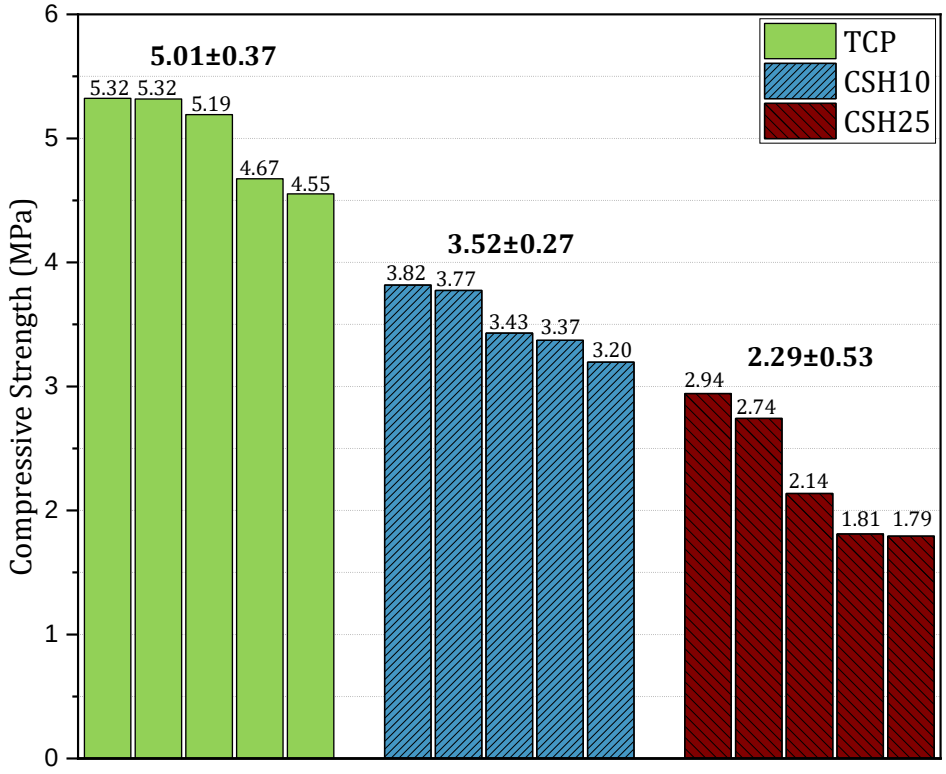


Figure 5.15: Uniaxial compressive strength values (in MPa) of TCP, CSH10 and CSH25 scaffolds.

Additionally, the compressive strength values for CSH25 scaffolds were deviated too much, which it may lead to anticipate that increasing Ca-sulfate share in the composition of cement-ink caused the mechanical instability to the scaffold. CSH10 scaffolds were failed around the same compressive strength values which may make them candidate to use in similar applications of bare TCP cements if the higher porosity is desired for the implanted tissue. Nevertheless, TCP scaffolds had the highest compressive strength values, which is directly related to the porosity size and distribution. In other words, volume of hydrated TCP (or CDHAp) phase is much highest for pure TCP scaffolds. It is more likely for CaP:CaS hybrid cements to be used as pore generator rather than providing mechanical support to the structure. Compressive strength of the scaffolds can be attributed to mechanical interlocking mechanism of the precipitated CDHAp particles within the network. For that reason, all scaffolds were hydrated for 72 h to represent the composition effect for mechanical properties.

CHAPTER 6

CONCLUSIONS

Synthesis of Reactive Cement Precursor: α-TCP

α-TCP was initially synthesized by the solid-state reaction of monetite ($CaHPO_4$) and calcium carbonate (CaCO3) at 1200 °C for 2 h in the open air furnace. However, XRD diffractograms of this reactant combination contained hydroxyapatite (HAp) phase together with α-TCP. In order to obtain phase pure α-TCP, monetite is converted to calcium pyrophosphate (CPP or $Ca_2P_2O_7$) by firing operation to remove possible water or OH/H species. Another α-TCP batch was synthesized by the solid state reaction between $Ca_2P_2O_7$ and $CaCO_3$ powders in an identical process conditions. There was no HAp phase detected in the XRD diffractogram of second reactant combination. After SEM investigation of α-TCP powders, there was no morphological difference between both powders. Although there was no morphological difference for both α-TCP particles of different synthesis routes HAp particles, as a secondary phase were observed in the SEM images of the first route. It is critical to eliminate secondary phases from the mixture to control and to promote hydration based cement setting reaction. Therefore, a synthesis protocol has been established to obtain phase pure and reactive α-TCP powders. These powders were employed as a cement printing paste/ink component.

Studies with Different Binder Solutions and Reactivity of α-TCP/CSH Hybrid Cements

Injectable cement paste (for manual printing of dummy scaffolds) was developed with Pluronic F127:water solutions at various concentrations (20 wt.%, 25 wt.%, 30 wt.% in DI water) or alginate:water solution (2 wt.% in DI water) to adjust the viscosity of the cement paste. In injectability experiments, liquid to powder ratios (LPR) were set as 0.55, 0.6 and 0.65 ml/g for each binder formulation. Alginate cement pastes were highly injectable with a 94.4±1.0% injectability at LPR:0.65. However, cement pastes prepared with 2 wt.% did not exhibit structural stability upon injecting, even collapsed for LPR:0.65 after injection. Cement paste prepared with Pluronic F127 showed better structural integrity compared to the alginate for each formulation. The only cement paste did not show any injectability was the one prepared at Pluronic concentration of 30 wt.% with LPR:0.55. Increasing LPR provided 30 wt.% Pluronic F127:α-TCP cement pastes to become injectable at same environmental conditions. The cement pastes prepared with Pluronic F127 solution reached highest injectability as 90.7±1.4% at lower concentrations (20 wt.%) and higher LPR values (0.65). Even though injectability values were better at LPR:0.65, structural integrity of the cement pastes was questionable. At the end of these optimization studies, proper cement printing paste formulation was determined as 20 wt.% F127 and LPR:0.6 with 82.1±3.6% and these printing parameters were employed in exploring hydration behavior of printed cement-based dummy scaffolds.

TCP and calcium sulfate hemihydrate containing; CSH10 (90 wt.% TCP: 10 wt.% CSH) and CSH25 (75 wt.% TCP: 25 wt.% CSH) cement pastes were hand-injected. Structurally stable dummy scaffolds with well-preserved shapes were obtained. These scaffolds eere hydrated for different time intervals. Setting reactions were conducted for 6, 12, 24, 48 and 72 h respectively at 37 °C in excess DI water. As-printed and hydrated products were investigated by XRD, FTIR and SEM. According to XRD, FTIR analyses and SEM investigations pure TCP scaffolds were hydrated to calcium deficient HAp (CDHAp) in 24 h while TCP in the CSH10 and CSH25 structures could not complete the hydration reaction in 72 h. Increased amount of CSH altered the setting reactivity of α-TCP powders. CSH phase present in CSH10 structure was

set/transformed to CSD in as-printed condition. CSD phase disappeared after 12 h which indicated that CaS phase dissolved in time. CSH present in CSH25 structure did not hydrate to CSD phase in 12 h. It is seen that a CSH improves initial hardening during/after injection/printing, however higher amount of CSH phase in as-prepared cements slowed down setting reaction kinetics.

Direct-Ink Writing of Cement-Inks

Optimized cement paste formulations were successfully adapted for Direct-Ink Writing operation for printing geometrically more complex and intricate scaffolds. Several equipment specific printing parameters were established by utilizing and fine tuning of hand printing formations. These involved parameters: LPR, Pluronic F127 concentration in DI water, printing speed, cement-ink temperature, tip opening/orifice size were conducted for TCP scaffolds. Optimized parameters were found as LPR:0.6, Pluronic F127 concentration: 25. wt%, cement-ink temperature:17 °C, printing speed: 9 mm/s, tip opening size: 0.4 mm for TCP scaffolds. Higher LPR values of 0.65 for CSH10 and 0.7 for CSH25, respectively to ease printing with these fast-setting inks.

Similarly, 3D printed TCP scaffolds were hydrated in excess DI water for 72 h at 37 °C while 3D printed CSH10 and CSH25 scaffolds were hydrated in phosphate buffered solution for 72 h at 37 °C. Micro-CT scan, microstructural investigation with , Archimedes porosity measurement and uniaxial compressive strength tests were performed for the characterization of 3D printed scaffolds. According to porosity measurement, 3D printed CSH10 and CSH25 scaffolds had higher bulk porosity (48.7±2.6 vol% and 52.0±3.7 vol% respectively) compared to TCP scaffolds (45.1±1.8 vol%). CaS phases dissolved during hydration. SEM and micro-CT investigations showed that CSH25-based structurally deteriorated. Consequently, compressive strength values of CSH25 scaffolds were found 2.29±0.53 MPa as the lowest amongs others, while compressive strength values of TCP were found 5.01±0.37 MPa as the highest. It is concluded that TCP:CSH hybrid cements did not exhibited higher strength, due to dissolution CaS phases. CSH could be only used as initial setting-promoter during printing and an interconnected pore generator rather than mechanical reinforcement.

REFERENCES

[1] P. Fratzl and R. Weinkamer, "Nature's hierarchical materials," *Progress in Materials Science*, vol. 52, no. 8, pp. 1263–1334, 2007.

[2] S. Weiner and H. D. Wagner, "The material bone: Structure-mechanical function relations," *Annual Review of Materials Science*, vol. 28, no. 1, pp. 271–298, 1998.

[3] J. Y. Rho, L. Kuhn-Spearing, and P. Zioupos, "Mechanical properties and the hierarchical structure of bone," *Medical Engineering and Physics*, vol. 20, no. 2, pp. 92–102, 1998.

[4] U. G. Wegst, H. Bai, E. Saiz, A. P. Tomsia, and R. O. Ritchie, "Bioinspired structural materials," *Nature Materials*, vol. 14, no. 1, pp. 23–36, 2015.

[5] M. F. Young, "Bone matrix proteins: their function, regulation, and relationship to osteoporosis.," *Osteoporosis international : a journal established as result of cooperation between the European Foundation for Osteoporosis and the National Osteoporosis Foundation of the USA*, vol. 14 Suppl 3, pp. 35–42, 2003.

[6] M. J. Olszta, X. Cheng, S. S. Jee, R. Kumar, Y. Y. Kim, M. J. Kaufman, E. P. Douglas, and L. B. Gower, "Bone structure and formation: A new perspective," *Materials Science and Engineering R: Reports*, vol. 58, no. 3-5, pp. 77–116, 2007.

[7] S. V. Dorozhkin, "Calcium orthophosphates in nature, biology and medicine," *Materials*, vol. 2, no. 2, pp. 399–498, 2009.

[8] R. Murugan and S. Ramakrishna, "Development of nanocomposites for bone grafting," *Composites Science and Technology*, vol. 65, no. 15-16 SPEC. ISS., pp. 2385–2406, 2005.

[9] C. Rey, C. Combes, C. Drouet, and M. J. Glimcher, "Bone mineral: Update on

chemical composition and structure," *Osteoporosis International*, vol. 20, no. 6, pp. 1013–1021, 2009.

[10] J. A. Sterling and S. A. Guelcher, "Biomaterial scaffolds for treating osteoporotic bone," *Current Osteoporosis Reports*, vol. 12, no. 1, pp. 48–54, 2014.

[11] D. Arcos, A. R. Boccaccini, M. Bohner, A. Díez-Pérez, M. Epple, E. Gómez-Barrena, A. Herrera, J. A. Planell, L. Rodríguez-Mañas, and M. Vallet-Regí, "The relevance of biomaterials to the prevention and treatment of osteoporosis," *Acta Biomaterialia*, vol. 10, no. 5, pp. 1793–1805, 2014.

[12] J. A. Siddiqui and N. C. Partridge, "Physiological bone remodeling: Systemic regulation and growth factor involvement," *Physiology*, vol. 31, no. 3, pp. 233–245, 2016.

[13] C. Conference, "Osteoporosis Prevention, Diagnosis, and Therapy," vol. 285, no. 6, 2020.

[14] S. Wu, X. Liu, K. W. Yeung, C. Liu, and X. Yang, "Biomimetic porous scaffolds for bone tissue engineering," *Materials Science and Engineering R: Reports*, vol. 80, no. 1, pp. 1–36, 2014.

[15] H. S. Sohn and J. K. Oh, "Review of bone graft and bone substitutes with an emphasis on fracture surgeries," *Biomaterials Research*, vol. 23, no. 1, pp. 4–10, 2019.

[16] W. Habraken, P. Habibovic, M. Epple, and M. Bohner, "Calcium phosphates in biomedical applications: Materials for the future?," *Materials Today*, vol. 19, no. 2, pp. 69–87, 2016.

[17] S. V. Dorozhkin, "Bioceramics of calcium orthophosphates," *Biomaterials*, vol. 31, no. 7, pp. 1465–1485, 2010.

[18] K. Ishikawa, "Bone substitute fabrication based on dissolution-precipitation reactions," *Materials*, vol. 3, no. 2, pp. 1138–1155, 2010.

[19] V. Campana, G. Milano, E. Pagano, M. Barba, C. Cicione, G. Salonna, W. Lattanzi, and G. Logroscino, "Bone substitutes in orthopaedic surgery: from ba-

sic science to clinical practice," *Journal of Materials Science: Materials in Medicine*, vol. 25, no. 10, pp. 2445–2461, 2014.

[20] L. F. Peltier, E. Y. Bickel, R. Lillo, and M. S. Thein, "The use of plaster of paris to fill defects in bone.," *Annals of surgery*, vol. 146, no. 1, pp. 61–69, 1957.

[21] J. W. Bullard, H. M. Jennings, R. A. Livingston, A. Nonat, G. W. Scherer, J. S. Schweitzer, K. L. Scrivener, and J. J. Thomas, "Mechanisms of cement hydration," *Cement and Concrete Research*, vol. 41, no. 12, pp. 1208–1223, 2011.

[22] M. Sadat-Shojai, M. T. Khorasani, E. Dinpanah-Khoshdargi, and A. Jamshidi, "Synthesis methods for nanosized hydroxyapatite with diverse structures," *Acta Biomaterialia*, vol. 9, no. 8, pp. 7591–7621, 2013.

[23] E. R. Kreidler and F. Hummel, "Phase Relationships in the System SrO-P,O, and the Influence of Water Vapor on the Formation of Sr,P,O,," *Inorganic Chemistry*, vol. 6, no. 5, pp. 884–891, 1967.

[24] R. G. Carrodeguas and S. De Aza, "α-Tricalcium phosphate: Synthesis, properties and biomedical applications," *Acta Biomaterialia*, vol. 7, no. 10, pp. 3536–3546, 2011.

[25] G. Fernandez de Grado, L. Keller, Y. Idoux-Gillet, Q. Wagner, A. M. Musset, N. Benkirane-Jessel, F. Bornert, and D. Offner, "Bone substitutes: a review of their characteristics, clinical use, and perspectives for large bone defects management," *Journal of Tissue Engineering*, vol. 9, 2018.

[26] G. Cicek, E. A. Aksoy, C. Durucan, and N. Hasirci, "Alpha-tricalcium phosphate (α-TCP): Solid state synthesis from different calcium precursors and the hydraulic reactivity," *Journal of Materials Science: Materials in Medicine*, vol. 22, no. 4, pp. 809–817, 2011.

[27] D. Brazete, P. M. Torres, J. C. Abrantes, and J. M. Ferreira, "Influence of the Ca/P ratio and cooling rate on the allotropic $\alpha \leftrightarrow \beta$-tricalcium phosphate phase transformations," *Ceramics International*, vol. 44, no. 7, pp. 8249–8256, 2018.

[28] H. Kihara, M. Shiota, Y. Yamashita, and S. Kasugai, "Biodegradation process of α-TCP particles and new bone formation in a rabbit cranial defect model," *Jour-*

nal of Biomedical Materials Research - Part B Applied Biomaterials, vol. 79, no. 2, pp. 284–291, 2006.

[29] F. Tamimi, Z. Sheikh, and J. Barralet, "Dicalcium phosphate cements: Brushite and monetite," *Acta Biomaterialia*, vol. 8, no. 2, pp. 474–487, 2012.

[30] C. Moseke and U. Gbureck, "Tetracalcium phosphate: Synthesis, properties and biomedical applications," *Acta Biomaterialia*, vol. 6, no. 10, pp. 3815–3823, 2010.

[31] W. E. Brown, "A new calcium phosphate, water-setting cement," *Cements research progress*, pp. 351–379, 1987.

[32] J. Zhang, W. Liu, V. Schnitzler, F. Tancret, and J. M. Bouler, "Calcium phosphate cements for bone substitution: Chemistry, handling and mechanical properties," *Acta Biomaterialia*, vol. 10, no. 3, pp. 1035–1049, 2014.

[33] A. A. Mirtchi, J. Lemaitre, and N. Terao, "Calcium phosphate cements: study of the β-tricalcium phosphate—monocalcium phosphate system," *Biomaterials*, vol. 10, no. 7, pp. 475–480, 1989.

[34] S. V. Dorozhkin, "Biphasic, triphasic and multiphasic calcium orthophosphates," *Acta Biomaterialia*, vol. 8, no. 3, pp. 963–977, 2012.

[35] R. Z. LeGeros, "Calcium phosphate-based osteoinductive materials," *Chemical Reviews*, vol. 108, no. 11, pp. 4742–4753, 2008.

[36] M. Bohner, "Reactivity of calcium phosphate cements," *Journal of Materials Chemistry*, vol. 17, no. 38, pp. 3980–3986, 2007.

[37] E. Ferńndez, F. J. Gil, M. P. Ginebra, F. C. Driessens, J. A. Planell, and S. M. Best, "Calcium phosphate bone cements for clinical applications. Part I: Solution chemistry," *Journal of Materials Science: Materials in Medicine*, vol. 10, no. 3, pp. 169–176, 1999.

[38] C. Durucan and P. Brown, "α-tricalcium phosphate hydrolysis to hydroxyapatite at and near physiological temperature," *Journal of materials science: Materials in medicine*, vol. 11, no. 6, pp. 365–371, 2000.

[39] O. Gauthier, J. M. Bouler, E. Aguado, P. Pilet, and G. Daculsi, "Macroporous biphasic calcium phosphate ceramics: Influence of macropore diameter and macroporosity percentage on bone ingrowth," *Biomaterials*, vol. 19, no. 1-3, pp. 133–139, 1998.

[40] M. C. von Doernberg, B. von Rechenberg, M. Bohner, S. Grünenfelder, G. H. van Lenthe, R. Müller, B. Gasser, R. Mathys, G. Baroud, and J. Auer, "In vivo behavior of calcium phosphate scaffolds with four different pore sizes," *Biomaterials*, vol. 27, no. 30, pp. 5186–5198, 2006.

[41] C. Durucan and P. W. Brown, "Reactivity of α-tricalcium phosphate," *Journal of Materials Science*, vol. 37, no. 5, pp. 963–969, 2002.

[42] I. Khairoun, M. G. Boltong, F. C. Driessens, and J. A. Planell, "Some factors controlling the injectability of calcium phosphate bone cements," *Journal of Materials Science: Materials in Medicine*, vol. 9, no. 8, pp. 425–428, 1998.

[43] M. Bohner, R. Luginbühl, C. Reber, N. Doebelin, G. Baroud, and E. Conforto, "A physical approach to modify the hydraulic reactivity of α-tricalcium phosphate powder," *Acta Biomaterialia*, vol. 5, no. 9, pp. 3524–3535, 2009.

[44] C. L. Camiré, U. Gbureck, W. Hirsiger, and M. Bohner, "Correlating crystallinity and reactivity in an α-tricalcium phosphate," *Biomaterials*, vol. 26, no. 16, pp. 2787–2794, 2005.

[45] A. Sugawara, K. Asaoka, and S.-J. Ding, "Calcium phosphate-based cements: Clinical needs and recent progress," *Journal of Materials Chemistry B*, vol. 1, no. 8, pp. 1081–1089, 2013.

[46] F. R. McMichen, G. Pearson, S. Rahbaran, and K. Gulabivala, "A comparative study of selected physical properties of five root-canal sealers," *International Endodontic Journal*, vol. 36, no. 9, pp. 629–635, 2003.

[47] S. Takagi, S. Frukhtbeyn, and L. C. Chow, "Fluorapatite-Forming Calcium Phosphate Cements," *Laboratory Animals*, vol. 115, no. 4, pp. 267–276, 2010.

[48] F. J. Martínez-Vázquez, F. H. Perera, P. Miranda, A. Pajares, and F. Guiberteau, "Improving the compressive strength of bioceramic robocast scaffolds by polymer infiltration," *Acta Biomaterialia*, vol. 6, no. 11, pp. 4361–4368, 2010.

[49] S. Panzavolta, B. Bracci, M. L. Focarete, C. Gualandi, and A. Bigi, "Fiber reinforcement of a biomimetic bone cement," *Journal of Materials Science: Materials in Medicine*, vol. 23, no. 6, pp. 1363–1370, 2012.

[50] R. O'Neill, H. O. McCarthy, E. B. Montufar, M. P. Ginebra, D. I. Wilson, A. Lennon, and N. Dunne, "Critical review: Injectability of calcium phosphate pastes and cements," *Acta Biomaterialia*, vol. 50, pp. 1–19, 2017.

[51] M. P. Ginebra, M. Espanol, E. B. Montufar, R. A. Perez, and G. Mestres, "Acta Biomaterialia New processing approaches in calcium phosphate cements and their applications in regenerative medicine," *Acta Biomaterialia*, vol. 6, no. 8, pp. 2863–2873, 2010.

[52] X. Chateau, *Particle packing and the rheology of concrete*. Woodhead Publishing Limited, 2012.

[53] M. Hunger and H. J. Brouwers, "Flow analysis of water-powder mixtures: Application to specific surface area and shape factor," *Cement and Concrete Composites*, vol. 31, no. 1, pp. 39–59, 2009.

[54] E. B. Montufar, Y. Maazouz, and M. P. Ginebra, "Relevance of the setting reaction to the injectability of tricalcium phosphate pastes," *Acta Biomaterialia*, vol. 9, no. 4, pp. 6188–6198, 2013.

[55] P. M. Torres, S. Gouveia, S. Olhero, A. Kaushal, and J. M. Ferreira, "Injectability of calcium phosphate pastes: Effects of particle size and state of aggregation of β-tricalcium phosphate powders," *Acta Biomaterialia*, vol. 21, pp. 204–216, 2015.

[56] K. Ishikawa, "Effects of spherical tetracalcium phosphate on injectability and basic properties of apatitic cement," *Key Engineering Materials*, vol. 240-242, pp. 369–372, 2003.

[57] R. Holdich, *Fundamentals of Particle Technology*. 01 2002.

[58] D. Alves Cardoso, J. A. Jansen, and S. C. Leeuwenburgh, "Synthesis and application of nanostructured calcium phosphate ceramics for bone regeneration.," *Journal of biomedical materials research. Part B, Applied biomaterials*, vol. 100, no. 8, pp. 2316–2326, 2012.

[59] L. Leroux, Z. Hatim, M. Frèche, and J. L. Lacout, "Effects of various adjuvants (lactic acid, glycerol, and chitosan) on the injectability of a calcium phosphate cement," *Bone*, vol. 25, no. 2 SUPPL. 1, pp. 31–34, 1999.

[60] R. O'Neill, H. O. McCarthy, E. Cunningham, E. Montufar, M. P. Ginebra, D. I. Wilson, A. Lennon, and N. Dunne, "Extent and mechanism of phase separation during the extrusion of calcium phosphate pastes," *Journal of Materials Science: Materials in Medicine*, vol. 27, no. 2, pp. 1–13, 2016.

[61] M. Habib, G. Baroud, F. Gitzhofer, and M. Bohner, "Mechanisms underlying the limited injectability of hydraulic calcium phosphate paste," *Acta Biomaterialia*, vol. 4, no. 5, pp. 1465–1471, 2008.

[62] M. Bayfield, J. A. Haggett, M. J. Williamson, D. I. Wilson, and A. Zargar, "Liquid phase migration in the extrusion of icing sugar pastes," *Food and Bioproducts Processing: Transactions of the Institution of of Chemical Engineers, Part C*, vol. 76, no. 1, pp. 39–46, 1998.

[63] J. Franco, P. Hunger, M. Launey, A. Tomsia, and E. Saiz, "Direct write assembly of calcium phosphate scaffolds using a water-based hydrogel," *Acta Biomaterialia*, vol. 6, no. 1, pp. 218–228, 2010.

[64] A. Fatimi, J. F. Tassin, J. Bosco, R. Deterre, M. A. Axelos, and P. Weiss, "Injection of calcium phosphate pastes: Prediction of injection force and comparison with experiments," *Journal of Materials Science: Materials in Medicine*, vol. 23, no. 7, pp. 1593–1603, 2012.

[65] M. Komath and H. K. Varma, "Development of a fully injectable calcium phosphate cement for orthopedic and dental applications," *Bulletin of Materials Science*, vol. 26, no. 4, pp. 415–422, 2003.

[66] I. Khairoun, F. C. Driessens, M. G. Boltong, J. A. Planell, and R. Wenz, "Addition of cohesion promoters to calcium phosphate cements," *Biomaterials*, vol. 20, no. 4, pp. 393–398, 1999.

[67] X. Wang, L. Chen, H. Xiang, and J. Ye, "Influence of anti-washout agents on the rheological properties and injectability of a calcium phosphate cement," *Journal*

of Biomedical Materials Research - Part B Applied Biomaterials, vol. 81, no. 2, pp. 410–418, 2007.

[68] N. Michida, M. Hayashi, and T. Hori, "Comparison of event related potentials with and without hypnagogic imagery," *Psychiatry and Clinical Neurosciences*, vol. 52, no. 2, pp. 145–147, 1998.

[69] L. Klouda and A. G. Mikos, "Thermoresponsive hydrogels in biomedical applications," *European Journal of Pharmaceutics and Biopharmaceutics*, vol. 68, no. 1, pp. 34–45, 2008.

[70] G. Dumortier, J. L. Grossiord, F. Agnely, and J. C. Chaumeil, "A review of poloxamer 407 pharmaceutical and pharmacological characteristics," *Pharmaceutical Research*, vol. 23, no. 12, pp. 2709–2728, 2006.

[71] B. Shriky, A. Kelly, M. Isreb, M. Babenko, N. Mahmoudi, S. Rogers, O. Shebanova, T. Snow, and T. Gough, "Pluronic F127 thermosensitive injectable smart hydrogels for controlled drug delivery system development," *Journal of Colloid and Interface Science*, vol. 565, pp. 119–130, 2020.

[72] K. Edsman, J. Carlfors, and R. Petersson, "Rheological evaluation of poloxamer as an in situ gel for ophthalmic use," *European Journal of Pharmaceutical Sciences*, vol. 6, no. 2, pp. 105–112, 1998.

[73] Y. Maazouz, E. B. Montufar, J. Malbert, M. Espanol, and M. P. Ginebra, "Self-hardening and thermoresponsive alpha tricalcium phosphate/pluronic pastes," *Acta Biomaterialia*, vol. 49, pp. 563–574, 2017.

[74] M. Bengisu, *Engineering ceramics*. Springer Science & Business Media, 2013.

[75] I. Gibson, D. W. Rosen, B. Stucker, M. Khorasani, D. Rosen, B. Stucker, and M. Khorasani, *Additive manufacturing technologies*, vol. 17. Springer, 2021.

[76] Z. Chen, Z. Li, J. Li, C. Liu, C. Lao, Y. Fu, C. Liu, Y. Li, P. Wang, and Y. He, "Journal of the European Ceramic Society 3D printing of ceramics : A review," vol. 39, no. November 2018, pp. 661–687, 2019.

[77] S. Bose, S. Vahabzadeh, and A. Bandyopadhyay, "Bone tissue engineering using 3D printing," *Materials Today*, vol. 16, no. 12, pp. 496–504, 2013.

[78] L. C. Hwa, S. Rajoo, A. M. Noor, N. Ahmad, and M. B. Uday, "Recent advances in 3D printing of porous ceramics: A review," *Current Opinion in Solid State and Materials Science*, vol. 21, no. 6, pp. 323–347, 2017.

[79] K. Tan, C. Chua, K. Leong, C. Cheah, W. Gui, W. Tan, and F. Wiria, "Selective laser sintering of biocompatible polymers for applications in tissue engineering," *Bio-medical materials and engineering*, vol. 15, no. 1-2, pp. 113–124, 2005.

[80] P. F. Jacobs, *Rapid prototyping & manufacturing: fundamentals of stereolithography*. Society of Manufacturing Engineers, 1992.

[81] M. L. Griffith and J. W. Halloran, "Freeform fabrication of ceramics via stereolithography," 1996.

[82] Z. Chen, D. Li, W. Zhou, and L. Wang, "Curing characteristics of ceramic stereolithography for an aqueous-based silica suspension," *Proceedings of the Institution of Mechanical Engineers, Part B: Journal of Engineering Manufacture*, vol. 224, no. 4, pp. 641–651, 2010.

[83] S. J. Lombardo, "Minimum time heating cycles for diffusion-controlled binder removal from ceramic green bodies," *Journal of the American Ceramic Society*, vol. 98, no. 1, pp. 57–65, 2015.

[84] X. Zhang, X. N. Jiang, and C. Sun, "Micro-stereolithography of polymeric and ceramic microstructures," *Sensors and Actuators, A: Physical*, vol. 77, no. 2, pp. 149–156, 1999.

[85] A. Withell, O. Diegel, I. Grupp, S. Reay, D. De Beer, and J. Potgieter, "Porous ceramic filters through 3D printing," *Innovative Developments in Virtual and Physical Prototyping - Proceedings of the 5th International Conference on Advanced Research and Rapid Prototyping*, pp. 313–318, 2012.

[86] G. S. Lee, J. H. Park, U. S. Shin, and H. W. Kim, "Direct deposited porous scaffolds of calcium phosphate cement with alginate for drug delivery and bone tissue engineering," *Acta Biomaterialia*, vol. 7, no. 8, pp. 3178–3186, 2011.

[87] A. Barba, Y. Maazouz, A. Diez-Escudero, K. Rappe, M. Espanol, E. B. Montufar, C. Öhman-Mägi, C. Persson, P. Fontecha, M. C. Manzanares, J. Franch, and

M. P. Ginebra, "Osteogenesis by foamed and 3D-printed nanostructured calcium phosphate scaffolds: Effect of pore architecture," *Acta Biomaterialia*, vol. 79, pp. 135–147, 2018.

[88] J. T. Huh, J. U. Lee, W. J. Kim, M. Yeo, and G. H. Kim, "Preparation and characterization of gelatin/α-TCP/SF biocomposite scaffold for bone tissue regeneration," *International Journal of Biological Macromolecules*, vol. 110, pp. 488–496, 2018.

[89] Y. Maazouz, E. B. Montufar, J. Guillem-Marti, I. Fleps, C. Öhman, C. Persson, and M. P. Ginebra, "Robocasting of biomimetic hydroxyapatite scaffolds using self-setting inks," *Journal of Materials Chemistry B*, vol. 2, no. 33, pp. 5378–5386, 2014.

[90] S. Raymond, Y. Maazouz, E. B. Montufar, R. A. Perez, B. González, J. Konka, J. Kaiser, and M. P. Ginebra, "Accelerated hardening of nanotextured 3D-plotted self-setting calcium phosphate inks," *Acta Biomaterialia*, vol. 75, pp. 451–462, 2018.

[91] B. Idowu, G. Cama, S. Deb, and L. Di Silvio, "In vitro osteoinductive potential of porous monetite for bone tissue engineering," *Journal of Tissue Engineering*, vol. 5, no. January, 2014.

[92] D. Griesiute, E. Garskaite, A. Antuzevics, V. Klimavicius, V. Balevicius, A. Zarkov, A. Katelnikovas, and D. Sandberg, "Synthesis , structural and luminescent properties of Mn - doped calcium pyrophosphate (polymorphs," *Scientific Reports*, pp. 1–10, 2022.

[93] M. Nilsson, E. Fernández, S. Sarda, L. Lidgren, and J. A. Planell, "Characterization of a novel calcium phosphate/sulphate bone cement," *Journal of Biomedical Materials Research*, vol. 61, no. 4, pp. 600–607, 2002.

[94] M. Bohner, "New hydraulic cements based on α-tricalcium phosphate-calcium sulfate dihydrate mixtures," *Biomaterials*, vol. 25, no. 4, pp. 741–749, 2004.

[95] W. L. Chen, C. K. Chen, J. W. Lee, Y. L. Lee, C. P. Ju, and J. H. C. Lin, "Structure, properties and animal study of a calcium phosphate/calcium sulfate com-

posite cement," *Materials Science and Engineering C*, vol. 37, no. 1, pp. 60–67, 2014.

[96] D. Freyer and W. Voigt, "Crystallization and Phase Stability of CaSO4 and CaSO 4 - Based Salts," *Monatshefte fur Chemie*, vol. 134, no. 5, pp. 693–719, 2003.

[97] L. Berzina-Cimdina and N. Borodajenko, "Research of Calcium Phosphates Using Fourier Transform Infrared Spectroscopy," *Infrared Spectroscopy - Materials Science, Engineering and Technology*, 2012.

[98] Y. Liu, A. Wang, and J. Freemen, "Raman, mir, and nir spectroscopic study of calcium sulfates: gypsum, bassanite, and anhydrite," in *40th Annual Lunar and Planetary Science Conference*, p. 2128, 2009.